Electromagnetic Inversion Strategies for Antenna Design and Characterization

by

Chaitanya Narendra

A Thesis submitted to the Faculty of Graduate Studies of
The University of Manitoba
in partial fulfilment of the requirements of the degree of

Doctor of Philosophy

Department of Electrical and Computer Engineering
University of Manitoba
Winnipeg, Manitoba, Canada

Abstract

In this work, we use the electromagnetic inversion (EI) framework to develop/improve algorithms for the purpose of antenna design and characterization. Broadly speaking, antennas are any device, object, or system that can transform energy in the form of guided waves to energy in the form of radiated waves in space. In our increasingly wireless technology landscape, many different types of antennas are being analyzed and developed for a variety of applications. Therefore a flexible design/characterization methodology is required to support our future wireless engineering needs.

To this end, we employ an EI methodology that allows the flexibility to develop novel antenna characterization and design algorithms in a variety of applications. In general, electromagnetic inversion enables the determination of an electromagnetic property of interest (e.g., relative permittivity or equivalent current distribution) in an investigation domain by processing some type of electromagnetic data (e.g., complex electric field, phaseless data, or far-field performance criteria) on a separate measurement/desired data domain wherein the investigation and data domains can be arbitrarily shaped; our methodology allows for this flexibility to be utilized. Through the use of this methodology and the electromagnetic surface and volume equivalence principles we develop EI algorithms to contribute to the areas of metasurface design, microwave imaging, and dielectric lens/antenna design.

Specifically, (i) we develop and demonstrate a gradient-based EI algorithm that can directly design the circuit admittance profiles of metasurfaces from desired complex or phaseless (magnitude-only) magnetic field data on an external data domain, (ii) we develop and verify inverse scattering algorithms to reconstruct dielectric profiles from phaseless synthetic and experimentally measured data, and finally (iii) we introduce a combined inverse source and scattering technique to tailor electromagnetic fields by designing passive, lossless, and reflectionless dielectric profiles to transform an existing electromagnetic field distribution from a known feed to one that satisfies desired far-field performance criteria such as main beam directions, null locations, and half-power beamwidth.

Acknowledgements

First, I would like thank my advisor and friend Dr. Puyan Mojabi for his guidance throughout my academic journey and for inspiring me to begin the journey in the first place all those years ago in his antennas course at the end of my B.Sc. Thanks also to my friends and colleagues Dr. Trevor Brown, Chen Niu, and Dr. Nozhan Bayat for making my time at the University of Manitoba an absolute joy.

I would like to express my gratitude to my Ph.D. internal committee members Dr. Ian Jeffrey, Dr. Jason Fiege, and my external committee member Dr. Andrea Massa for taking the time to help me improve my thesis.

Lastly, I'd like to thank the University of Manitoba Electromagnetic Imaging Laboratory and Dr. Joe LoVetri for providing experimental data for this work, the University of Manitoba Graduate Fellowship, the University of Manitoba GETS program, Natural Sciences and Engineering Research Council of Canada, and the Canada Research Chair program for financially supporting this work, and finally the Canadian Microelectronics Corporation (CMC) for providing the use of ANSYS Electronics Desktop.

Contents

List of Tables

List of Figures

Important Abbreviations

2D	**2 D**imensional
3D	**3 D**imensional
AUT	**A**ntenna **U**nder **T**est
CSI	**C**ontrast **S**ource **I**nversion
EI	**E**lectromagnetic **I**nversion/ **I**nverse
GSTC	**G**eneralized **S**heet **T**ransition **C**onditions
HPBW	**H**alf-**P**ower **B**eam**w**idth
LPC	**L**ocal **P**ower **C**onservation
MoM	**M**ethod **o**f **M**oments
MWI	**M**icro**w**ave **I**maging
PGNI	**P**haseless **G**auss-**N**ewton **I**nversion
ROI	**R**egion **o**f **I**nterest
SL-PGNI	**S**hape and **L**ocation **PGNI**
SRM	**S**ource **R**econstruction **M**ethod
SP-PGNI	**S**patial **P**riors **PGNI**
TE$_z$	**T**ransverse **E**lectric to the $\hat{z}$ direction
TM$_z$	**T**ransverse **M**agnetic to the $\hat{z}$ direction
TV	**T**otal **V**ariation

Important Symbols

λ	Wavelength
$\vec{\mathscr{E}}$	Electric field intensity in the time domain
$\vec{\mathscr{H}}$	Magnetic field intensity in the time domain
ϵ	Permittivity
μ	Permeability
$\vec{\mathscr{J}}$	Electric current density in the time domain
$\mathscr{Q}_v$	Volumetric charge density
$\vec{E}$	Electric field intensity phasor
$\vec{H}$	Magnetic field intensity phasor
$\vec{J}$	Electric current density phasor
$\vec{M}$	Magnetic current density phasor
f	frequency
ω	angular frequency
t	time
j	$\sqrt{-1}$
$\mathcal{S}$	Measurement/Data Domain
$\mathcal{D}$	Imaging domain for microwave imaging
χ	Contrast from microwave imaging
L_2	The Euclidean norm

To my parents, my sister, and Keeley...

Chapter 1

Introduction

This thesis uses the electromagnetic inversion (EI) framework for antenna design and characterization. In this chapter we present an overview of the common methodology we use to solve a diverse set of problems. We begin by briefly reviewing antennas and what it means to characterize or design them. Next, we present the basic concept and subcategories of EI and a summary of the framework's challenges. Finally, the benefits of the EI framework and general methodology we adopted to solve EI problems are discussed.

1.1 Antennas

In this work, we focus on the problem of characterizing and designing antennas. Antennas are essential to much of today's modern technology, and with the current trend toward a more wireless world, their use is only increasing. Broadly speaking, antennas can be defined as transitional devices that serve as a bridge between energy in the form of *guided* electromagnetic waves (e.g., in a two-wire transmission line) to energy in the form of electromagnetic *radiation* in space [5]. Consequently, antennas can be characterized by circuit *and* spatial properties. The circuit properties of an antenna relate to its overall

energy use and storage, which is useful for cases where the antenna needs to be seen as a lumped element in a larger circuit/network.[1] However, in this work we are interested in characterizing and designing radiators with respect to their spatial properties.

The spatial properties of an antenna are those describing how it distributes electromagnetic radiation in space (e.g., far-field radiation pattern, near-field distribution, main-beam direction, etc.) [5]. Depending on the design, antennas send and receive electromagnetic radiation in certain directions more than others. Consequently, different antennas are designed and used for wireless applications based on the required spatial properties. For example, cellular base station antennas often require the reception of signals from all directions equally to ensure reliable communication within a certain radius, while reflector antennas that are used for space communication applications need to accentuate signals in a specific direction. In this work, we implement the EI framework through a methodology that can facilitate the design or analysis of different antennas and their spatial properties.

According to the definition of an antenna presented above, they can take many forms. Common antenna types for example include dipole antennas, patch antennas and horn antennas [5]. These antennas are composed of a single radiating element, however, antennas can also be composed of feed elements and a *field modifier* such as a reflector, metasurface [6–8], or dielectric material [9, 10] that works in conjunction with the feed to produce the intended spatial properties. The human body can also be thought of as part of an antenna as it will affect the original incident field distribution of a source (e.g., the electromagnetic field distribution of a cell-phone is different if it is in the presence of a human compared to when it is radiating in free-space).[2] Next, let us explore how we can characterize the spatial properties of these different types of antennas.

[1] For example, like other lumped elements, an antenna can be characterized by its input impedance.

[2] The incident field of a source is its electromagnetic field distribution in isolation, i.e., when there are no other sources or material in its presence. In the context of microwave imaging the incident fields are the fields of the source in the absence of the object of interest.

1.2 Antennas and Radiation

The spatial properties of an antenna are related to the electromagnetic field distribution it generates. Therefore, let us consider how an antenna produces an electromagnetic field. The following are Maxwell's equations in the time domain combined with the constitutive relationships in a linear and isotropic medium [11]

$$\begin{aligned} \nabla \times \vec{\mathscr{E}}(\vec{r},t) &= -\frac{\partial \mu(\vec{r})\vec{\mathscr{H}}(\vec{r},t)}{\partial t}, & \nabla \cdot \mu(\vec{r})\vec{\mathscr{H}}(\vec{r},t) &= 0, \\ \nabla \times \vec{\mathscr{H}}(\vec{r},t) &= \frac{\partial \epsilon(\vec{r})\vec{\mathscr{E}}(\vec{r},t)}{\partial t} + \vec{\mathscr{J}}(\vec{r},t), & \nabla \cdot \epsilon(\vec{r})\vec{\mathscr{E}}(\vec{r},t) &= \mathscr{Q}_v(\vec{r},t). \end{aligned} \tag{1.1}$$

In (1.1), $\vec{\mathscr{E}}(\vec{r},t)$ is the electric field intensity and can vary as a function of position $\vec{r}$ and time t (henceforth, we suppress the explicit reference to the arguments $\vec{r}$ and t for brevity), ϵ is the permittivity, $\vec{\mathscr{H}}$ is the magnetic field intensity, μ is the permeability, $\vec{\mathscr{J}}$ is the electric current density, and $\mathscr{Q}_v$ is the volumetric charge density. The two equations on the left (Faraday's law and Ampère-Maxwell's law) are coupled, and describe how electromagnetic waves propagate. However, a source is needed to start the propagation process, i.e., we need to generate $\vec{\mathscr{J}}$.[3]

With some manipulation of Ampère-Maxwell's law and Gauss' Law, it can be shown that

$$\nabla \cdot \vec{\mathscr{J}} = -\frac{\partial \mathscr{Q}_v}{\partial t}, \tag{1.2}$$

which is referred to as the equation of continuity. In this form, it shows that there must be movement of charge ($-\frac{\partial \mathscr{Q}_v}{\partial t}$), to create $\vec{\mathscr{J}}$ (i.e., $-\frac{\partial \mathscr{Q}_v}{\partial t}$ is the source of $\vec{\mathscr{J}}$). A steady current (i.e. $\mathscr{Q}_v$ is moving with a constant velocity) can generate a static magnetic or electromagnetic radiation in special cases.[4] However, it can be shown that to generate electromagnetic radiation in general, there must be a time-varying current, or acceleration of charge [5]. This is the purpose of antennas: they generate electromagnetic radiation

[3]Note that for simplicity we have assumed zero conductivity for the medium in (1.1). When the conductivity σ is present, $\vec{\mathscr{J}}$ consists of two components including the impressed current and $\sigma\vec{\mathscr{E}}$.

[4]If there is a steady current but the conducting path is bent, there can be radiation [5].

by supporting the needed time-varying current distributions. Therefore, if we are able to represent an antenna by the appropriate current distribution, we can characterize any of its spatial properties. This is why the current distribution of a radiator is often referred to as its fundamental spatial property.

Antennas often support time-harmonic current as a means to create electromagnetic radiation. Consequently, the electromagnetic responses of the antennas are often studied in the frequency domain wherein we can substitute the instantaneous quantities in Maxwell's equations with their phasor counterparts. For example, the equation $\vec{\mathscr{E}}(\vec{r},t) = \mathrm{Re}\left(\vec{E}(\vec{r})e^{j\omega t}\right)$ describes how the instantaneous ($\vec{\mathscr{E}}(\vec{r},t)$) and phasor representation of the electric field ($\vec{E}(\vec{r})$) are related, where Re(.) is an operator extracting the real part of a complex quantity, $j = \sqrt{-1}$, and $\omega = 2\pi f$ is the angular frequency of operation. Note that throughout this work we assume $e^{j\omega t}$ time dependency. Now we can write Maxwell's equations in the frequency domain combined with the constitutive relationships in a linear and isotropic medium as

$$\begin{aligned} \nabla \times \vec{E}(\vec{r}) &= -j\omega\mu(\vec{r})\vec{H}(\vec{r}), \qquad \nabla \cdot \mu(\vec{r})\vec{H}(\vec{r}) = 0, \\ \nabla \times \vec{H}(\vec{r}) &= j\omega\epsilon(\vec{r})\vec{E}(\vec{r}) + \vec{J}(\vec{r}), \qquad \nabla \cdot \epsilon(\vec{r})\vec{E}(\vec{r}) = \rho_v(\vec{r}), \end{aligned} \tag{1.3}$$

where all the instantaneous quantities save been replaced with their phasor counterparts and we have explicitly written that these quantities are a function of position for clarity. (As previously stated we continue to suppress the explicit reference to $\vec{r}$ except when required for clarity.) For the sake of analysis, Faraday's law is often written as

$$\nabla \times \vec{E} = -j\omega\mu\vec{H} - \vec{M}, \tag{1.4}$$

where $\vec{M}$ denotes the magnetic current density. Although natural magnetic sources have not been documented, they are often used to simplify analysis.[5] Throughout the course of this thesis, we will assume that we are in the frequency domain.[6]

[5]Infinitesimal loops of electric current may be represented by magnetic currents.

[6]In the above, we have written the electric flux density $\vec{D}$ as $\epsilon\vec{E}$. For bi-isotropic material, this can be extended to $\vec{D} = \epsilon\vec{E} + \xi\vec{H}$. We will then have a similar relation for the magnetic flux density $\vec{B}$ based

1.3 Electromagnetic Equivalence Principles

In the previous section, it was explained why the current distribution of an antenna is so important to antenna design and characterization. In many cases, it may be unnecessary to find the exact current distribution flowing through the antenna in order to characterize the necessary spatial properties. Instead, we may use the concept of equivalent currents as defined by the electromagnetic surface and volume equivalence principles.

1.3.1 Surface Equivalence Principle

It is possible to leverage the surface electromagnetic equivalence principle [11], which allows for the replacement of the original problem wherein the true source or sources in a region bounded by a surface $\mathcal{S}'$ is/are radiating the true electromagnetic field ($\vec{E}_0$ and $\vec{H}_0$) with an equivalent problem wherein the same true electromagnetic fields are radiated *outside* $\mathcal{S}'$, but the field inside $\mathcal{S}'$ can be arbitrary; the discontinuity in fields is supported by electric and magnetic surface current densities ($\vec{J}$ and $\vec{M}$) on the region's boundaries. This is summarized in Figure 1.1.

Because $\vec{J}$ and $\vec{M}$ generate the same electromagnetic fields as the true source outside of $\mathcal{S}'$, they are often referred to as *equivalent* currents. Furthermore, since we can remove the original sources, the equivalent currents radiate in a homogeneous background medium (such as free space), making it easy to find the Green's function.[7] Therefore the surface equivalence principle enables the characterization of spatial properties with equivalent currents, and it is not always necessary to find the true currents of the antenna.

It is often desirable to utilize a special case of the surface equivalence principle, namely, Love's equivalence principle. In this special case, the fields $\vec{E}_1$ and $\vec{H}_1$ in the equivalent

on $\vec{E}$ and $\vec{H}$ [12]. As will be seen later, this magneto-electric coupling is typically used in the design of metasurfaces. Finally, for the anisotropic (or bi-anisotropic) medium, the material properties such as the permittivity ϵ needs to be written in the form of a tensor $\bar{\bar{\epsilon}}$.

[7] The Green's function maps a point source in a medium to the electromagnetic field created by that source [11].

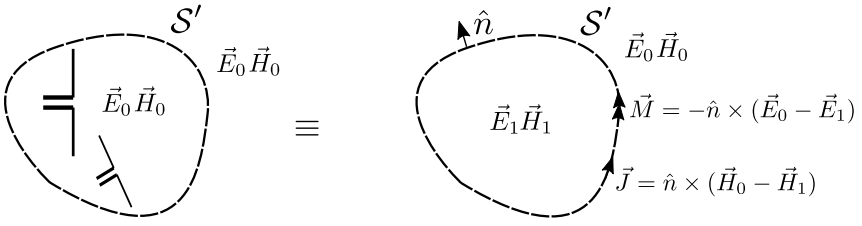

Figure 1.1: The surface electromagnetic equivalence principle. The original problem (left) where a true source (can include more than one radiator) is bounded by an arbitrary surface $\mathcal{S}'$ and is radiating the true electromagnetic field ($\vec{E}_0$ and $\vec{H}_0$) can be replaced with an equivalent problem (right) where the same field ($\vec{E}_0$ and $\vec{H}_0$) is being radiated *outside* $\mathcal{S}'$ but the field inside $\mathcal{S}'$ ($\vec{E}_1$ and $\vec{H}_1$) can be arbitrary. The discontinuity in the fields is supported by a set of electric and magnetic current densities ($\vec{J}$ and $\vec{M}$) on $\mathcal{S}'$. Note that in the boundary condition equations, $\hat{n}$ is the outward facing normal unit vector to $\mathcal{S}'$.

problem are enforced to be zero. Doing so presents certain advantages. For example, if Love's condition is enforced, we can directly relate the electric and magnetic current densities $\vec{J}$ and $\vec{M}$ to the field outside $\mathcal{S}'$ using a simplified version of the boundary condition equations

$$\begin{aligned} \vec{J} &= \hat{n} \times \vec{H}_0, \\ \vec{M} &= -\hat{n} \times \vec{E}_0. \end{aligned} \tag{1.5}$$

Consequently, this form of the equivalence principle allows for the determination of an outward propagating (dependent on time convention) electromagnetic aperture field on $\mathcal{S}'$, in contrast to finding a set of current densities $\vec{J}$ and $\vec{M}$ that may affect the region inside $\mathcal{S}'$. This is advantageous for design applications where a desired transmitted field (and not currents) are required on the output side of the device being created as will be seen in Chapter 3 and 5.

1.3.2 Volume Equivalence Principle

Another type of equivalence principle is the volume equivalence principle for penetrable scatterers [13]. This principle is used in the design of dielectric lenses and microwave imaging, and replaces an inhomogeneous permittivity (and/or permeability) profile of a scatterer with equivalent induced polarization currents. To see how this is possible, consider Maxwell's equations with no impressed sources as shown below

$$\begin{aligned} \nabla \times \vec{E} &= -j\omega\mu\vec{H}, \\ \nabla \times \vec{H} &= j\omega\epsilon\vec{E}, \end{aligned} \tag{1.6}$$

where $\mu = \mu_0\mu_r$ and $\epsilon = \epsilon_0\epsilon_r$. Therefore the permittivity and permeability can be decomposed into the permittivity and permeability of free space (ϵ_0, μ_0) and the relative permittivity and permeability (ϵ_r, μ_r). Recall that ϵ_r and μ_r can be a function of space. For example, within a penetrable scatterer (such as a human body or a dielectric lens) $\epsilon_r \neq 1$ whereas in free space $\epsilon_r = 1$. However, we can re-write Maxwell's equations to include the effect of the scatterer in a set of equivalent currents

$$\begin{aligned} \nabla \times \vec{E} &= -j\omega\mu_0\vec{H} - \underbrace{j\omega\mu_0(\mu_r - 1)\vec{H}}_{\vec{M}_{\text{eq}}}, \\ \nabla \times \vec{H} &= j\omega\epsilon_0\vec{E} + \underbrace{j\omega\epsilon_0(\epsilon_r - 1)\vec{E}}_{\vec{J}_{\text{eq}}}, \end{aligned} \tag{1.7}$$

where $\vec{M}_{\text{eq}}$ and $\vec{J}_{\text{eq}}$ are the equivalent currents that are a function of the scatterers internal electromagnetic properties. It is also instructive to note that both the right hand side terms can be thought of as contributing to the total field on the left hand side. Therefore, the total field is composed of the incident field (field that would be present if there were no scatterer, i.e., $\epsilon_r = 1$ and $\mu_r = 1$) and scattered field (field generated by $\vec{M}_{\text{eq}}$ and $\vec{J}_{\text{eq}}$). Finally, we note that the other advantage of making use of $\vec{M}_{\text{eq}}$ and $\vec{J}_{\text{eq}}$ is that they radiate in free-space, once again simplifying the process of obtaining a Green's function.

In summary, the surface and volume equivalence principle are useful in characterizing and designing the spatial properties of antennas as they can represent the true source/scatterer with an equivalent problem. In order to use these equivalence principles to solve practical problems, we apply them through an electromagnetic inversion framework.

1.4 Electromagnetic Inversion

Electromagnetic inversion is the process by which specific *properties* of an *investigation domain* are calculated from *electromagnetic data* obtained outside that investigation domain; the properties of interest are also a *cause* (or part of the cause) for the measured electromagnetic data (the *effect*) [2, 14].[8] The properties of interest, investigation domain, and type of electromagnetic data can vary depending on the application. This is summarized in Figure 1.2.

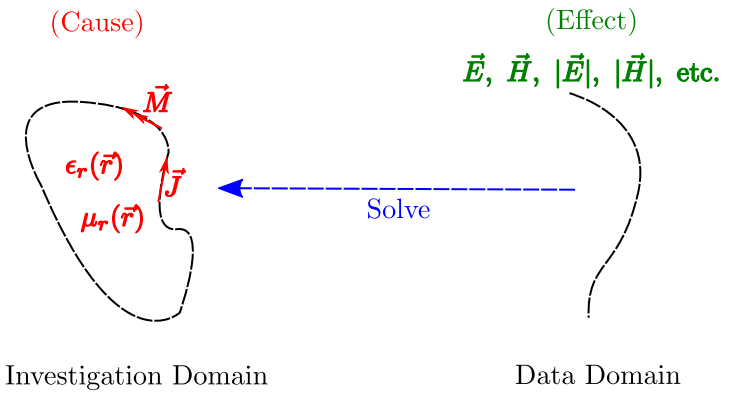

Figure 1.2: An overview of electromagnetic inversion wherein certain properties in an investigation domain are calculated from known electromagnetic data on an external data domain. The properties in the investigation domain are a cause (or part of the cause) for the electromagnetic data on the data domain. Examples of the properties of interest could be the electric or magnetic current densities on the investigation domain, while the electromagnetic data could be the complex electric field distribution or magnetic field distribution.

[8]The flow of information is important when defining an inverse problem. In such problems, we are trying to find the cause from some effect. If instead, we are trying to calculate the effect (e.g., the far-field pattern of a source) from the cause (e.g., the true antenna), then this is referred to as a forward problem.

For a specific example, consider the application of near-field antenna measurements, wherein the spatial properties (e.g. far-field pattern or directivity) of an antenna under test (AUT) are to be inferred from near-field measurements [15, 16]. One way we can solve this problem is to solve an electromagnetic inverse problem to reconstruct the equivalent (surface) current distribution of the AUT. Once we have inferred the equivalent current distribution, we can calculate the AUT's electromagnetic field distribution, and therefore, its spatial properties.[9] The property of interest in this application is the equivalent current distribution of the AUT, the investigation domain is often a reconstruction surface enclosing the AUT, and the electromagnetic data are tangential electric and/or magnetic field measurements on some domain outside that reconstruction surface [17, 18].[10] It should also be clear that the surface equivalence principle is being used in this application.

In general, electromagnetic inverse problems can be categorized depending on their property of interest. This is explained in the following sections.

1.4.1 Types of Electromagnetic Inverse Problems

Electromagnetic inverse problems can be separated into two different types based on the property of interest: (I) inverse source problems, and (II) inverse scattering problems. In (I) *sources* that generate specific electromagnetic data are the property of interest (e.g., seeking an equivalent current distribution in antenna diagnostics or contrast sources in microwave imaging [14, 19]). Therefore, inverse source problems are formulated as

$$f_{\text{data}} = \mathcal{L}\left(U_{\text{sources}}\right), \tag{1.8}$$

[9] If the AUT's equivalent current distribution is known, we can calculate the associated electromagnetic fields using the Green's function of free space and the electric/magnetic field integral equations. This will be described in detail in later chapters.

[10] It is clear in this case that the equivalent current distribution, which can replace the true source, is the cause of the electromagnetic field comprises the measured data.

where f_{data} is a known function describing the electromagnetic data, U_{sources} is the unknown function representing the sources (e.g., this could be the equivalent current distribution on the antenna), and $\mathcal{L}$ is the operator that maps the sources to the data. In contrast, (II) tries to recover material properties of scatterers that produce a specific electromagnetic field when in the presence of known sources (e.g., reconstructing the dielectric profile in microwave imaging [19, 20]).[11] In inverse scattering applications, in addition to a formulation mapping some type of sources to the electromagnetic data as in (1.8), there is a relation

$$U_{\text{sources}} = \mathcal{K}\left(X_{\text{material}}\right), \tag{1.9}$$

where X_{material} is the unknown function representing the sought after material parameters (e.g., this could be the relative permittivity distribution), and $\mathcal{K}$ is an operator mapping X_{material} to sources that radiate.

All applications that make use of electromagnetic inversion can be characterized into one of these two types of problems. Figure 1.3 summarizes the above discussion and also lists some applications that use electromagnetic inversion.[12] It is important to note that the applications in Figure 1.3 can be divided into characterization and design applications. Characterization problems involve the analysis of an existing antenna, while design involves the synthesis of an antenna. Consequently, in EI characterization applications, the electromagnetic data is some form of measured data, while in EI design applications, desired electromagnetic data is used.

As can be seen from Figure 1.3, electromagnetic inverse source and scattering problems have been used in many applications, however, there are difficulties that must be overcome when solving these types of problems.

[11] One way to distinguish between inverse source and scattering problems is to consider whether more information can be gathered about the property of interest by further experimentation. In inverse scattering problems, one can obtain more information about the physical scatterers in the ROI by changing the known sources, changing the position of the known sources, and changing the frequency of operation. However, in inverse source problems, one can only gain extra information by thorough and accurate sampling of the associated electromagnetic field [19].

[12] For a discussion on the advantages of the electromagnetic inversion framework for antenna pattern synthesis, see [21].

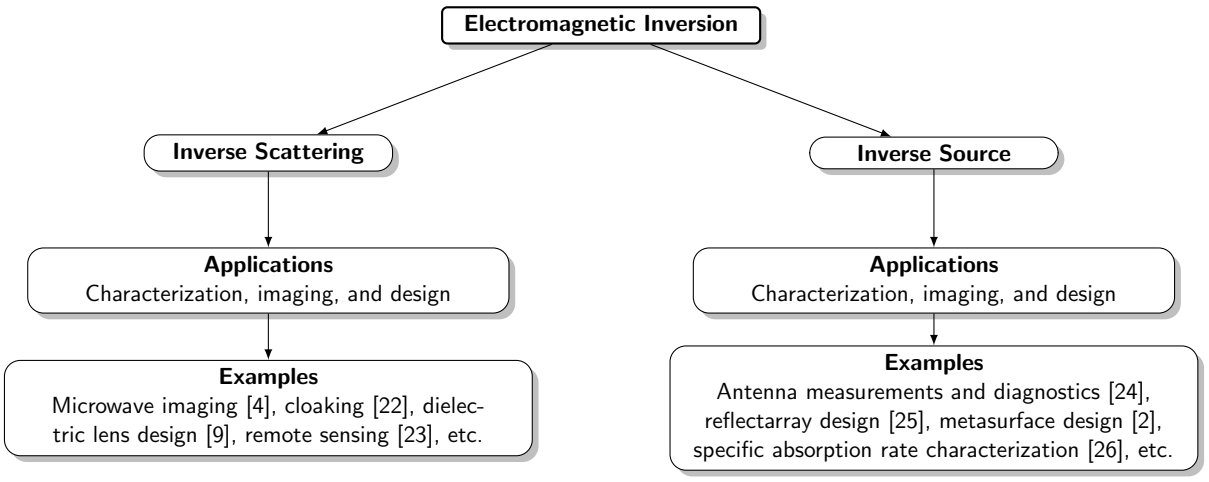

Figure 1.3: Electromagnetic inversion and applications. This figure is slightly modified from the one that appears in [1].© 2020 IEEE.

1.4.2 Difficulties

All electromagnetic inverse problems are ill-posed [19, 27]. Consequently, these problems deal with the issues of uniqueness, existence, and instability. Furthermore, the issue of uniqueness or existence may become more prominent based on whether we apply the electromagnetic inversion framework to characterization or design applications.[13] Consider, for example, an inverse source problem where one is trying to solve for a set of currents for an antenna diagnostics problem from measured electric field data; due to the non-uniqueness of the problem [28], there would be many such current distributions (e.g., a small dipole antenna with a *uniform* current distribution will produce an electromagnetic field indistinguishable from a small dipole with twice the length of the previous one, with a *triangular* current distribution after some distance [5]). This is clearly problematic for this application because the *true* solution is one among many possible solutions. Note that since this is a characterization problem, there is a true source and thus existence is not an issue. However, consider a scenario where a dielectric lens is being designed to scatter a given electromagnetic field to form a desired far-field pattern. There can be many dielectric profiles that can be used to generate the desired field for a given

[13]We remind the reader that characterization problems involves analysis while design involves synthesis. In EI characterization applications, the electromagnetic data is some form of measured data, while in EI design applications, desired electromagnetic data used.

source. However, in this design application, certain solutions can help facilitate the lens fabrication process more than others. For example, a dielectric profile wherein only two permittivity values are used may be easier to fabricate than one where many different values are needed. In this problem, existence is an issue: it may not be possible for a dielectric profile of a specific size to meet the user's desired field specifications. Additionally, electromagnetic inverse problems also suffer from instability [19]. This means that a small change in the measured electromagnetic data, can result in a large change in the solution of the property of interest. This can cause problems numerically when solving the inverse problem and lead to erroneous solutions.

Regularization methods enable a way to alleviate these issues.[14] These methods facilitate the choice of an appropriate solution to the inverse problem by incorporating information into the solution of electromagnetic inverse problems [29]. This information can either be about the desired behaviour in the solution (e.g., standard weighted L_2 norm total variation multiplicative regularization is used in microwave imaging and near-field antenna measurements for its smoothing and edge preserving properties [24, 30, 31]) or to incorporate *prior* information about the problem (e.g., a multiplicative regularization scheme has been used in microwave imaging to incorporate information about the expected relative permittivity values of objects being imaged [32]). The implementation of regularization methods often involves the use of regularization parameter weights to define the amount of emphasis given to a particular regularization method during the inversion process, e.g., if a higher weight is used with an additive L_2 norm total variation regularizer, there will be more emphasis on finding a solution that is smooth as compared to the case where a lower weight is used. The process of choosing the appropriate regularization weights poses another challenge in the inversion process.[15]

[14] They, for example, achieve this by filtering out smaller singular values of the associated (linearized) ill-posed operator via augmenting the main data-misfit cost functional with a penalty term.

[15] The methods used to choose the appropriate weights are often referred to as regularization parameter choice methods [33].

1.4.3 Benefits and Motivation

Despite the general difficulties outlined in the previous section, EI-based algorithms are widely used due to their many advantages. The specific advantages that can be gained by the EI framework depend on the methodology that is taken to implement algorithms within this framework. For example, machine learning approaches to solving EI problems will have different benefits (and disadvantages) than physics based approaches. In this section we will outline the main common benefits.

Firstly, EI-based algorithms can be formulated to use many different forms of electromagnetic data to solve for the same property of interest. This is often beneficial because one type of data may be more useful in certain situations. For example, consider the case of using inverse source algorithms for near-field antenna measurements. Many of these algorithms have been developed that make use of complex electromagnetic field data [15, 34–36], but algorithms that make use of phaseless (magnitude only) electromagnetic data have also been developed and demonstrated for the same purpose [24, 37] where the lower cost of measuring magnitude-only electromagnetic data motivated the research. Similarly, we developed an EI-based methodology for metasurface design that can make use of desired complex, phaseless, and far-field criteria [2]. This helps facilitate the metasurface design process as designers are sometimes only interested in tailoring a specific power pattern or meeting specifications like main beam direction or null location.

EI-based algorithms can also be formulated to solve for different properties of interest for the same application. Consider the application of metasurface design wherein these devices can be represented by (but not limited to) a surface susceptibility profile or a circuit admittance profile (see Chapter 2 and Chapter 3) if a specific type of model is assumed. Each representation method for the metasurface has different benefits, and EI algorithms have been developed to solve for both properties of interest [2, 38, 39]

The electromagnetic data is often specified on a measurement/desired data domain and the property of interest is often solved for on an investigation domain. Another benefit

of EI-based algorithms is that these domains can be arbitrary in shape.[16] For example, consider the case of near-field antenna measurements where modal expansion algorithms are traditionally used for near-field to far-field transformations. These modal expansion algorithms traditionally require canonical measurement domain shapes, whereas, there are applications where more irregularly shaped measurement domains may be required. Inverse source antenna measurement algorithms in the literature have been shown to be capable of using arbitrarily shaped measurement domains [35]. To this end, in [15], we developed a near-field antenna measurement inverse source algorithm that makes use of multiple planes of magnetic field measurements to potentially increase the accuracy of an existing planar, bench top antenna measurement system (see Appendix C).

In summary, the EI framework enables extraordinary flexibility that can be used to benefit many applications. With rapidly changing needs of wireless technology, this framework is well suited to keep pace and provide utility to the engineers working in this area. Next, we provide the methodology we use throughout this work to implement the advantages above to various applications.

1.4.4 Solution Methodology Overview

We employ a common framework to characterize and design sources and scatterers in different applications. Throughout this thesis, we contribute to the literature by adding novel aspects to this general framework, or applying it in a novel manner to solve a problem. These contributions will be made clear in the chapter introductions before we present the main body of the chapter. The steps we take in our approach are shown below.

1. **Determine the type of the measured/desired electromagnetic data**

[16] These domains can be arbitrarily shaped and the inversion algorithm can still calculate a solution, but certain domain geometries may lead to better results. For example, in antenna measurements it is beneficial to have tangential electromagnetic data on a measurement domain completely enclosing the true source.

This step requires the choice of electromagnetic data that will be used in the inversion process. For example, the data could be complex electric field data, phaseless electric field data, complex magnetic field data, or performance criteria (such as main beam direction, null locations etc.) Note that for design problems this is *desired* data, while for characterization, this is *measured* data.

2. **Determine the form of the property of interest**

   We must decide what we are solving for using the known electromagnetic data. For example, in inverse source problems we are solving for the equivalent electric and magnetic current densities and for inverse scattering problems we could be interested in reconstructing the permittivity distribution in an investigation domain [31, 40, 41], circuit admittance profile of a metasurface [38, 42, 43], or surface susceptibilities [2, 6] of a metasurface (these applications are discussed in further detail in the next chapter).

3. **Determine a physical model to relate the property of interest to the electromagnetic data**

   The first two steps that were presented are necessary for solving any inverse problem; this is the first step where we choose specific methods. Throughout the work we relate the properties of interest to the electromagnetic data through a physical model. In order to model the behaviour of electromagnetic fields we use Maxwell's equations in the integral form and utilize the method of moments (MoM) to develop discrete operators that transform sources to fields. This process is explained in more detail throughout the remainder of the thesis.

   Note that there are other methods to relate the knowns to unknowns when solving inverse problems including data driven/machine learning methods and physical solutions using differential equations. However, in the electromagnetic characterization and design applications we contributed to in this work, it is often difficult to obtain the large amounts of data needed for a data driven solution. For example, if the application is near-field antenna measurements, obtaining many different

types of antennas and measuring their electromagnetic near and far-fields would be a time consuming, expensive endeavour. Additionally, more general solutions often require more data. For these reasons, we chose to use physical models in this work, however, many machine learning solutions to electromagnetic inverse problems have been reported in the literature [44–46]. We use MoM solvers because in both characterization and design problems, the electromagnetic data is usually defined on a surface domain. Therefore, we often require field operators to map sources to electromagnetic data on an external surface. Because we do not need to know the field between the sources and measured/desired surface domain, we have not made use of differential equation based operators.

4. **Construct an appropriate data-misfit cost functional and minimize using gradient-based optimization**

   In order to solve for the property of interest using the physical model developed in the previous step, we formulate an appropriate data-misfit cost functional and minimize the functional with respect to the property of interest. We may utilize additive, multiplicative and Krylov subspace regularization in conjunction with the data-misfit part of the cost functional. Finally, to minimize the cost-functional we use iterative gradient-based methods.

This methodology has successfully been used to solve many different types of EI problems in the literature. In this thesis, we apply these techniques in unique ways and add to this framework so that we can characterize and design antennas. Specifically, we contribute to the areas of microwave imaging, metasurface design, and dielectric antenna design. In the next chapter, the reasoning behind choosing these applications is explained and a brief introduction on each of the topics is presented to ready the reader for more detailed explanations of the contributions in each area in the subsequent chapters.

1.5 Thesis Outline

This thesis is a grouped manuscript or sandwich-style thesis defined by the University of Manitoba. Consequently, chapters 3 to 5 are the author's published or submitted peer-reviewed journal papers; a complete list of the author's published and submitted papers and contributions thereof can be found in Appendix D. Due to the use of the grouped manuscript style, some general information and concepts as well as theory/background may be repeated throughout this thesis.

This chapter presented the main purpose of this thesis: to develop new and improve existing electromagnetic inversion based methods to characterize and design antennas. In Chapter 2, a brief introduction of the three different application areas that are contributed to by this work are presented to prepare the reader for a more detailed explanations of the contributions in subsequent chapters. Next, in Chapter 3, we present a gradient-based EI algorithm to design metasurfaces utilizing a three-layer impedance/admittance model. This algorithm enables the calculation of circuit admittances directly, a property of interest that can be more useful when designing metasurfaces than the existing inversion algorithms for metasurface design that we presented previously that reconstruct the necessary transmitted field on the output boundary on the metasurface. Following this, in Chapter 4 we present a novel phaseless Gauss-Newton Inversion inverse scattering algorithm for microwave imaging. The purpose of this work was to leverage the EI framework to be able to reconstruct the complex permittivity in a region from phaseless/magnitude-only measured data; this can result in more cost effective imaging systems. Next we move to dielectric lens/antenna design applications. In Chapter 5, we present a combined inverse source and scattering technique for dielectric profile design to tailor electromagnetic fields. In this work we clearly show the advantages of and a way to combine inverse source and scattering techniques to design dielectric profiles (i.e. lens antennas). Finally, in Chapter 6, the work in the thesis is summarized, the contributions are clearly presented, and future work is suggested.

Chapter 2

Background and Application Areas

In this work, we contribute to the areas of metasurface design, microwave imaging, and dielectric antenna/lens design by applying the electromagnetic inversion framework methodology described in the previous chapter. Herein, we explain the reasoning behind the choice of contributing to these specific applications while briefly introducing them to prepare the reader for the latter chapters that describe our contributions to each area in detail.

2.1 Antenna Design and Characterization Philosophy

As was explained in Section 1.2, an antenna's current distribution can be thought of as its fundamental spatial property as it determines the way the antenna radiates in space. According to the surface equivalence theorem (summarized in Section 1.3.1), a true source can be replaced with a set of equivalent currents that are still capable of producing the same spatial properties as the true source. Additionally, according to the volume equivalence principle (summarized in Section 1.3.2), penetrable scatterers can

be characterized by a set of volumetric currents (i.e., the currents that are internal to the volume of the scatterer) that are related to the material properties of that scatterer. Therefore, it can be seen that whether we seek to solve an inverse source problem, or an inverse scattering problem to calculate material properties of a scatterer, the currents (whether or not equivalent) are fundamental to the process of design and characterization.

To this end, we believe that to use the EI framework to design and characterize radiators in the best manner, the focus should be on how to implement (for design) or discover (for characterization) the appropriate current distribution (whether or not equivalent). Since these currents generate the incident field, total field, or the scattered field, they can be thought of as antennas for the problem of interest. For example, in the metasurface design approach discussed in this chapter, the equivalent surface currents are responsible for generating the desired far-field pattern (total field). On the other hand, the equivalent volumetric currents in the case of microwave imaging and dielectric lens design are responsible for generating the scattered field data that when added to the incident field data should result in the measured or desired data.

In the next sections within this chapter, we explain why we chose to contribute to the areas of metasurface design, microwave imaging, and dielectric lens/antenna design. We will also focus on how the aspect of solving for currents (either directly or indirectly) can show how these applications are related.

2.2 Design and Characterization using Surface Equivalence

As a starting point, let us consider the electromagnetic surface equivalence principle as explained in Section 1.3.1. This principle allows for the solution of a set of *surface* currents that supports a discontinuity between an output and input field. The output field distribution can be specified with measured or desired electromagnetic data depending

on the application. The surface currents can then be solved for using an EI algorithm with the constraint that the currents must produce the specified measured or desired electromagnetic data.

The idea of using inverse *source* algorithms that make use of the surface equivalence principle and solve for a specific set of surface currents is often seen in antenna characterization applications [15, 47–50]. For example, in near-field antenna measurement applications, an inverse source problem can be solved to reconstruct a set of surface currents that produce the measured data on a surface in the near field; these currents can then be used to calculate the far-field and other spatial properties of the antenna under test. We reiterate that we developed a multi-plane magnetic near-field antenna characterization using these principles in Appendix C. To this end, the use of the inverse source framework enabled us to be able to handle a non-canonical measurement domain.

However, let us now consider using this approach for design. We can also solve for a set of equivalent currents that produce desired electromagnetic data, however, the challenge lies in determining a way to physically implement them. For this reason we turn to the contemporary topic of metasurface design.

2.2.1 Metasurface Fundamentals

In recent decades, metamaterials have proposed to control and tailor electromagnetic waves [51, 52]. More recently, metasurfaces, which are the electrically thin version of metamaterials, have become popular because of their lower profile and loss properties when compared to metamaterials [6, 7, 53–55]. These planar devices can provide a systematic means of transforming an *input* electromagnetic field distribution to a desired *output* field distribution. They work by providing the necessary surface boundary conditions enabled by their subwavelength elements, i.e., metasurfaces can be viewed as an attempt to physically implement the electromagnetic equivalence principle to tailor electromagnetic fields (design) [2]. Metasurfaces have been used to achieve a variety of

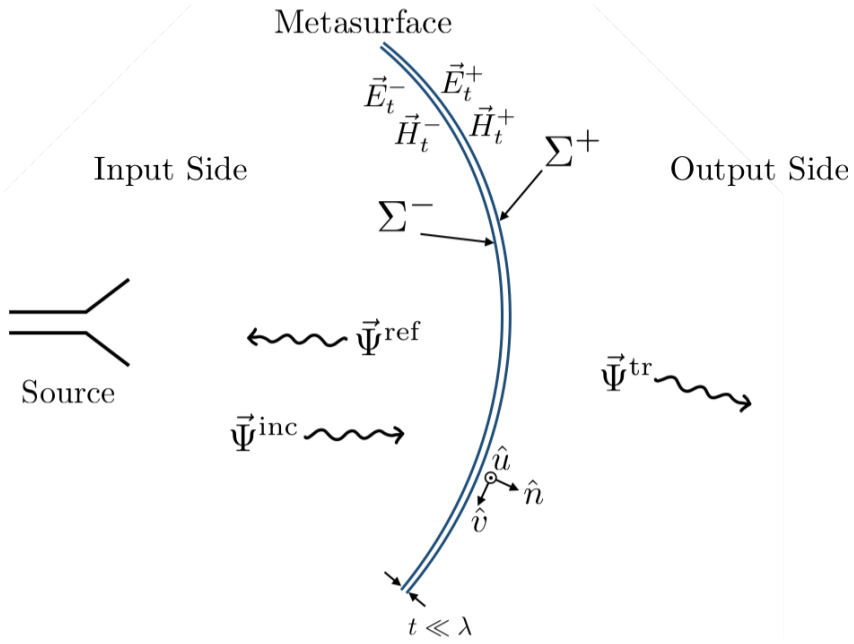

Figure 2.1: A transmitting metasurface. The input field, which is the sum of the incident and reflected fields ($\vec{\Psi}^{\text{inc}} + \vec{\Psi}^{\text{ref}}$) is transformed to an output field ($\vec{\Psi}^{\text{tr}}$) by a metasurface of subwavelength thickness. The metasurface can be designed if the tangential electric and magnetic fields ($\vec{E}_{\text{t}}^-$, $\vec{H}_{\text{t}}^-$, $\vec{E}_{\text{t}}^+$, $\vec{H}_{\text{t}}^+$) on the metasurface input boundary Σ^- and output boundary Σ^+ are known. This illustration is reprinted, with permission, from the one in [2, Figure 1] with minor modifications.

field transformations (e.g., reflection [56], refraction [54, 56], polarization control [57], absorption [58, 59]) for advanced applications such as cloaking [60], the development of smart radio environments [61]. In summary, due to their ability to achieve a variety of field transformations with their low profile and low loss properties, metasurfaces have the potential to impact wireless technology in the near future, and therefore we sought to contribute the area of metasurface design utilizing EI.

An illustration of a transmitting metasurface is shown in Figure 2.1. The *input* field is the addition of the incident field from a known source and the reflected field. The *output* field is the desired transmitted field on the other side of the metasurface.

Because metasurfaces are electrically very thin, they are often modelled as two-dimensional planar sheet discontinuities. Consequently, they cannot be described by the conventional

boundary conditions that describe the field discontinuity between two different types of media, and do not describe a sheet discontinuity in a medium [62, 63]. Instead, the generalized sheet transition conditions (GSTCs), which were developed by Idemen [64], can be used to model metasurfaces [65]. The full form of the GSTCs, shown in (2.1), relate the electromagnetic field differences across the metasurface (i.e., $\Delta\vec{H}$, $\Delta\vec{E}$, $\Delta\vec{D}$, and $\Delta\vec{B}$) to the electric and magnetic surface polarization densities ($\vec{P}^{\mathrm{e}}$ and $\vec{P}^{\mathrm{m}}$, respectively) of the metasurface:

$$\hat{n} \times \Delta\vec{H} = j\omega\vec{P}_t^{\mathrm{e}} - \hat{n} \times \nabla_t(\hat{n} \cdot \vec{P}^{\mathrm{m}}), \tag{2.1a}$$

$$\Delta\vec{E} \times \hat{n} = j\omega\mu_0\vec{P}_t^{\mathrm{m}} - \frac{1}{\epsilon_0}\nabla_t(\hat{n} \cdot \vec{P}^{\mathrm{e}}) \times \hat{n}, \tag{2.1b}$$

$$\hat{n} \cdot \Delta\vec{D} = -\nabla \cdot \vec{P}_t^{\mathrm{e}}, \tag{2.1c}$$

$$\hat{n} \cdot \Delta\vec{B} = -\mu_0 \nabla \cdot \vec{P}_t^{\mathrm{m}}. \tag{2.1d}$$

Note that $\hat{n}$ is the normal component to the metasurface (locally $\hat{n} = \hat{u} \times \hat{v}$ as in Figure 2.1), the subscript t specifies that the tangential components ($\hat{u}$ and $\hat{v}$) of the corresponding quantity are required, ω is the angular frequency of operation, $\vec{D}$ is the electric flux density, $\vec{B}$ is the magnetic flux density, and ϵ_0 and μ_0 are the permittivity and permeability of free space, respectively. The '∇_t' operator calculates the gradient with respect to tangential directions only and the 'Δ' operator can be defined in terms of the transmitted, incident, and reflected fields on the metasurface input and output boundaries [63] (see Figure 2.1)

$$\Delta\vec{\Psi} \triangleq \vec{\Psi}^{\mathrm{tr}}|_{\Sigma^+} - \left(\vec{\Psi}^{\mathrm{inc}}|_{\Sigma^-} + \vec{\Psi}^{\mathrm{ref}}|_{\Sigma^-}\right). \tag{2.2}$$

Furthermore, it has been shown that a macroscopically valid relation for the electric and magnetic surface polarization densities can be written as [63]

$$\vec{P}^{\mathrm{e}} = \epsilon_0\overline{\overline{\chi}}_{\mathrm{ee}}\vec{E}_{\mathrm{av}} + \overline{\overline{\chi}}_{\mathrm{em}}\sqrt{\mu_0\epsilon_0}\vec{H}_{\mathrm{av}}, \tag{2.3a}$$

$$\vec{P}^{\mathrm{m}} = \overline{\overline{\chi}}_{\mathrm{mm}}\vec{H}_{\mathrm{av}} + \overline{\overline{\chi}}_{\mathrm{me}}\sqrt{\frac{\epsilon_0}{\mu_0}}\vec{E}_{\mathrm{av}}, \tag{2.3b}$$

where $\overline{\overline{\chi}}_{\mathrm{ee}}$, $\overline{\overline{\chi}}_{\mathrm{mm}}$, $\overline{\overline{\chi}}_{\mathrm{em}}$, and $\overline{\overline{\chi}}_{\mathrm{me}}$ are the electric or magnetic (first subscript) surface susceptibility tensors that define the metasurface's response to electric or magnetic (second subscript) field excitations [63, 66]. Note that the field quantities are truly those at the position of the metasurface, but they are approximated as the average fields on the input and output metasurface boundaries [62], i.e.

$$\vec{\Psi}_{\mathrm{av}} \triangleq \frac{\vec{\Psi}^{\mathrm{tr}}|_{\Sigma^+} + \left(\vec{\Psi}^{\mathrm{inc}}|_{\Sigma^-} + \vec{\Psi}^{\mathrm{ref}}|_{\Sigma^-}\right)}{2}. \tag{2.4}$$

In order to simplify the GSTC expressions, it is often assumed that the normal components of the electric and magnetic polarization currents are zero [63]. In doing so, the spatial derivatives in (2.1a) and (2.1b) go to zero. Then, by combining (2.3) and (2.1) the GSTCs can be simplified to [2, 63]

$$\begin{aligned}\begin{pmatrix} -\Delta H_v \\ \Delta H_u \end{pmatrix} &= j\omega\epsilon_0 \begin{pmatrix} \chi_{\mathrm{ee}}^{uu} & \chi_{\mathrm{ee}}^{uv} \\ \chi_{\mathrm{ee}}^{vu} & \chi_{\mathrm{ee}}^{vv} \end{pmatrix} \begin{pmatrix} E_{u,\mathrm{av}} \\ E_{v,\mathrm{av}} \end{pmatrix} \\ &\quad + j\omega\sqrt{\epsilon_0\mu_0} \begin{pmatrix} \chi_{\mathrm{em}}^{uu} & \chi_{\mathrm{em}}^{uv} \\ \chi_{\mathrm{em}}^{vu} & \chi_{\mathrm{em}}^{vv} \end{pmatrix} \begin{pmatrix} H_{u,\mathrm{av}} \\ H_{v,\mathrm{av}} \end{pmatrix},\end{aligned} \tag{2.5a}$$

$$\begin{aligned}\begin{pmatrix} -\Delta E_u \\ \Delta E_v \end{pmatrix} &= j\omega\mu_0 \begin{pmatrix} \chi_{\mathrm{mm}}^{vv} & \chi_{\mathrm{mm}}^{vu} \\ \chi_{\mathrm{mm}}^{uv} & \chi_{\mathrm{mm}}^{uu} \end{pmatrix} \begin{pmatrix} H_{v,\mathrm{av}} \\ H_{u,\mathrm{av}} \end{pmatrix} \\ &\quad + j\omega\sqrt{\epsilon_0\mu_0} \begin{pmatrix} \chi_{\mathrm{me}}^{vv} & \chi_{\mathrm{me}}^{vu} \\ \chi_{\mathrm{me}}^{uv} & \chi_{\mathrm{me}}^{uu} \end{pmatrix} \begin{pmatrix} E_{v,\mathrm{av}} \\ E_{u,\mathrm{av}} \end{pmatrix}.\end{aligned} \tag{2.5b}$$

Note that the degrees of freedom in a metasurface design is related to these surface susceptibility values. However, when we limit ourselves to reciprocal metasurfaces, the degrees of freedom are reduced as we also need to satisfy [67]

$$\overline{\overline{\chi}}_{\mathrm{ee}}^{T} = \overline{\overline{\chi}}_{\mathrm{ee}}, \quad \overline{\overline{\chi}}_{\mathrm{mm}}^{T} = \overline{\overline{\chi}}_{\mathrm{mm}}, \quad \overline{\overline{\chi}}_{\mathrm{me}}^{T} = -\overline{\overline{\chi}}_{\mathrm{em}}, \tag{2.6}$$

where the superscript T denotes the transpose operator. In addition, if we would like to satisfy the conditions for lossless and passive metasurfaces, we need to have [63, 67]

$$\overline{\overline{\chi}}_{\mathrm{ee}}^{T} = \overline{\overline{\chi}}_{\mathrm{ee}}^{*}, \quad \overline{\overline{\chi}}_{\mathrm{mm}}^{T} = \overline{\overline{\chi}}_{\mathrm{mm}}^{*}, \quad \overline{\overline{\chi}}_{\mathrm{me}}^{T} = \overline{\overline{\chi}}_{\mathrm{em}}^{*}, \tag{2.7}$$

where the superscript $*$ denotes the complex conjugate operator.

In the next sections, we explain how metasurfaces can be designed using the inverse source *and* inverse scattering techniques.

2.2.2 Metasurface Design Using Inverse Source

According to (2.5), if one knows the incident, reflected, and desired transmitted fields on the metasurface boundaries, we can use the GSTCs to calculate the surface susceptibility profile that is required to implement the metasurface.[1] However, the desired transmitted field is not always known on the output boundary of the metasurface. For example, in many applications such as mobile communication, the far-field radiation pattern of the antenna is most important. In these cases, one may be able to use modal expansion methods to back-propagate the desired data to the output boundary of the metasurface, however, it is difficult to use these methods if the desired data is not on a canonical surface, if only phaseless desired data are known, or if only far-field criteria such as main beam direction and/or null locations are known [2]. Instead, we have recently showed that we can use the EI framework to solve an inverse source problem to find the desired transmitted field on the output boundary of the metasurface [2]. Then the GSTCs can be used to calculate the surface susceptibility profile that will represent the metasurface.

To clarify this from the EI standpoint, in [2], we used the flexibility of the EI framework to develop a metasurface design methodology that could make use of a variety of electromagnetic data including complex magnetic field data, phaseless magnetic field data,

[1] In this work, we showed the GSTCs written in terms of surface susceptibilities, but they may also be represented with surface impedances and polarizabilities [7, 56].

and far-field criteria to calculate the property of interest which was the transmitted field on the output boundary of the metasurface ($\vec{E}^{\text{tr}}|_{\Sigma^+}$ and $\vec{H}^{\text{tr}}|_{\Sigma^+}$). This method also allows us to make use of arbitrarily shaped surfaces/regions for the locations of the desired data and metasurface shape. As this work was a precursor to the work in Chapter 3, an overview of the methods taken are presented next.

The main steps taken to solve the EI problem in [2] to calculate the desired transmitted field on the output metasurface boundary were outlined in Section 1.4.4. We presented design algorithms for three cases wherein the desired electromagnetic data was specified as: complex tangential electromagnetic data, phaseless data, or far-field criteria (such as main beam direction and half-power beam width) [2, Section VII]. The property of interest in all these cases was the tangential transmitted field on the output boundary of the metasurface ($\vec{E}^{\text{tr}}|_{\Sigma^+}$ and $\vec{H}^{\text{tr}}|_{\Sigma^+}$), or equivalently, the electric and magnetic current densities on the output metasurface boundary ($\vec{J}|_{\Sigma^+}$ and $\vec{M}|_{\Sigma^+}$, respectively) contingent on the enforcement of Love's condition.[2] To obtain a physical model/operator to map the sought-after currents to the different types of electromagnetic data, we first needed an operator ($\mathcal{G}$) to map the currents to fields [2]. To this end, we used the electric field integral equations[3] (EFIE) [47], which in the full three-dimensional case, can be expressed as [35]

$$\begin{aligned}\mathcal{G}(\vec{J},\vec{M}) = &- j\eta_0 k_0 \int\limits_{\Sigma^+} \left[\vec{J}(\vec{r}\,') + \frac{1}{k_0^2}\nabla\nabla'_s \cdot \vec{J}(\vec{r}\,')\right] g(\vec{r},\vec{r}\,')ds' \\ &- \nabla \times \int\limits_{\Sigma^+} \vec{M}(\vec{r}\,')g(\vec{r},\vec{r}\,')ds' \end{aligned} \tag{2.8}$$

where $\vec{r}$ is a position vector belonging to the desired data domain/surface and $\vec{r}\,'$ is a position vector on Σ^+. The operators '$\nabla\times$' and '∇' are the curl and gradient operator, respectively, while '$\nabla'_s\cdot$' is the surface divergence operator with respect to the $\vec{r}\,'$ coordinates. Finally, $g(.,.)$ is the Green's function, η_0 is the wave impedance, and k_0 is the

[2]Note that in this method we are focused on calculating a set of equivalent currents for the purposes of design utilizing the surface equivalence principle.

[3]If the operator mapping to magnetic field data is required, one can use the EFIE with the principle of duality [11].

wavenumber all in free space. The operator $\mathcal{G}$ can also then be used to map the currents to phaseless data if necessary [2, Section VI-VII]. Finally, the data misfit cost functional $\mathcal{C}$ is constructed as

$$\mathcal{C}(\vec{J},\vec{M}) = \left\| \mathcal{L}(\mathcal{G}(\vec{J},\vec{M})) - \mathcal{K}(S^{\text{des}}) \right\|_2^2, \tag{2.9}$$

where $\|.\|_2$ denotes the L_2-norm which is defined over the desired data domain/surface on which the desired specifications are defined [2]. In (2.9), $\mathcal{L}(\mathcal{G}(\vec{J},\vec{M}))$ is an operator that maps the fields (obtained through $\mathcal{G}(\vec{J},\vec{M})$) to the form of the provided desired data. For example, $\mathcal{L}(\mathcal{G}(\vec{J},\vec{M}))$ might map currents to phaseless electric field data.[4] The operator $\mathcal{K}(S^{\text{des}})$ maps the desired data S^{des} to a form that can be used in the inversion algorithm. For example, if S^{des} is given as phaseless data, it can be used directly, but if far-field criteria are specified, it must be converted to some form of complex or phaseless field data before it can be inverted [2, Section VI]. Finally we minimize (2.9) with respect to the property of interest using analytically derived gradients and the appropriate regularization i.e.,

$$\text{appropriate } (\vec{J},\vec{M}) = \underset{\vec{J},\vec{M}}{\text{argmin}} \left\{ \mathcal{C}(\vec{J},\vec{M}) \right\}. \tag{2.10}$$

Note that during this process, we enforce Love's condition using a virtual point method, i.e., we create a virtual surface that is inwardly offset with respect to Σ^+ (i.e. towards input side of the metasurface), and then enforce zero tangential electric/magnetic fields on this virtual surface when solving for $\vec{J}$ and $\vec{M}$. (For details, see [35].) The points on the virtual surface can be thought of as additional desired field data points where we want the tangential electric field to be zero. Enforcing Love's condition during the inversion process ensures these currents can be related directly to the output field on the output boundary of the metasurface Σ^+ as

$$\vec{H}_t^+ = -\hat{n} \times \vec{J} \qquad \text{and} \qquad \vec{E}_t^+ = \hat{n} \times \vec{M}. \tag{2.11}$$

[4] As expected, in this inverse source problem mapping sources to the electromagnetic data has the same form as that shown in (1.8).

Now that we know the transmitted fields on Σ^+, we can use the GSTCs to calculate the surface susceptibility profile to design the metasurface.

To show an example of what is possible with this inversion method, let us briefly show the metasurface design example from [2, Section IX]. In this example, the goal was to design a metasurface that was 10λ in length (λ is the free-space wavelength) and discretized into $\lambda/6$ subwavelength element segments. Therefore, there were 60 reconstruction points and a total of 120 unknowns (60 for $\vec{J}$ and 60 for $\vec{M}$). Note that if we are using the GSTCs to design a metasurface in this manner, it is assumed that it has zero thickness. The incident field is a 'tapered' normally incident transverse electric (TE_z) plane wave, i.e., the z-component of the magnetic field (H_z) amplitude of the plane wave is 1 A/m for 14λ (past the extents of the metasurface) and decays linearly to zero thereafter.[5] Additionally, the reflected field was assumed to be zero. The desired far-field power pattern was generated by an array of 13 $\hat{z}$-directed elementary dipoles that were uniformly spaced on a 6λ line. The power pattern of H_z produced by this array was calculated on a semicircular region of radius 500λ from $-90^\circ \leq \varphi \leq 90^\circ$ as shown in Figure 2.2 where φ is in the spherical coordinate system. At this point in the design process, the incident field and reflected field are known on the metasurface input boundary and the desired phaseless magnetic far-field is known. To design the metasurface, we use the inverse source method outlined above, by constructing the appropriate cost functional and minimizing this cost functional with respect to the electric and magnetic currents on Σ^+ while enforcing Love's condition [2]. Next we calculate the fields from the currents according to (2.11), and use the GSTCs to solve for the susceptibilities. We simulated the designed metasurface using a full-wave finite difference frequency domain solver that was capable of simulating the GSTC boundary conditions (FDFD-GSTC) developed by Vahabzadeh et. al. [66]. The magnitude of H_z at a moment in time from this simulation is shown in [2, Figure 8]. The far-field pattern was then calculated by propagating the near-field to the far-field. This far-field is shown in Figure 2.2. It can be seen that the far-field generated by

[5] This was done to reduce interaction between the plane wave and the perfectly matched layer boundary conditions in the simulation and therefore avoid numerical error during the verification process [2].

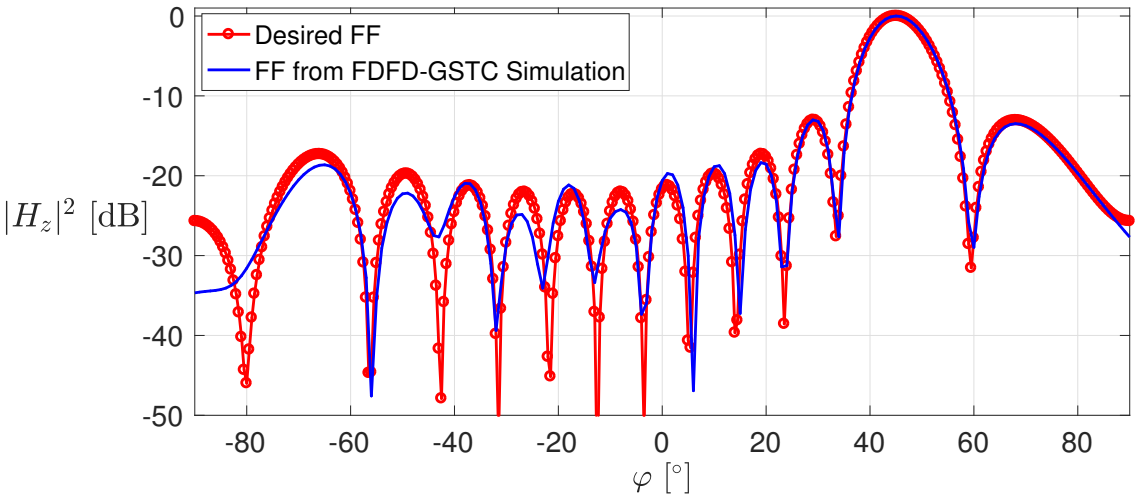

Figure 2.2: A comparison of the normalized far-field (FF) power pattern (phaseless) produced by the FDFD-GSTC simulation of the designed metasurface (solid blue curve) and the desired power pattern (solid red curve with circular markers). This figure also appears in [2] © 2019 IEEE.

the designed metasurface when interrogated by the planewave closely follows the desired phaseless pattern.

The method presented in [2] enabled a flexible way of designing metasurfaces for a variety of different types of electromagnetic data. However, it did not address power conservation. Although the results in [2] show that the designed metasurfaces were able to accurately meet the desired electromagnetic data, the power efficiency of the transformations were low due to the need for lossy subwavelength elements. For example, in the phaseless example shown in Figure 2.2, the efficiency was 17.0%. To address this, an additive regularization method was developed to enforce local power conservation in [68]. By enforcing local power conservation [69], the time average output and input power normal to the metasurface at each subwavelength element is ideally set to be equal. This ensures that there is no loss or gain at each element composing the metasurface. In this way, efficient passive and lossless metasurfaces can be designed.

2.2.3 Metasurface Design Using Inverse Scattering

Metasurfaces can also be designed using an inverse scattering approach as will be demonstrated in Chapter 3. To understand how the metasurface design problem can be viewed as an inverse scattering problem, one can compare the full form of the GSTCs in (2.1a) and (2.1b) to (1.9). We remind the reader that in Section 1.4.1 we stated that inverse scattering problems have some means of mapping currents to the material property of interest, i.e. $U_{\text{sources}} = \mathcal{K}(X_{\text{mater}})$. It can be seen that the left hand side of (2.1a) and (2.1b) are simply the surface currents supported by the metasurface (see the boundary condition equations in (3.6)). Additionally, keeping in mind that the electric and magnetic surface polarization densities are functions of the surface susceptibilities (see (2.3)), we have a mapping from the unknown surface susceptibilities to the surface currents supported by the metasurface.[6] Note that posing the metasurface design problem as an inverse scattering problem allows for the direct solution of the surface susceptibility profile or related parameters. This was done in [39] where the surface impedances, admittances and magneto-electric coupling parameters are found to satisfy far-field criteria.[7]

Note that up until now we have been assuming an ideal, zero-thickness (single layer) model for the metasurface. However, it has been shown that metasurfaces are typically implemented as multi-layered printed circuit boards, e.g., see the three-layered dogbone structures shown in [70]. This is due to the required degrees of freedom to enable such transformations.[8] These types of metasurfaces can not be directly designed with the above inverse source approaches.

[6]These currents are actually supported by the metasurface (internal) and should not be confused with the output currents/fields (aperture) on the metasurface boundary Σ^+ that we solved for in (2.11). Note that this can be seen as another example of the volume equivalence principle that was described in 1.3.2, but for a surface because we are dealing with a 2D scatterer.

[7]The surface impedances, admittances and magneto-electric coupling parameters serve the same purpose as the surface susceptibilities; they both describe the relation between the surface currents supported by the metasurface to the fields on the metasurface.

[8]If we want to transform complex input fields $\vec{E}_1$ and $\vec{H}_1$ to complex output fields $\vec{E}_2$ and $\vec{H}_2$ we need four degrees of freedom. Assuming local power conservation for the design of passive, lossless and reflectionless metasurfaces, we have three degrees of freedom [68] (see Section 2.2.1).

Multi-layer metasurfaces can be approximately modelled with a circuit-based modelling technique. The metasurface is seen as a set of adjacent two-port network [71] models that are composed of circuit elements representing the different layers in each subwavelength element; it is assumed that the metasurface is composed of dielectric layers (e.g., for substrate and bondply) and admittance layers (representing the metal trace of a subwavelength element). The circuit admittances are often the parameters that are tuned to design the metasurface, i.e., the dielectric layers are consistent throughout the metasurface and only the admittance of each metasurface element is tuned. This is explained in detail in Chapter 3.

Note that modelling the metasurface in this way allows for the mapping of the unknown circuit admittances (material property of interest) to the electric and magnetic surface current densities on the output boundary of the metasurface. In Chapter 3, we demonstrate an inverse scattering approach that uses this simplified model for the metasurface to solve directly for the circuit admittances. This approach also adds the ability to add constraints directly to the circuit admittances during the inversion process, this can facilitate the design of the subwavelength elements needed to physically implement the metasurface.

2.3 Design and Characterization by Volume Equivalence

Metasurfaces are a means to support surface currents that can tailor electromagnetic fields, i.e., they can be seen as a method to physically implement the surface equivalence principle. However, most antennas/scatterers are not so electrically thin that they can be analyzed as metasurfaces.[9] Additionally, there are many cases where the internal electromagnetic properties of a radiator need to be analyzed or synthesized, (e.g., in

[9]It may also be beneficial to model metasurfaces as having finite thickness as they do so in reality. Metasurface circuit models do this, however, more accurate full-wave physics solvers may also be used in the future so mutual coupling between layers can be taken into account.

the application of microwave imaging the complex dielectric profile of volume scatterers are the property of interest). For these cases, and cases where perfect electric/magnetic conductors are not the only radiators, surface current approaches may not be sufficient.

Instead, we can look to use the volume equivalence principle to model antennas/scatterers where some internal properties of the scatterer are required. The volumetric equivalent currents are related to the electromagnetic data as in (1.8), and also related to the property of interest as in (1.9). This is demonstrated in Section 1.3.2 where the equivalent currents that radiate the scattered fields are a function of the relative permittivity and permeability. Therefore, using these equivalent currents, we can develop an inverse scattering problem to solve for the property of interest from the measured/desired electromagnetic data.

The above methods are often used for the applications of microwave imaging and dielectric lens/antenna design. Next we present a brief overview of these applications to ready the reader for later chapters.

2.3.1 Microwave Imaging: Characterization by Volumetric Currents

In microwave imaging (MWI), the property of interest is often the complex dielectric profile in a region of interest (i.e., investigation domain) referred to as the imaging domain $\mathcal{D}$. The electromagnetic data that are to be processed in the inversion algorithm are the electric and/or magnetic field data collected by receivers on a measurement domain $\mathcal{S}$ outside $\mathcal{D}$. The electromagnetic data are generated by successively illuminating the targets in $\mathcal{D}$ by transmitters and collecting the resulting total electric and/or magnetic field data for each transmitter at the receivers. The same experiment is also often repeated without any targets in $\mathcal{D}$ to collect the incident field on the measurement domain. The resulting scattered field data, where the scattered field is the difference of the total and incident fields (e.g., in the case of electric fields: $E^{\text{scat}} = E - E^{\text{inc}}$), is then given to

an inverse scattering algorithm[10] that processes the data and reconstructs the complex dielectric profile in the $\mathcal{D}$. Because $\mathcal{S}$ is external to $\mathcal{D}$, MWI is inherently non-destructive and the frequencies that are used are non-ionizing. This makes MWI an active area of study for many applications such as biomedical imaging, non-destructive testing and many more [23, 74–76]. A typical MWI setup is shown in Figure 2.3, where a set of co-resident transceivers are located on a ring surrounding the imaging domain.

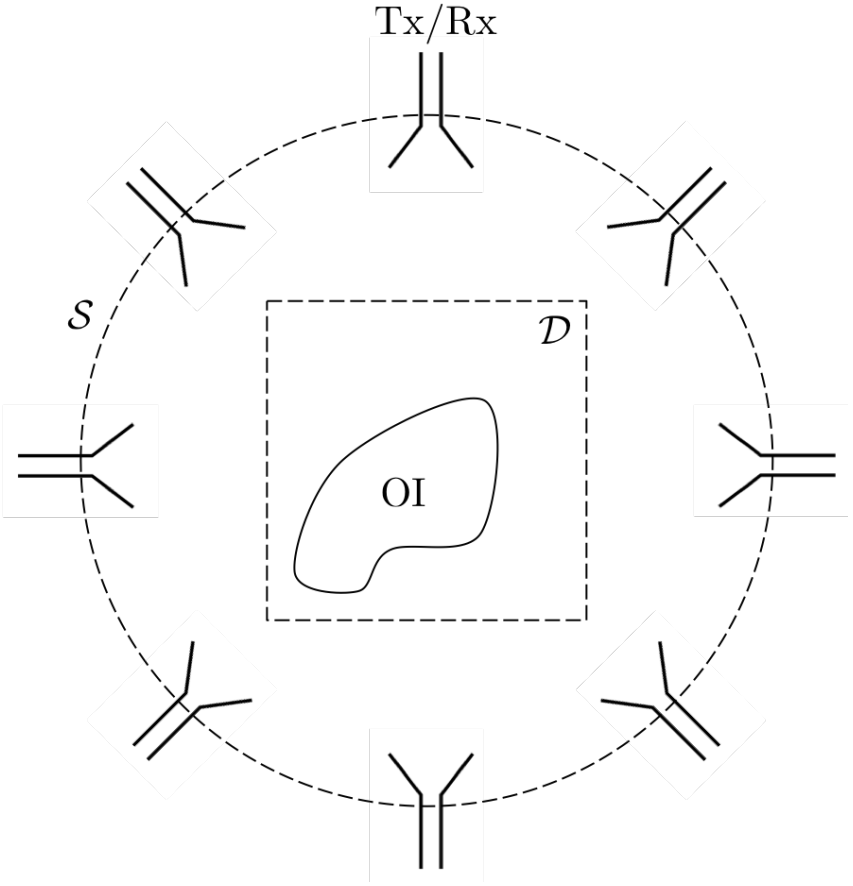

Figure 2.3: A typical MWI apparatus. A set of co-resident transceivers (Tx/Rx) are on the measurement/data domain $\mathcal{S}$ surrounding the imaging domain $\mathcal{D}$. The property of interest is the complex dielectric profile in the $\mathcal{D}$. Analyzing the reconstructed dielectric profile often provides valuable information on the targets or objects of interest (OIs) in $\mathcal{D}$.

[10]Another approach in microwave imaging is to use radar-based techniques, e.g., see [72, 73]. The radar approach is not within the scope of this thesis.

To understand how the application of MWI can be set up as an electromagnetic inverse problem, consider the data equation for a non-magnetic, homogeneous background [19, 77]

$$E^{\text{scat}}(\mathbf{r} \in \mathcal{S}) = k_b^2 \int_{\mathcal{D}} g(\mathbf{r} \in \mathcal{S}, \mathbf{r}' \in \mathcal{D}) E(\mathbf{r}' \in \mathcal{D}) \frac{\epsilon_r(\mathbf{r}' \in \mathcal{D}) - \epsilon_b}{\epsilon_b} d\mathbf{r}' \tag{2.12}$$

that maps the relative permittivity of the scatterers in $\mathcal{D}$ to the scattered field on the measurement domain $\mathcal{S}$ for a typical tomographic (2D) MWI configuration. Here, $g(\mathbf{r}, \mathbf{r}')$ is the two dimensional Green's function of the background medium that has a relative permittivity ϵ_b. There are two unknowns: $E(\mathbf{r}')$, the total field in $\mathcal{D}$, and the (property of interest) relative permittivity $\epsilon_r(\mathbf{r}')$ in $\mathcal{D}$. Finally k_b is the wavenumber of the background medium. It is instructive to note that contrast sources that represent the volumetric currents that generate the scattered field as described by volume equivalence principle can be defined as

$$W(\mathbf{r}' \in \mathcal{D}) = E(\mathbf{r}' \in \mathcal{D}) \frac{\epsilon_r(\mathbf{r}') - \epsilon_b}{\epsilon_b}. \tag{2.13}$$

Therefore, we can rewrite (2.12) as producing a scattered field due to a set of contrast sources. Also, $E(\mathbf{r}' \in \mathcal{D})$ is itself related to $\epsilon_r(\mathbf{r}')$ and the incident field E^{inc} via the domain equation [19, 77]:

$$E(\mathbf{r}' \in \mathcal{D}) = E^{\text{inc}}(\mathbf{r}' \in \mathcal{D}) + k_b^2 \int_{\mathcal{D}} g(\mathbf{r}' \in \mathcal{D}, \mathbf{r}'' \in \mathcal{D}) E(\mathbf{r}'' \in \mathcal{D}) \frac{\epsilon_r(\mathbf{r}'' \in \mathcal{D}) - \epsilon_b}{\epsilon_b} d\mathbf{r}''. \tag{2.14}$$

We can see that with (2.12), (2.13), and (2.14) we have a means of relating sources to the electromagnetic data, and the sources to the property of interest as in all inverse scattering problems. Another advantage with using these equations are that they are full wave, and so they take into account mutual coupling and multiple scattering as opposed to simpler models such as the circuit model we used to approximately model a muti-layer metasurface. Therefore, by using this formulation, we may be able to more accurately characterize and design antennas.

In order to calculate the dielectric profile, many inverse scattering algorithms have been put forth that utilize the data equation, domain equation, different approximations of

$E(\mathbf{r}')$, optimization methods, and regularization schemes (some examples of the vast amount of inverse scattering methods are found in [19, 30, 78, 79]). In Chapter 4 we use the flexibility of the EI framework to develop phaseless Gauss-Newton inversion algorithms that can be used with microwave imaging. In this work phaseless data are used on $\mathcal{S}$ to reconstruct the relative permittivity in $\mathcal{D}$. Note that measuring phaseless data generally requires less expensive equipment compared to measuring data with phase.

2.3.2 Dielectric Lens/Antenna Design: Design by Volumetric Currents

Inverse scattering algorithms can also be used to *design* dielectric objects in $\mathcal{D}$. Instead of using *measured* data collected at the receivers in Figure 2.3, we can instead provide the inverse scattering algorithm with *desired* data. From this point, many of the same algorithmic techniques that can be used to solve MWI problems can be used to design dielectric profiles in $\mathcal{D}$. This application is especially logical as the non-uniqueness that is problematic in the imaging case, can be advantageous in the case of design (*e.g.* the availability of different dielectric profiles for a single set of desired data may facilitate dielectric lens fabrication).[11] Recently, research on inverse scattering for design of dielectric lenses, cloaks, etc has been reported [9, 22, 80, 81].

As was previously shown in [2], it is often beneficial to be able to make use of a variety of electromagnetic data to solve for the property of interest. To this end, in [82] we briefly explored using the phaseless Gauss-Newton inversion algorithm that was developed for Chapter 4 for dielectric lens design. However, to further increase the variety of electromagnetic data that is available for use in the inversion process and to increase the capability of the dielectric lens/antenna designer, in Chapter 5 we present a novel combined inverse source and scattering technique to design dielectric lens antennas. This

[11] There is a trade-off that occurs here, the once issue of non-uniqueness may be an advantage for design, but now the issue of existence presents itself. There may not be a dielectric profile that can do what the designer desires.

technique is capable of using multiple inverse scattering algorithms, is capable of utilizing complex, phaseless, and far-field criteria data in the inversion process, and can design passive, lossless and reflectionless lenses.

2.4 Summary

In this chapter, we briefly described the antenna design and characterization applications addressed in this thesis. All these applications are connected in their direct or indirect solution of a set of sources that relate to the electromagnetic data through EI; if an inverse scattering problem is being solved, then the material parameters of the scatterer are in turn related to the sources contributing to the electromagnetic data.

First we contributed to the area of metasurface design using an inverse source, then inverse scattering method to be able to directly design the admittance layers of the metasurface. Then, to continue to more directly design and characterize electrically thicker scatterers, we moved to the areas of microwave imaging and dielectric lens/antenna design. In the next chapter, we present our EI algorithm that is capable of designing the admittance layers of a metasurface in more detail.

Chapter 3

Multi-Layer Metasurface Design Using An Inverse Scattering Technique

Preface

In this chapter, we present an EI algorithm for the purpose of metasurface design. As mentioned in Section 2.2, metasurfaces are a way to physically implement the surface equivalence principle to tailor electromagnetic fields. Previously, we presented an inverse source method to design these surfaces (see Section 2.2.2 and [2]), but we could not directly design multi-layer metasurfaces or any material parameters directly using this method. To this end, in this work we present an electromagnetic inversion scattering algorithm that can design the circuit admittances of a three-layer admittance metasurface directly. Because we are directly solving for the material parameters of the metasurface, this can be considered as an inverse scattering approach. This can be seen in Section 3.4 as the *circuit model* allows us to relate the circuit admittances to the output/aperture

field of the metasurface (this output field can be interpreted as sources that radiate) and the *field model* relates the sources on the output side of the metasurface aperture to the electromagnetic data.

From the standpoint of the common methodology outlined in Section 1.4.4, the electromagnetic data are the desired complex or phaseless magnetic field on a desired data domain somewhere external to the output side of the metasurface. The property of interest are the circuit admittances of the metasurface when a three admittance layer design is utilized as developed from the research in [43, 70, 83–85]. The physical model is based on approximating each metasurface unit cell as a layered circuit model, and then using an integral formulation of Maxwell's equations to relate the output field of the metasurface to the desired tangential complex magnetic field at the required locations. The physical model is used to construct a data-misfit cost functional, and subsequently, it is minimized with respect to the property of interest using a gradient-based process.

The main contribution of this work is that to the best of the authors' knowledge, this is the first time a gradient-based metasurface design algorithm has been developed that can directly provide the required circuit admittances needed to implement a passive lossless metasurface given a desired complex or phaseless far-field pattern, i.e., we can directly constrain the admittance profile of the metasurface. The material presented in this chapter was published as a journal paper for IEEE Transactions on Antennas and Propagation [38].[1]

Abstract

A gradient-based optimization algorithm is presented that is capable of directly designing a metasurface at the circuit parameter level for a desired field (amplitude and phase) pattern or a desired power (phaseless) pattern on some region of interest (ROI) external

[1] © 2021 IEEE. Reprinted, with permission, from C. Narendra, T. Brown and P. Mojabi, "Gradient-Based Electromagnetic Inversion for Metasurface Design Using Circuit Models," in *IEEE Transactions on Antennas and Propagation*, doi: 10.1109/TAP.2021.3118811.

to the metasurface boundary. Specifically, the inversion algorithm designs the microwave admittance profile of each subwavelength element of the metasurface when a three-layer admittance model is assumed. To this end, a forward model is developed that maps the admittance profile of each layer of the metasurface to the desired field on the ROI. Then, for the inverse design problem, a data misfit cost functional is defined and minimized over the unknown admittance profile using analytically derived gradients and step lengths. The developed inversion algorithm is then utilized to design metasurfaces capable of beam forming in the far-field zone.

3.1 Introduction

Metasurfaces are devices of subwavelength thickness that are capable of systematically transforming an incoming electromagnetic field distribution to a desired outgoing field distribution [8, 54, 65, 86–88]. This is made possible by the lattice of subwavelength elements that comprise the metasurface. Metasurfaces enable the implementation of a vast amount of field transformations such as controlling reflection [56], refraction [54, 56], absorption [89, 90], polarization transformation [57], and much more. These abilities can then facilitate many applications such as tailoring radiation patterns of antennas [91], cloaking [60], and the development of smart radio environments [61].

In order to utilize metasurface technology towards different applications, general design methodologies are needed and some have recently been proposed [6, 7]. In these approaches, the tangential electromagnetic field components present on the input and output boundaries of the metasurface are required. (For a discussion on the normal components, see [92].) Once these fields have been defined, the generalized sheet transition conditions (GSTCs) [65] are used to calculate either the surface impedance [7], susceptibility [6], or polarizability [56] profiles that represent the discontinuity needed to support the specified field transformation assuming a metasurface of zero-thickness. In this paper, we will refer to these quantities as GSTC parameters.

In the general design methodologies mentioned above, a procedure for relating desired field specifications (e.g., power pattern, main beam direction, null directions, etc.) somewhere external to the metasurface (e.g., in the far-field zone) to the fields on the output boundary of the metasurface is not described. The development of such a link would promote the use and design of metasurfaces because the field on the output boundary of the metasurface is not always known; rather, a set of specifications on a region somewhere external to the metasurface is what is important and typically known to the designer. For example, many antenna applications require specific far-field patterns such as nulls in desired directions or a specific half-power beamwidth (HPBW). To this end, in [2, 68, 93], the general metasurface design framework described above was extended to leverage electromagnetic inversion for design scenarios where different types of field specifications are required on a region of interest (ROI) external to the metasurface, e.g., in its far-field zone. This framework is referred to as inversion because it infers a cause (equivalent currents on the metasurface boundary) from an external effect (desired specifications). It was also demonstrated how this inversion framework can enable the design of passive and lossless metasurfaces by enforcing local power conservation (LPC) [69, 94] in the inversion process via augmenting the original cost functional with an extra term [68]. Therefore, the work in [2, 68] introduced a flexible field model to the metasurface design framework: using this framework, it is possible to infer the required output fields on the metasurface boundary from the knowledge of field specifications on a ROI. Thus, the required GSTC parameters can be obtained. However, this is usually not sufficient to complete the metasurface design process. Physically implementing a metasurface directly from its associated GSTC parameter profile is not done in practice, instead, the GSTC parameters are often transformed to microwave circuit parameters such as impedance, admittance, or scattering parameters [7, 43, 83–85, 95] so that the appropriate subwavelength metasurface elements can be designed in a separate step [7, 43].

Alternatively, instead of having equivalent currents as the unknowns of the inverse design problem, we may reformulate the problem such that its unknowns become the circuit parameters associated with different unit cells. To understand the advantage of such a

reformulation, let us assume that we desire to create a null in a certain direction using a metasurface to be later fabricated on a specific dielectric substrate (e.g., Rogers RO3010) and specific metallic trace geometry (e.g., dogbone traces [70, 85]).[2] Given the substrate and trace types, we often know beforehand the range of capacitance and inductance values [85] that can be supported. Therefore, if the inverse design can be done directly at the circuit parameter level, we will have the opportunity to limit the optimization space to those practically feasible capacitance and inductance values. On the other hand, if the inverse design is performed at the field level (i.e., optimizing over equivalent currents), it is not straightforward to impose such circuit-level constraints on field-level unknowns during the optimization process. As another example, when the inverse design is performed at the field level, ensuring a passive and lossless metasurface requires augmenting the cost functional by an extra LPC term [68]. On the other hand, at the circuit level, we can simply limit the search space to purely imaginary impedance values.

Herein, we make use of research introduced in [43, 70, 83–85] to model metasurfaces as an array of subwavelength elements composed of a network of circuit admittances in combination with concepts developed in [2, 68] to develop a forward model that can relate these microwave circuit parameters to the desired output field (amplitude and phase) or power (phaseless) pattern. Next, we use this forward model to develop a novel gradient-based electromagnetic inversion algorithm used to design a metasurface by directly optimizing the circuit admittance profile of the metasurface. This work aims to keep the flexibility of meeting desired field constraints external to the metasurface as well as facilitating the design of metasurface subwavelength elements. We begin by describing the general metasurface design problem in Section 3.2 as well as a brief description of the employed forward model and scope of this paper. Then, the problem statement is presented in Section 3.3. Next, the forward model is described in detail in Section 3.4

[2]Dogbone traces are a common choice to implement these admittance layers. This is partly due to the fact that their fabrication is relatively easy and they can be implemented with printed circuit board technology. To implement various admittance values the geometrical parameters of the dogbone trace, such as its height and width, are changed to create a lookup table. Once a lookup table is formed, it can be used for an initial design which then needs to be further optimized to take into account other effects such as mutual coupling.

and the novel inversion algorithm is presented in Section 3.5. Results are then shown and discussed in Section 5.4 wherein the developed inversion algorithm is used to design metasurfaces to meet desired field (amplitude and phase) or power (phaseless) patterns. Finally, we summarize this work in Section 3.7.

3.2 General Problem Description and Scope

The general metasurface design problem is shown in Figure 3.1. A metasurface separates two volumetric regions of space; the input side V^-, and the output side V^+. The source is in V^-, while the ROI, a fictitious region of space containing the set of desired field or power specifications lies in V^+. The known quantities of this problem are the incident field $\vec{\Psi}^{\text{inc}}$ produced by the source, the reflected field $\vec{\Psi}^{\text{ref}}$ (in our work we assume $\vec{\Psi}^{\text{ref}} = 0$) and the desired specifications on the ROI. The tangential fields on the metasurface boundaries are denoted by $\vec{E}_{\text{t}}^-$ and $\vec{H}_{\text{t}}^-$ on Σ^-, and $\vec{E}_{\text{t}}^+$ and $\vec{H}_{\text{t}}^+$ on Σ^+. The tangential coordinates on the metasurface are $\hat{u}$ and $\hat{v}$, while the outward facing normal direction is $\hat{n}$. (In this work, $\hat{u} = \hat{z}$, $\hat{v} = -\hat{y}$ and $\hat{n} = \hat{x}$.)

Microwave two-port networks normally relate an input voltage and current to an output voltage and current, and because $\vec{E}_{\text{t}}$ and $\vec{H}_{\text{t}}$ are analogous quantities, we can use these networks to model metasurface unit cells. Furthermore, the unit cells (and thus, the two-port networks) can be defined by a network of circuit elements as in [43, 84, 85]. Therefore, the output fields of a unit cell are related to the circuit elements that comprise that cell and the input fields. In this work, the unit cells will be composed of three parallel admittances which are optimized to meet the desired specifications. Thus, we can represent the output fields of each unit cell as a function of three admittances, $g(Y_1, Y_2, Y_3)$, as summarized in Figure 3.2. In the scope of this work, we assume a two-dimensional transverse-electric to the $\hat{z}$ direction (TE_z) design problem. Thus, the problem can be formulated based on H_z.

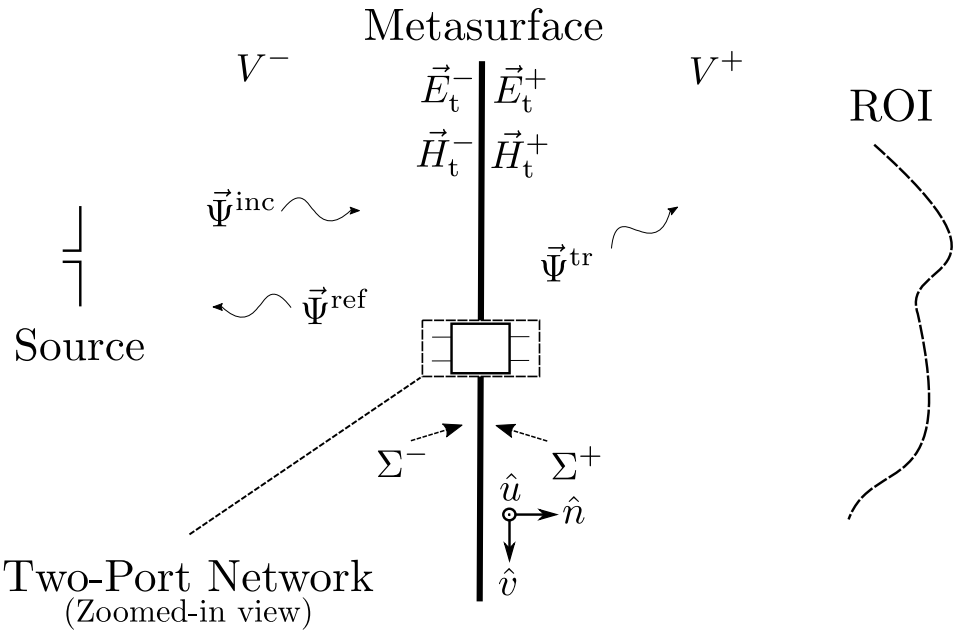

Figure 3.1: Overview of the metasurface design problem. The input and output surfaces of the metasurface are denoted by Σ^- and Σ^+. ROI denotes the region of interest which is the far-field zone in this paper. (Herein, $\hat{u} = \hat{z}$, $\hat{v} = -\hat{y}$ and $\hat{n} = \hat{x}$.)

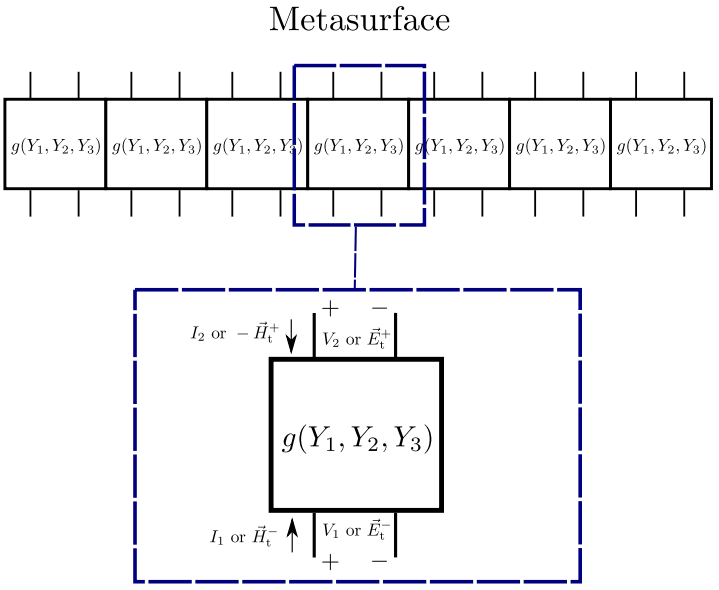

Figure 3.2: Each metasurface unit cell is modeled as a two-port network wherein the output of each network is dependent on the circuit parameters that comprise them. Note that Y_1, Y_2, and Y_3 can vary from unit cell to unit cell.

3.3 Problem Statement

Given (i) desired field (amplitude and phase) H_z or power (phaseless) $|H_z|^2$ specifications on the ROI, (ii) a known incident field, (iii) a known dielectric substrate, and (iv) a known dielectric bondply (adhesive), we attempt to determine the admittance profile of a passive, lossless, and reflectionless omega-type bianisotropic metasurface [94] to transform the incident field to an output field that meets the specifications on the ROI (as closely as possible).[3] Therefore, each unit cell consists of three unknown admittance values with two known dielectric substrates and one known dielectric bondply layer. Denoting the total number of unit cells by N, the admittance profile will then consist of $3N$ admittance values. That is, the problem is concerned with determining $3N$ unknowns from the desired specifications on the ROI.

3.4 Forward Model

To solve this inverse problem, we first need to build a forward model to relate a given admittance profile to the data on the ROI. Our forward model to be explained below is composed of a circuit and field model, see Figure 3.3.

3.4.1 Circuit model

Each subwavelength element of the metasurface is modeled as a two-port network composed of a network of three admittances. As in [43, 96], the three admittance layers are separated by dielectric layers. The three admittances are needed to obtain the degrees

[3]Note that since we have considered a TE_z configuration the problem has been formulated with respect to the H_z component.

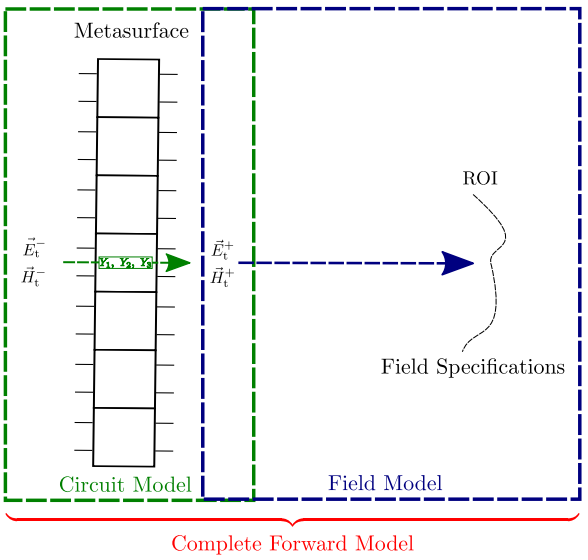

Figure 3.3: The full forward model used in this work is composed of two separate models: the circuit and field models, respectively.

of freedom necessary to match the input and output fields [43].[4] Note that this design facilitates physical implementation with two printed circuit boards: one board will have two trace layers (on either side of the substrate) and it can be bonded to another board with one trace layer.

To represent each unit cell as a two-port network, three layers of admittance elements can be linked in parallel with the dielectric layers as shown in Figure 3.4. The dielectric layers (dielectric substrate of the traces and bondply) can be modeled as transmission lines of length l. The wavenumber β and the characteristic impedance Z associated with these dielectric layers are then defined as

$$\beta = \frac{2\pi}{\lambda} = \frac{2\pi f\sqrt{\epsilon_r}}{c_0}, \qquad Z = \frac{\eta_0}{\sqrt{\epsilon_r}}, \tag{3.1}$$

[4]We note that for some applications it might be necessary to increase the degrees of freedom in design by adding a fourth admittance layer to the utilized unit cell, e.g., see [57, 97]. The overall methodology presented herein remains the same if an extra admittance layer is added, however, new gradient operators need to be found. Also, adding an extra admittance layer may increase the non-linearity of the optimization problem. Therefore, the chance of encountering inappropriate local minima can increase. Finally let us justify the use of three admittance layers. When we want to convert a given $(E,\ H)$ to desired fields we need a two-port transformation. A two-port matrix consists of four elements. Due to reciprocity one of these elements is dependent on the remaining three, thus having three degrees of freedom. Therefore three layers have been used.

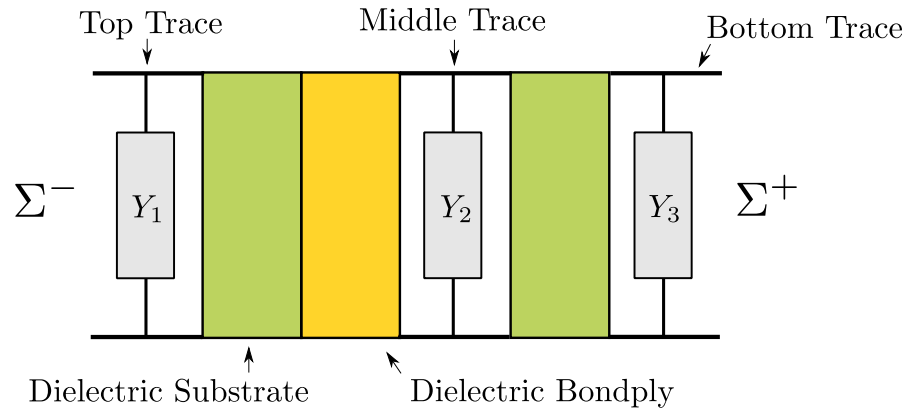

Figure 3.4: The two-port circuit model of the metasurface unit cells (not-to-scale).

where λ is the wavelength, f is the frequency of operation, c_0 is the speed of light in a vacuum, η_0 is the characteristic impedance of free space, and ϵ_r is the relative permittivity of the dielectric layer.

This two-port network can be represented with ABCD or transmission parameters [96] that represent how the input electric and magnetic field are transformed. To this end, the ABCD matrices of the individual layers comprising the metasurface unit cells are required. To model our entire unit cell, all the necessary individual ABCD matrices are

$$\begin{aligned}
\mathbf{T}_{Y_1} &= \begin{bmatrix} 1 & 0 \\ Y_1 & 1 \end{bmatrix}, \ \mathbf{T}_{Y_2} = \begin{bmatrix} 1 & 0 \\ Y_2 & 1 \end{bmatrix}, \ \mathbf{T}_{Y_3} = \begin{bmatrix} 1 & 0 \\ Y_3 & 1 \end{bmatrix}, \\
\mathbf{T}_{\text{sub}} &= \begin{bmatrix} \cos(\beta_{\text{sub}} l_{\text{sub}}) & jZ_{\text{sub}}\sin(\beta_{\text{sub}} l_{\text{sub}}) \\ \frac{j}{Z_{\text{sub}}}\sin(\beta_{\text{sub}} l_{\text{sub}}) & \cos(\beta_{\text{sub}} l_{\text{sub}}) \end{bmatrix}, \\
\mathbf{T}_{\text{bpl}} &= \begin{bmatrix} \cos(\beta_{\text{bpl}} l_{\text{bpl}}) & jZ_{\text{bpl}}\sin(\beta_{\text{bpl}} l_{\text{bpl}}) \\ \frac{j}{Z_{\text{bpl}}}\sin(\beta_{\text{bpl}} l_{\text{bpl}}) & \cos(\beta_{\text{bpl}} l_{\text{bpl}}) \end{bmatrix},
\end{aligned} \tag{3.2}$$

where $\mathbf{T}_{Y_1}$, $\mathbf{T}_{Y_2}$, and $\mathbf{T}_{Y_3}$ are the ABCD matrices of the admittances in each layer of the metasurface, $\mathbf{T}_{\text{sub}}$ is the ABCD matrix of the dielectric substrates, and $\mathbf{T}_{\text{bpl}}$ is the ABCD matrix of the bondply layer. Noting Figure 3.4, the total ABCD matrix for a metasurface

subwavelength element (unit cell) can be calculated as

$$\mathbf{T}_{\text{elem}} = \mathbf{T}_{Y_1}\,\mathbf{T}_{\text{sub}}\,\mathbf{T}_{\text{bpl}}\,\mathbf{T}_{Y_2}\,\mathbf{T}_{\text{sub}}\,\mathbf{T}_{Y_3}. \tag{3.3}$$

Now with $\mathbf{T}_{\text{elem}}$, it is possible to relate the input field, admittances, and output fields of each metasuface subwavelength element as [43]

$$\begin{bmatrix} \vec{E}_t^- \\ \vec{H}_t^- \end{bmatrix} = \mathbf{T}_{\text{elem}} \begin{bmatrix} \vec{E}_t^+ \\ \vec{H}_t^+ \end{bmatrix}. \tag{3.4}$$

To model the metasurface in its entirety, $\mathbf{T}_{\text{elem}}$ must be defined for all the subwavelength elements. In this work, we assume that the dielectric layers (substrates and bondply) are spatially invariant. Therefore, to model the complete metasurface, Y_1, Y_2, and Y_3 for every metasurface element must be known. We also replace the left hand side of (3.4) with the incident field since we desire reflectionless metasurfaces. Finally, note that since Y_1 can be different than Y_3, the algorithm may yield an omega-type bianisotropic metasurface [94].

3.4.2 Field model

Now that it is possible to relate the input and output fields of each subwavelength element, the fields on the output boundary of the metasurface Σ^+ are available. Then, as in [2], we use the well-known electric field integral equations and the principle of duality [47] to obtain expressions relating the electric and magnetic current densities on Σ^+ to H_z on the ROI through the Green's function of free space. In the discrete domain, this transformation between currents on Σ^+ to H_z on the ROI can be represented as the following matrix operator

$$\underbrace{\mathbf{H_z}}_{\text{on ROI}} = \begin{bmatrix} \mathbf{A}_{\mathrm{H_z J_y}} & \mathbf{A}_{\mathrm{H_z M_z}} \end{bmatrix} \underbrace{\begin{bmatrix} \mathrm{J}_y \\ \mathrm{M}_z \end{bmatrix}}_{\text{on } \Sigma^+}, \tag{3.5}$$

where $\mathbf{H_z}$ is a vector containing all the H_z values on the ROI, $\mathbf{A}_{\mathrm{H_z J_y}}$ operates on the electric current density vector J_y on Σ^+ to produce the electric current contribution of H_z, and $\mathbf{A}_{\mathrm{H_z M_z}}$ operates on the magnetic current density vector M_z on Σ^+ to produce the magnetic current contribution of H_z.

In order to make use of (3.5), we must be able to calculate the electric and magnetic surface current densities from the output fields on Σ^+. In the case where Love's condition is enforced, we can relate these two quantities as

$$\begin{aligned} J_y &= \hat{n} \times \vec{H}_t^+ = -H_z\Big|_{\Sigma^+}, \\ M_z &= -\hat{n} \times \vec{E}_t^+ = -E_y\Big|_{\Sigma^+}, \end{aligned} \tag{3.6}$$

where $\hat{n}$ is the unit outward normal on the output side of the metasurface. The method and importance of enforcing Love's condition will be explained later on in this paper.

3.4.3 Complete forward model

The circuit and field models described above are now put together to demonstrate the complete relationship between the input field, admittances, and the field at the ROI. First, note that $\mathbf{T}_{\mathrm{elem}}$ of each metasurface element can be explicitly written in terms of its ABCD parameters, and its inverse can also be expressed as

$$\mathbf{T}_{\mathrm{elem}} = \begin{bmatrix} A & B \\ C & D \end{bmatrix} \implies \mathbf{T}_{\mathrm{elem}}^{-1} = \frac{1}{\Delta} \begin{bmatrix} D & -B \\ -C & A \end{bmatrix}, \tag{3.7}$$

where $\Delta = AD - BC$. Because in this problem the two-port network at each element is reciprocal, $\Delta = 1$. Once the individual ABCD parameters are found for each element from (3.3), by combining (3.4), (3.5), (3.6), and (3.7), the field at the ROI can be found

as

$$\mathbf{H_z} = \mathcal{G}(\mathbf{Y}) = \begin{bmatrix} \mathbf{A}_{\mathrm{H_z J_y}} & \mathbf{A}_{\mathrm{H_z M_z}} \end{bmatrix} \begin{bmatrix} \mathbf{C}(\mathbf{Y}) \odot \mathbf{E}_y^- - \mathbf{A}(\mathbf{Y}) \odot \mathbf{H}_z^- \\ -\mathbf{D}(\mathbf{Y}) \odot \mathbf{E}_y^- + \mathbf{B}(\mathbf{Y}) \odot \mathbf{H}_z^- \end{bmatrix}, \tag{3.8}$$

where $\odot$ denotes the Hadamard (element-wise) product of two vectors of the same size. Note that in (3.8) the ABCD parameters are now in boldface to represent a vector wherein each element of that vector corresponds to a parameter from a different metasurface subwavelength element on Σ^+. For example,

$$\mathbf{A}(\mathbf{Y}) = \begin{bmatrix} A_1 \\ A_2 \\ \vdots \\ A_N \end{bmatrix} \in \mathbb{C}^N, \quad \mathbf{H}_z^- = \begin{bmatrix} H_{z,1}^- \\ H_{z,2}^- \\ \vdots \\ H_{z,N}^- \end{bmatrix} \in \mathbb{C}^N, \tag{3.9}$$

where A_i is the A component of $\mathbf{T}_{\text{elem}}$ of the ith unit cell, $H_{z,i}^-$ is H_z^- at the ith unit cell, and N is the total number of unit cells. Furthermore, it is clear that the ABCD parameters are functions of the admittances of each element. We have written $\mathbf{A}(\mathbf{Y})$ as a way to make clear that the A parameter for every unit cell is a function of the admittances of that element. In addition, $\mathbf{Y}$ is composed of $\mathbf{Y}_1$, $\mathbf{Y}_2$, and $\mathbf{Y}_3$, which are the admittance profiles of each layer of the metasurface. Each element in these vectors correspond to the admittance from a specific metasurface unit cell. That is,

$$\mathbf{Y_i} = \begin{bmatrix} Y_{i,\ \text{elem\#1}} \\ Y_{i,\ \text{elem\#2}} \\ \vdots \\ Y_{i,\ \text{elem\#}N} \end{bmatrix}, \tag{3.10}$$

where $i = \{1, 2, 3\}$, and 'elem' refers to a subwavelength element (unit cell) of the metasurface.

3.5 Inverse Problem

The process of calculating an appropriate admittance profile to achieve a desired complex field or phaseless power pattern is now explained. To this end, a data misfit cost functional is defined, and a method of enforcing Love's condition and smoothing regularizers are described. Then, the gradient descent minimization process is presented.

3.5.1 Data Misfit Cost Functional

We form a cost functional that compares the modeled pattern due to a predicted metasurface admittance profile with the desired pattern. The modeled pattern due to a set of microwave admittances can be calculated using (3.8). The desired pattern is stored in the vector $\mathbf{f}_{\text{ROI}}$ for the field pattern synthesis and in the vector $|\mathbf{f}_{\text{ROI}}|^2$ for the power pattern synthesis. The data misfit cost functional will then be

$$\mathcal{C}_{\text{data}}(\mathbf{Y}) = \begin{cases} \zeta_f \left\| \mathcal{G}(\mathbf{Y}) - \mathbf{f}_{\text{ROI}} \right\|^2 & \text{field pattern synthesis} \\ \\ \zeta_p \left\| |\mathcal{G}(\mathbf{Y})|^2 - |\mathbf{f}_{\text{ROI}}|^2 \right\|^2 & \text{power pattern synthesis} \end{cases} \tag{3.11}$$

where $\|.\|$ denotes the L_2 norm over the ROI, $\mathbf{Y}$ represents the unknown admittance profile, and the normalization constants ζ_f and ζ_p are defined as $\|\mathbf{f}_{\text{ROI}}\|^{-2}$ and $\||\mathbf{f}_{\text{ROI}}|^2\|^{-2}$ respectively.

3.5.2 Passive Lossless Metasurfaces

To design passive and lossless metasurfaces, we assume that the admittances in each layer are purely imaginary. For every subwavelength element we assume

$$\mathbf{T}_{Y_i} = \begin{bmatrix} 1 & 0 \\ jY_i & 1 \end{bmatrix}, \tag{3.12}$$

where the Y_i's ($i = \{1, 2, 3\}$) are now purely real. (Note that j has been extracted out.) We then concatenate these real-valued numbers as in (3.10) to form three real-valued vectors, namely, $\mathbf{Y}_1,\ \mathbf{Y}_2,\ \mathbf{Y}_3 \in \mathbb{R}^N$. Therefore, the data misfit cost functional (3.11) is now a mapping from $\mathbb{R}^{3N}$ to $\mathbb{R}$.

3.5.3 Enforcing Love's Condition

Love's condition is a special case of the electromagnetic equivalence principle [98]. In our metasurface design problem, enforcing Love's condition along with minimizing the cost functional amounts to stipulating that the tangential electric and magnetic current densities J_y and M_z on the output metasurface boundary Σ^+ produce the desired magnetic field on the ROI and ideally produce zero field in the region behind Σ^+. Note that enforcing Love's condition allows the relations in (3.6) and subsequently (3.8) to be true. Herein, (similar to [2, 35]), Love's condition is enforced by virtue of restricting the magnetic field on an inward recessed surface to Σ^+ to be zero. This is done by mapping J_y and M_z on Σ^+ to the magnetic field on the virtual points (these virtual points are those that comprise the inward recessed surface to Σ^+) as well as to the ROI. Then we enforce that the magnetic field should be zero at these points by appending zeros to the desired field vector $\mathbf{f}$. Therefore, when Love's condition is being enforced, an unpacked view of

$\mathcal{G}(\mathbf{Y})$ is

$$\begin{aligned}\mathcal{G}(\mathbf{Y}) = \mathbf{H}_z(\mathbf{Y}) &= \begin{bmatrix}\mathbf{H}_z^{\mathrm{ROI}}(\mathbf{Y})\\ \mathbf{H}_z^{\mathrm{Love}}(\mathbf{Y})\end{bmatrix}\\ &= \begin{bmatrix}\begin{bmatrix}\mathbf{A}^{\mathrm{ROI}}_{\mathrm{H}_z\mathrm{J}_y}\\ \mathbf{A}^{\mathrm{Love}}_{\mathrm{H}_z\mathrm{J}_y}\end{bmatrix} & \begin{bmatrix}\mathbf{A}^{\mathrm{ROI}}_{\mathrm{H}_z\mathrm{M}_z}\\ \mathbf{A}^{\mathrm{Love}}_{\mathrm{H}_z\mathrm{M}_z}\end{bmatrix}\end{bmatrix} \begin{bmatrix}\mathbf{C}(\mathbf{Y})\odot\mathbf{E}^-_{\mathbf{y}} - \mathbf{A}(\mathbf{Y})\odot\mathbf{H}^-_{\mathbf{z}}\\ -\mathbf{D}(\mathbf{Y})\odot\mathbf{E}^-_{\mathbf{y}} + \mathbf{B}(\mathbf{Y})\odot\mathbf{H}^-_{\mathbf{z}}\end{bmatrix},\end{aligned} \tag{3.13}$$

where $\mathbf{H}_z^{\mathrm{Love}}$ is the magnetic field at Love's virtual points, $\mathbf{H}_z^{\mathrm{ROI}}$ is the magnetic field on the ROI, and $\mathbf{A}^{\mathrm{Love}}_{\mathrm{H}_z\mathrm{J}_y}$ and $\mathbf{A}^{\mathrm{Love}}_{\mathrm{H}_z\mathrm{M}_z}$ are operators that map J_y and M_z to the magnetic field at Love's virtual points, respectively. Similarly, $\mathbf{A}^{\mathrm{ROI}}_{\mathrm{H}_z\mathrm{J}_y}$ and $\mathbf{A}^{\mathrm{ROI}}_{\mathrm{H}_z\mathrm{M}_z}$ are operators that map J_y and M_z to the magnetic field on the ROI.

Similarly, the data vectors $\mathbf{f}_{\mathrm{ROI}}$ and $|\mathbf{f}_{\mathrm{ROI}}|^2$ in (3.11) will be changed to $\mathbf{f}$ and $|\mathbf{f}|^2$ respectively as

$$\mathbf{f} = \begin{bmatrix}\mathbf{f}_{\mathrm{ROI}}\\ \mathbf{f}_{\mathrm{Love}}\end{bmatrix},\ |\mathbf{f}|^2 = \begin{bmatrix}|\mathbf{f}_{\mathrm{ROI}}|^2\\ \mathbf{f}_{\mathrm{Love}}\end{bmatrix},\ \mathbf{f}_{\mathrm{Love}} = \begin{bmatrix}0\\ 0\\ \vdots\\ 0\end{bmatrix}, \tag{3.14}$$

where $\mathbf{f}_{\mathrm{Love}}$ is the part of $\mathbf{f}$ that enforces Love's condition. The length of $\mathbf{f}_{\mathrm{Love}}$ is equal to the number of virtual points on Love's surface. Finally, it is instructive to note that the augmentation of $\mathcal{G}(\mathbf{Y})$ by the Love's component makes the minimization of $\mathcal{C}_{\mathrm{data}}(\mathbf{Y})$ in (3.11) for the field and power pattern syntheses equivalent to minimizing

$$\zeta_f\{\left\|\mathbf{H}_z^{\mathrm{ROI}}(\mathbf{Y}) - \mathbf{f}_{\mathrm{ROI}}\right\|^2 + \left\|\mathbf{H}_z^{\mathrm{Love}}(\mathbf{Y})\right\|^2\}, \tag{3.15}$$

$$\zeta_p\{\left\||\mathbf{H}_z^{\mathrm{ROI}}(\mathbf{Y})|^2 - |\mathbf{f}_{\mathrm{ROI}}|^2\right\|^2 + \left\||\mathbf{H}_z^{\mathrm{Love}}(\mathbf{Y})|^2\right\|^2\}, \tag{3.16}$$

respectively.

3.5.4 Local Power Conservation (LPC)

Local power conservation [94] requires that the real power entering the unit cell in the normal direction be equal to the real power leaving the unit cell in the normal direction. As shown in [94], if LPC is satisfied between the incident field E_t^{inc} and H_t^{inc} and E_t^+ and H_t^+, we are able to transform the incident field to the output field using a reflectionless lossless passive omega-type bianisotropic metasurface. The proposed inversion algorithm inherently permits only those solutions that satisfy LPC. This can be easily verified by considering (3.4) and (3.7) and finding the real power density entering the metasurface (in the normal direction) as

$$\begin{aligned}\text{Re}\{E_t^- H_t^{-^*}\} = \text{Re}\{(AC^*|E_t^+|^2 + AD^* E_t^+ H_t^{+^*} \\ + BC^* H_t^+ E_t^{+^*} + BD^*|H_t^+|^2)\}.\end{aligned} \tag{3.17}$$

Since the admittances of the three layers are only allowed to be purely imaginary, and the dielectric substrates and bondply are assumed to be lossless, A and D are purely real and B and C are purely imaginary. In addition, since E_t^- and H_t^- are set to be the tangential incident fields (E_t^{inc} and H_t^{inc}) and noting the reciprocity of each unit cell, we can simplify (3.17) as

$$\begin{aligned}&\text{Re}\{E_t^{\text{inc}} H_t^{\text{inc}^*}\} = \text{Re}\{(ADE_t^+ H_t^{+^*} - B^* C^* H_t^+ E_t^{+^*})\} = \\ &\text{Re}\{(ADE_t^+ H_t^{+^*} - BCH_t^{+^*} E_t^+)\} = \text{Re}\{E_t^+ H_t^{+^*}\}.\end{aligned} \tag{3.18}$$

This shows that the LPC is satisfied. Note that the above analysis implicitly requires that E_t^+ and H_t^+ form a wavefront that propagates away from the metasurface in free space. That is why the data misfit cost functional has been augmented by the Love's constraint.

3.5.5 Favouring Smooth Equivalent Currents

If there is more spatial variation in the equivalent currents (i.e., less smooth currents), there will be more spatial variations in E_t^+ and H_t^+ when moving from one unit cell to the neighboring unit cell, which can be challenging to achieve in practice. To this end, we utilize a total variation (TV) regularizer to favour smoother equivalent currents by minimizing the norm of the derivative of the current along the metasurface (similar to [99]). The cost functionals used to smooth the electric current densities $\mathbf{J}$ and magnetic current densities $\mathbf{M}$ are respectively

$$\begin{aligned}
\mathcal{C}_{\mathrm{JTV}}(\mathbf{Y}_i) &= \tau_1 \sum_{i=1}^{3} \left\| \frac{\partial}{\partial y}(\mathbf{J}(\mathbf{Y}_i)) \right\|^2 \\
&= \tau_1 \sum_{i=1}^{3} \left\| \frac{\partial}{\partial y}(\mathbf{C}(\mathbf{Y}_i) \odot \mathbf{E}_y^- - \mathbf{A}(\mathbf{Y}_i) \odot \mathbf{H}_z^-) \right\|^2 \\
&= \tau_1 \sum_{i=1}^{3} \left\| \frac{\partial}{\partial y}(\mathbf{z_{i1}} \mathbf{Y}_i + \mathbf{h_{J_i}}) \right\|^2 ,
\end{aligned} \tag{3.19}$$

$$\begin{aligned}
\mathcal{C}_{\mathrm{MTV}}(\mathbf{Y}_i) &= \tau_2 \sum_{i=1}^{2} \left\| \frac{\partial}{\partial y}(\mathbf{M}(\mathbf{Y}_i)) \right\|^2 \\
&= \tau_2 \sum_{i=1}^{2} \left\| \frac{\partial}{\partial y}(-\mathbf{D}(\mathbf{Y}_i) \odot \mathbf{E}_y^- + \mathbf{B}(\mathbf{Y}_i) \odot \mathbf{H}_z^-) \right\|^2 \\
&= \tau_2 \sum_{i=1}^{2} \left\| \frac{\partial}{\partial y}(\mathbf{z_{i2}} \mathbf{Y}_i + \mathbf{h_{M_i}}) \right\|^2 ,
\end{aligned} \tag{3.20}$$

where $\frac{\partial}{\partial y}$ is the derivative operator along the y direction, and the above L_2 norms are taken along the metasurface. Also, note that in (3.19) $i = \{1, 2, 3\}$ and in (3.20), $i = \{1, 2\}$. (The reason that $i = \{1, 2\}$ for $\mathcal{C}_{\mathrm{MTV}}$ is that $\mathbf{M}$ is not a function of $\mathbf{Y}_3$; see (A.1) in Appendix A.1.) In addition, τ_1 and τ_2 are real weighting parameters and $\mathbf{h_{J_i}}$ and $\mathbf{h_{M_i}}$ are vectors of constants that are formed after $\mathbf{Y}_i$ has been factored from the currents $\mathbf{J}$ and $\mathbf{M}$, respectively. The expressions for $\mathbf{z}$ vectors are available in (A.9) in Appendix A.1.

3.5.6 Admittance Regularization

One of the inherent benefits of this method is the ability to enforce constraints or regularize the circuit parameters directly. Herein, to demonstrate the capability of admittance regularization, we have implemented an additive L_2 norm TV regularizer for the circuit parameters. Using this approach, we are trying to minimize rapid changes in the admittances along each layer from unit cell to unit cell. In addition to being an example of how we can regularize circuit parameters directly with this work, smoothing the admittances in each layer provides some practical benefits. Firstly, the utilized transmission line model is based on the local periodicity approximation [100], and thus, this regularization can reduce the discrepancy between the actual and modeled wave propagation. Secondly, when simulating the scattering parameters of individual unit cell structures, infinite periodicity is assumed. Later, when these elements combine to form the metasurface, this assumption no longer holds. Therefore, smoothing the admittances reduces the error introduced by the periodicity assumption during simulation. Furthermore, since the admittance layers are smoother, this may serve to limit the range of the lookup table required to implement the metasurface thereby saving time. To this end, since there are three admittance layers for each unit cell, each of these layers must be smoothed independently. Therefore, we form $\mathcal{C}_{\mathrm{YTV}}(\mathbf{Y})$ as

$$\mathcal{C}_{\mathrm{YTV}}(\mathbf{Y}) = \tau_3 \sum_{i=1}^{3} \left\| \frac{\partial}{\partial y}(\mathbf{Y}_i) \right\|^2, \tag{3.21}$$

where τ_3 is a real weighting coefficient and the above L_2 norm is taken along the metasurface.

3.5.7 Minimizing the Total Cost Functional

We now form the total cost functional as

$$\mathcal{C}(\mathbf{Y}) = \mathcal{C}_{\mathrm{data}}(\mathbf{Y}) + \mathcal{C}_{\mathrm{JTV}}(\mathbf{Y}) + \mathcal{C}_{\mathrm{MTV}}(\mathbf{Y}). \tag{3.22}$$

If the designer would like to apply some admittance regularization, e.g., via $\mathcal{C}_{\text{YTV}}(\mathbf{Y})$, that should also be added to the above cost functional. The total cost functional is then minimized over $\mathbf{Y}$; i.e.,

$$\mathbf{Y}^{\text{design}} = \arg\min_{\mathbf{Y}} \{\mathcal{C}(\mathbf{Y})\}, \tag{3.23}$$

where $\mathbf{Y}^{\text{design}}$ is the final designed admittance profile. Herein, we solve (3.23) by utilizing a gradient descent method. However, finding the gradient of $\mathcal{C}(\mathbf{Y})$ with respect to the complete set of circuit admittances is difficult. Therefore we solve (3.23) by minimizing the functional over each separate admittance layer.

At the kth iteration of the algorithm, the admittances of the ith layer ($i = \{1, 2, 3\}$) are updated as

$$\mathbf{Y}_i^{(k+1)} = \mathbf{Y}_i^{(k)} + \alpha_i^{(k)} \mathbf{g}_{\mathbf{Y}_i}^{(k)}, \tag{3.24}$$

where $\mathbf{Y}_i^{(k)} \in \mathbb{R}^N$ is the known admittance of the ith layer at the kth iteration[5], $\alpha_i^{(k)} \in \mathbb{R}$ is the step length, and $\mathbf{g}_{\mathbf{Y}_i}^{(k)} \in \mathbb{R}^N$ is the gradient direction at the kth iteration corresponding to minimization of $\mathcal{C}(\mathbf{Y})$ with respect to the ith admittance layer. Consequently, one full update of the admittance profile includes three sequential layer updates. To this end, the gradient of the functional (3.22) is needed with respect to each admittance layer $\mathbf{Y}_1$, $\mathbf{Y}_2$, and $\mathbf{Y}_3$, i.e., we need to calculate

$$\mathbf{g}_{\mathbf{Y}_i} = \mathbf{g}_{\mathbf{Y}_i}^{\text{data}} + \mathbf{g}_{\mathbf{Y}_i}^{\text{JTV}} + \mathbf{g}_{\mathbf{Y}_i}^{\text{MTV}}, \tag{3.25}$$

where $\mathbf{g}_{\mathbf{Y}_i}$ is the gradient of $\mathcal{C}(\mathbf{Y})$ with respect to the admittance layer $\mathbf{Y}_i$. Similarly, $\mathbf{g}_{\mathbf{Y}_i}^{\text{data}}$, $\mathbf{g}_{\mathbf{Y}_i}^{\text{JTV}}$ and $\mathbf{g}_{\mathbf{Y}_i}^{\text{MTV}}$ are the gradients of $\mathcal{C}_{\text{data}}$, $\mathcal{C}_{\text{JTV}}$, and $\mathcal{C}_{\text{MTV}}$ with respect to the admittance layer $\mathbf{Y}_i$, respectively.

[5]Note that the actual admittance is $j\mathbf{Y}_i^{(k)}$ and is purely imaginary; however, we have factored out j for formulation simplicity, thus, $\mathbf{Y}_i^{(k)}$ is purely real.

For the field pattern synthesis, the gradient of the data misfit cost functional will be

$$\mathbf{g}_{\mathbf{Y}_i}^{\text{data}} = 2\zeta_f \text{Re}\{\mathbf{L}_i^H(\mathcal{G}(\mathbf{Y}) - \mathbf{f})\}, \tag{3.26}$$

where Re is an operator that extracts the real part of the complex vector argument and the superscript H denotes the Hermitian (complex conjugate transpose) operator. Also, the expressions for the matrix operators $\mathbf{L}_1$, $\mathbf{L}_2$, and $\mathbf{L}_3$ can be found in (A.8) in Appendix A.1. On the other hand, for the power pattern synthesis problem, the gradient of the data misfit cost functional will be

$$\mathbf{g}_{\mathbf{Y}_i}^{\text{data}} = 4\zeta_p \text{Re}\left(\mathbf{L}_i^H(\mathcal{G}(\mathbf{Y}) \odot (|\mathcal{G}(\mathbf{Y})|^2 - |\mathbf{f}|^2))\right). \tag{3.27}$$

The derivation of these gradients can be found in Appendix A.1. In addition, the gradients for the current smoothing functional are

$$\mathbf{g}_{\mathbf{Y}_i}^{\text{JTV}} = -2\tau_1 \text{Re}\{\frac{\partial^2}{\partial y^2}(\mathbf{z_{i1}}\mathbf{Y}_i + \mathbf{h_{J_i}}) \odot \mathbf{z_{i1}^*}\},\ i = \{1, 2, 3\} \tag{3.28}$$

and

$$\mathbf{g}_{\mathbf{Y}_i}^{\text{MTV}} = -2\tau_2 \text{Re}\{\frac{\partial^2}{\partial y^2}(\mathbf{z_{i2}}\mathbf{Y}_i + \mathbf{h_{M_i}}) \odot \mathbf{z_{i1}^*}\},\ i = \{1, 2\} \tag{3.29}$$

where the expression for the $\mathbf{z}$ vectors can also be found in Appendix A.1. Furthermore, the gradients of the L_2 norm total variation smoothing functionals introduced in (3.21) are

$$\mathbf{g}_{\mathbf{Y}_i}^{\text{YTV}} = -2\tau_3 \frac{\partial^2}{\partial y^2}(\mathbf{Y}_i),\ i = \{1, 2, 3\} \tag{3.30}$$

where $\frac{\partial^2}{\partial y^2}$ is a second derivative operator along the y direction. Finally, the required step lengths are derived analytically and are discussed in Appendix A.2.

3.5.8 Scaling the Incident Field

In pattern synthesis, it is the relative angular distribution of the pattern—not the absolute pattern amplitude level—that is desired. However, the data vector $\mathbf{f}$ or $|\mathbf{f}|^2$ that is fed to the inversion algorithm has absolute values, and the inversion algorithm will naturally try to meet those absolute values to yield a solution. To handle this, we set our incident field as $\nu^{(k)}\vec{\Psi}^{\text{inc}}$ where $\nu^{(k)}$ is a coefficient to be determined at the kth iteration of the algorithm. (This has also been used in the context of inverse scattering for design [101].) The presence of this coefficient can be also loosely viewed as an attempt to satisfy the total power conservation between the desired pattern and the incident field level. To this end, we choose $\nu^{(k)}$ so as to minimize the data misfit cost functional, which results in

$$\nu^{(k)} = \begin{cases} \left\|\mathcal{G}(\mathbf{Y}^{(k)})\right\|^{-2} [\mathcal{G}(\mathbf{Y}^{(k)})]^H \mathbf{f}_{\text{ROI}} & \text{Field synth.} \\ \left\||\mathcal{G}(\mathbf{Y}^{(k)})|^2\right\|^{-2} [|\mathcal{G}(\mathbf{Y}^{(k)})|^2]^T |\mathbf{f}_{\text{ROI}}|^2 & \text{Power synth.} \end{cases} \tag{3.31}$$

Note that the other cost functionals such as $\mathcal{C}_{\text{JTV}}$ that use the incident field now need to use $\nu^{(k)}\vec{\Psi}^{\text{inc}}$.

3.5.9 Adaptive Control of the Love's Constraint Weight

As can be seen in (3.15) and (3.16), the relative weight of the Love's constraint with respect to the data misfit norm is one. From our numerical experience, we noticed that it is better to give more weight to the Love's constraint in earlier iterations of the inversion algorithm and then gradually decrease the relative weight back to one. Thus, at the kth iteration of the algorithm, we change (3.15) and (3.16) to

$$\zeta_f \{ \left\| \mathbf{H}_z^{\text{ROI}}(\mathbf{Y}) - \mathbf{f}_{\text{ROI}} \right\|^2 + \chi^{(k)} \left\| \mathbf{H}_z^{\text{Love}}(\mathbf{Y}) \right\|^2 \} \tag{3.32}$$

and

$$\zeta_p \{ \left\| |\mathbf{H}_z^{\text{ROI}}(\mathbf{Y})|^2 - |\mathbf{f}_{\text{ROI}}|^2 \right\|^2 + \chi^{(k)} \left\| |\mathbf{H}_z^{\text{Love}}(\mathbf{Y})|^2 \right\|^2 \}, \tag{3.33}$$

respectively where the weight $\chi^{(k)}$ is set to

$$\chi^{(k)} = \begin{cases} (1 + \left\|\mathbf{H}_z^{\text{Love}}(\mathbf{Y}^{(k)})\right\|^2)/\gamma_l & \text{Field synthesis} \\ (1 + \left\||\mathbf{H}_z^{\text{Love}}(\mathbf{Y}^{(k)})|^2\right\|^2)/\gamma_l & \text{Power synthesis} \end{cases} \tag{3.34}$$

where $\gamma_l \in \mathbb{R}$ is a constant to be explained below. As can be seen, if the Love's constraint is poorly satisfied, $\left\|\mathbf{H}_z^{\text{Love}}(\mathbf{Y}^{(k)})\right\|$ will be a large number, and therefore $\chi^{(k)}$ increases, thus, guiding the inversion algorithm to favour satisfying Love's condition. If Love's condition is perfectly satisfied, then $\mathbf{H}_z^{\text{Love}} = \mathbf{0}$, and thus $\chi^{(k)}$ will become one. This non-zero weight is necessary so that the inversion algorithm does not deviate from Love's condition while trying to minimize the data misfit cost functional. The constant γ_l is chosen so that the initial weight of $\chi^{(k)}$ is not too large. In the authors' experience, if γ_l is not used, the algorithm will initially only focus on enforcing Love's condition, leading to an unacceptable solution with a large data error. Furthermore, τ_1 and τ_2 in (3.19) and (3.20) at the kth iteration of the algorithm are set to $\gamma_{\text{TV}}\chi^{(k)} \times 10^{-10}$ and $\gamma_{\text{TV}}\chi^{(k)} \times 10^{-14}$ where $\gamma_{\text{TV}} \in \mathbb{R}$.[6] This is done to have more TV emphasis in early iterations to guide the inversion algorithm toward smoother equivalent currents. The constant γ_{TV} can be used to scale the TV emphasis as well. Note that the constants γ_l and γ_{TV} do not change in the minimization process.

3.5.10 Initialization and Truncation of the Algorithm

In this work, the initial guess for the gradient descent algorithm is a vector of zeros, i.e. all the admittances for every unit cell are initially assumed to be zero. This means that we initially assume that only the dielectric layers (two substrate and one bondply layers) exist in the circuit model. It may be possible to use more sophisticated initial guesses in future work. In addition, the gradient-based admittance reconstruction algorithm is

[6]The choice of 10^{-10} and 10^{-14} has been done in an ad-hoc manner through numerical trials. If these are chosen to be much higher the algorithm can not properly minimize the data-misfit cost functional (over-regularization). On the other hand if they are chosen to be too low, the smoothness will be compromised (under-regularization).

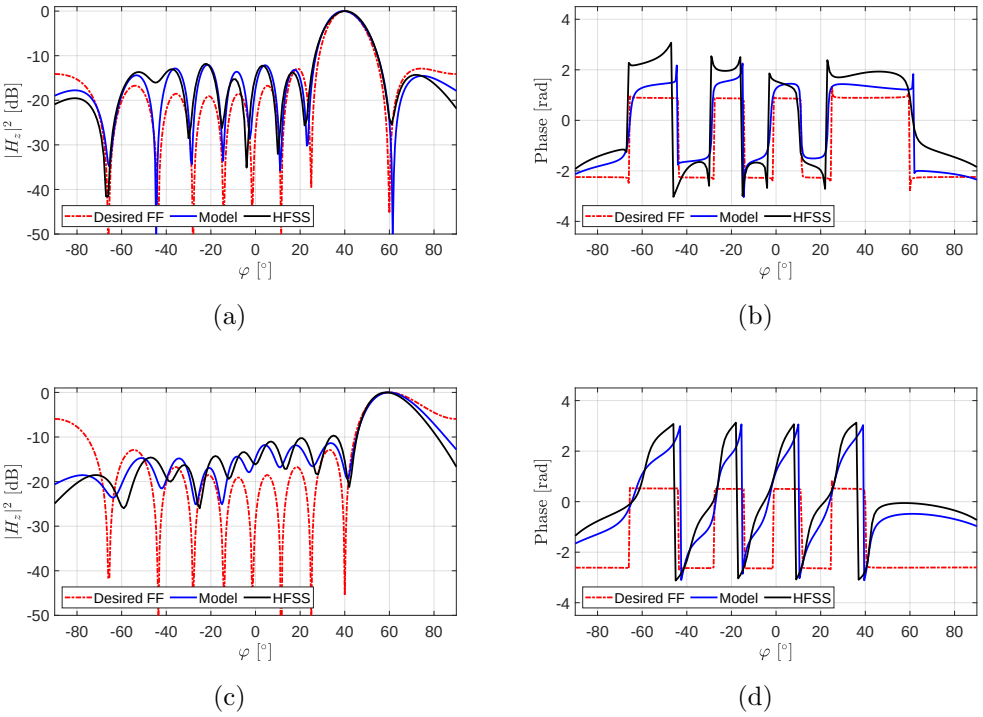

Figure 3.5: Field (amplitude and phase) pattern synthesis examples. The power (left column) and the associated phase (right column) patterns from $\varphi = -90°$ to $90°$ (at $\theta = 90°$ plane) are shown for two metasurface design problems. The desired field patterns are shown in red-dashed curve. The first example (top row) has a main beam at $\varphi = 40°$ whereas the second example (bottom row) has a main beam at $\varphi = 60°$. The required admittance profile is reconstructed by the inversion algorithm with the parameter values of $(\gamma_{\mathrm{TV}}, \gamma_l)$ set to $(1, 8)$ and $(1.2, 8)$ for the first and second examples respectively. The predicted field pattern from the resulting metasurface is calculated using two different methods: the forward model (blue), and ANSYS HFSS simulation (black).

iterative in nature and therefore requires a stopping criterion. In the current version of this work we truncate the algorithm in an ad-hoc manner, although this can be changed in the future.

3.6 Results and Discussion

Herein, the gradient-based admittance reconstruction algorithm is used to solve two-dimensional metasurface design problems. To this end, the capability of the inversion

algorithm to design metasurfaces that produce desired field pattern (amplitude and phase) as well as power (phaseless) patterns is demonstrated.

3.6.1 Problem Setup

The incident field $\vec{\Psi}^{\text{inc}}$ is chosen to be a plane wave normally incident upon the metasurface.[7] The metasurface's center is placed at the origin and the surface runs along the $\hat{y}$ direction while the plane wave propagates in the $\hat{x}$ direction; see Figure 3.1. The plane wave is assumed to be transverse-electric to the $\hat{z}$ direction allowing the E_y, E_x, and H_z field components. The desired field or power patterns (represented by H_z or $|H_z|^2$ respectively) on the ROI were created from arrays of nine Hertzian dipoles located along the $\hat{y}$-direction with a spacing of 0.5λ. The phases of the dipoles were varied to obtain the different beam directions in the far-field zone. All tests were performed at a frequency of 10.5 GHz.

The metasurface is made up of 30 subwavelength elements, each with a width of $\lambda/6$ (total length of 5λ or 0.1428 m). Consequently, for each example there are total of 90 unknowns: 30 unknowns for each of the top ($\mathbf{Y}_1$), middle ($\mathbf{Y}_2$), and bottom ($\mathbf{Y}_3$) admittance layers. We assumed the use of a Rogers RO3010 substrate (thickness of 1.28×10^{-3} m) and Rogers RO2929 bondply (thickness of 76×10^{-6} m) layers in the circuit model part of the forward solver. We assumed lossless dielectrics in the forward model for simplicity, but included realistic loss when verifying with a full-wave solver[8]. For all of the following examples, we make use of 180 virtual Love's points; i.e., $\mathbf{f}_{\text{Love}} \in \mathbb{R}^{180}$.

The ROI is on the output side of the metasurface in the far-field and is a set of points on a semicircle: the ROI's distance from the origin is 500λ, and the points are located on the plane where $\theta = 90°$ and $-90° \leq \varphi \leq 90°$. Finally, for each problem the gradient-based

[7] Absorbers are used on either side of the metasurface in order to isolate the fields on the input and output sides. Thus, the actual incident field is a plane wave in the presence of the absorbers measured at the reconstruction points.

[8] These dielectric substrate layers are low loss and thin compared to wavelength, so assuming no loss in the forward model is reasonable.

solver was run for a total of 3×10^4 iterations using MATLAB on a 16 core Windows machine with a 2.10 GHz processor and 128 GB of RAM. Full-wave verification was done with ANSYS HFSS using the same computer. We now present our results under two categories: field and power pattern syntheses.

3.6.2 Field Pattern Synthesis Examples

The inversion algorithm is first used to reconstruct the admittance profiles of metasurfaces capable of transforming an incident plane wave to two different desired field (amplitude and phase) patterns. The first desired field pattern is shown in Figure 3.5(a)-(b) with a red dashed curve. Note that the amplitude part of the desired field pattern has been shown in the form of amplitude-squared (power) pattern. As can be seen, the main beam of the desired pattern is directed toward $\varphi = 40°$. This desired field pattern is then given to the inversion algorithm in the form of the complex-valued data vector $\mathbf{f}_{\text{ROI}}$. The inversion algorithm will then reconstruct an admittance profile to support this transformation. The blue curve in Figure 3.5(a)-(b) shows the predicted pattern calculated by the forward model shown in (3.8) upon the convergence of the inversion algorithm. The black curve in Figure 3.5(a)-(b) shows the obtained pattern by modeling the designed metasurface in ANSYS HFSS[9], extracting the fields on the output side of the metasurface from the HFSS simulation, and then forward propagating those fields to the far-field zone by constructing an equivalent problem and using Green's function. It can be seen from Figure 3.5(a)-(b) that the obtained pattern (black) shows higher side lobes as compared to the side lobes in the desired pattern (dashed red). However, the obtained pattern is close to the desired pattern around the main beam area.

[9]The HFSS model treats the admittance profile via the impedance boundary conditions similar to [91]. That is, these admittances have not been implemented using copper traces such as dogbones. In addition, similar to [85], metallic (perfect electric conductor) baffles are placed between the neighbouring unit cells. In our full-wave simulation, we also used volumetric objects to simulate the dielectric bondply and substrate layers. These materials included realistic loss. We used absorbers (4λ) on either side of the metasurface to better isolate the input and output fields, while also providing separation from the periodic boundary condition (the excitation was done using floquet ports). Only propagating modes were taken into account. The tangential fields on the output side of the metasurface were recorded at a distance of $\approx \lambda/10$ (from Y_3). These tangential fields were then used to find the far-field pattern.

Table 3.1: Transmission Efficiency of Simulated Examples.

Example	η_{TX} [%]
First Field Pattern Synthesis (amplitude and phase)	90.2
Second Field Pattern Synthesis (amplitude and phase)	91.3
Power Pattern Synthesis (phaseless)	87.5
Power Pattern Synthesis with Admittance Regularization	88.3

The transmission efficiency is defined as

$$\eta_{\mathrm{TX}}[\%] = 100 \times \frac{P_{\mathrm{out}}}{P_{\mathrm{in}}}, \tag{3.35}$$

where P_{out} and P_{in} are the power out (i.e., on Σ^{+}) and the power incident on the metasurface, respectively. For this field pattern synthesis example, the achieved transmission efficiency is 90.2% as shown in Table 3.1. To visualize this relatively high efficiency, the real part (absolute value) of the total electric field in the simulation domain is shown in Figure 3.6, which shows small reflections on the input side of the metasurface (i.e., $x < 0$ region).

The second example is still a field pattern synthesis case whose desired amplitude and phase patterns are shown in Figure 3.5(c)-(d) as the dashed red curves. As can be seen, the main beam of the desired pattern is along $\varphi = 60°$. Upon the convergence of the inversion algorithm, the obtained field pattern of the designed metasurface (black curve) has a main beam along the intended direction but generally shows higher side lobes as compared to the desired pattern. In addition, the amplitude and phase are not matched as closely as the first field synthesis example. The main difference in the design process of these two examples was that the TV parameter weights τ_1 and τ_2 were chosen to be greater for the second example. This was done by scaling γ_{TV} from 1.0 for the first example to 1.2 in the second example. (See Section 3.5.9 for the description of γ_{TV}.) This greater emphasis enabled the authors to achieve a transmission efficiency of 91.3% as shown in Table 3.1, whereas if $\gamma_{\mathrm{TV}} = 1.0$ the efficiency decreased below 90%.

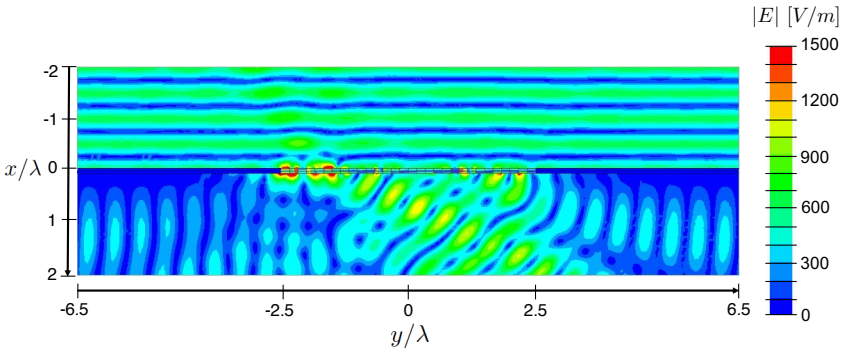

Figure 3.6: Absolute value of the real part of the total electric field in the simulation domain for the first field pattern synthesis example. The metasurface extends along $x = 0$ from $y = -2.5\lambda$ to $y = 2.5\lambda$. Along $x = 0$ and for $|y| > 2.5\lambda$, absorbing metasurfaces were placed. The left and right sides of the simulation domain consist of periodic boundaries. The top and bottom sides of the simulation domain are Floquet ports.

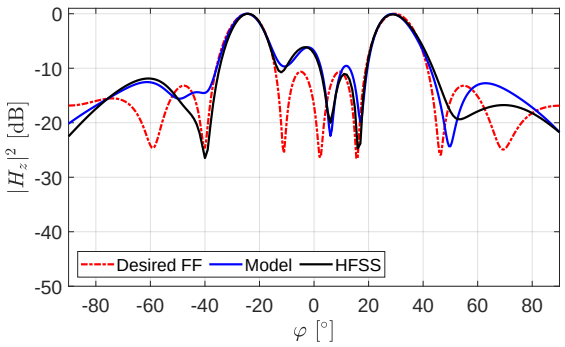

Figure 3.7: Power (phaseless) pattern synthesis example. The power pattern from $\varphi = -90°$ to $90°$ (at $\theta = 90°$ plane) is shown. The desired power pattern (dashed red) has main beams at $\varphi = 30°$ and $\varphi = -25°$. The required admittance profile is reconstructed by the inversion algorithm with parameter values of $\gamma_{\mathrm{TV}} = 1.0$ and $\gamma_l = 7$. The predicted power pattern from the resulting metasurface is calculated using two different methods: the forward model (blue), and ANSYS HFSS simulation (black).

3.6.3 Power Pattern Synthesis Examples

Next, the inversion algorithm is used to synthesize a desired power pattern. The ability to synthesize power patterns is advantageous in cases where there is no required phase constraint. Let us consider the desired power pattern shown in dashed red curve in Figure 3.7. As can be seen, this power pattern consists of two main beams at $\varphi = 30°$

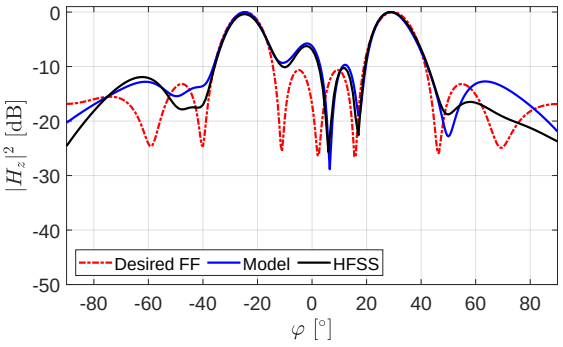

Figure 3.8: Power (phaseless) pattern synthesis example with admittance regularization. The desired power pattern is the same as that shown in Figure 3.7. The required admittance profile is reconstructed by the inversion algorithm with parameter values of $\gamma_{\text{TV}} = 1.0$ and $\gamma_l = 7$ in conjunction with an admittance regularization of $\tau_3 = 5 \times 10^{-6}$. The predicted power pattern from the resulting metasurface is calculated using two different methods: the forward model (blue), and ANSYS HFSS simulation (black).

and $\varphi = -20°$. This desired power pattern is provided to the inversion algorithm in the form of the real-valued data vector $|\mathbf{f}_{\text{ROI}}|^2$. Similar to the field pattern synthesis examples, when the inversion algorithm converges, we have a reconstructed admittance profile. The power pattern associated with the designed metasurface calculated by the forward model is shown in Figure 3.7 in blue. In addition, the power pattern calculated from HFSS data are shown in black. As can be seen in Figure 3.7, the designed metasurface produces a power pattern that follows the desired pattern; the two main beams are in the correct locations. However, there is an unwanted side lobe at about -6 dB which is not present in the desired pattern. Better solutions may be achievable through parameter tuning or by choosing a more sophisticated initial guess[10]. The achieved transmission efficiency for this example is 87.5% as listed in Table 3.1.

Next, the ability of this method to regularize the admittance profile directly is shown. The same desired power pattern is given to the inversion algorithm, but this time TV regularization is applied to each admittance layer as described in Section 3.5.6 with a weight of $\tau_3 = 5 \times 10^{-6}$. The resulting power pattern from the new metasurface are

[10]Additional degrees of freedom may also be required for some transformations as enforcing LPC restricts changes to the power distribution profile [99, 102].

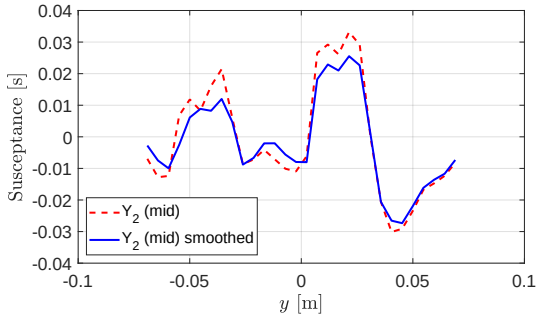

Figure 3.9: A graph comparing the admittances in the middle layer of the metasurfaces designed for the power pattern synthesis example. The blue and dashed red curves represent the reconstructed admittances in the presence and absence of admittance regularization respectively.

shown in Figure 3.8. As can be seen the power pattern produced by this metasurface is similar to the previous example shown in Figure 3.7, however the admittance profiles are different. This is most easily seen if one compares the middle admittance layers for the two metasurfaces. This comparison is shown in Figure 3.9 where the smoother admittance profile belongs to the metasurface where TV was applied to each admittance layer. We may change τ_3 to achieve an even smoother profile, and other types of regularization may also be added in the future. Finally, the achieved transmission efficiency of this power pattern synthesis example under admittance regularization was slightly increased to 88.3% as noted in Table 3.1.

3.7 Conclusion

A gradient-based inversion algorithm was introduced for metasurface design that process the desired field or power patterns and then reconstructs an appropriate metasurface admittance profile. The unique aspect of this inversion algorithm lies in its ability to directly reconstruct the three-layer admittance profile of the metasurface from the knowledge of the desired pattern specifications. To this end, the gradient operators and step lengths of the inversion algorithm were analytically derived for both field and power pattern syntheses. The inversion algorithm was tested for the design of metasurfaces that

transform an incident plane wave into desired field and power patterns. In addition, L_2 norm total variation additive regularizers were introduced to the optimization process to smoothen field variations over the metasurface boundary. Full-wave simulations were used to evaluate the method's ability to meet far-field magnitude-and-phase as well as phaseless constraints. In general, the obtained patterns around the main beam(s) were quite similar to the desired patterns; however, the inversion algorithm were not able to completely satisfy the side lobes and null constraints. This may be fixed by increasing the degrees of freedom in design, e.g., through the use of a metasurface pair. The main advantage of the proposed inverse design approach is the possibility of applying constraints (regularization) to the unknown admittance profile of the metasurface during the optimization procedure. To this end, we have demonstrated admittance smoothing functionality. More advanced admittance regularization, such as constraining the upper and lower ranges of admittance values, can be considered in a future work.

Chapter 4

Phaseless Gauss-Newton Inversion for Microwave Imaging

Preface

In the previous chapter we focused on designing metasurfaces, which are electrically thin devices. To characterize and design radiators with a larger electrical cross section we move to developing electromagnetic inverse scattering algorithms using the data and domain equations as described in Section 2.3.1. Note that this is an inverse scattering method as we are directly solving for the material properties in a region of interest. Because we are using the data and domain equations, we are inherently making use of the volume equivalence principle in this method, although the contrast sources are not used directly.

In this chapter, we present novel phaseless Gauss-Newton inversion (GNI) algorithms for microwave imaging applications (this is a characterization method). From the standpoint of the common EI methodology outlined in Section 1.4.4, the phaseless electric field data (electromagnetic data) is utilized to reconstruct the property of interest, which is the

complex relative permittivity of a region of interest[1]. The physical model is constructed using Maxwell's equations in the form of the data and domain equations. A data misfit cost functional is then constructed to compare the measured phaseless total electric field data to the simulated phaseless total electric field data. This is minimized using a Gauss-Newton inversion scheme wherein analytic gradient information is utilized. It is shown in the results that regularization is important to supplement the missing phase information in the desired data.

At the time of publishing, to the best of our knowledge this was the first time that a phaseless multiplicatively-regularized Gauss-Newton inversion imaging algorithm had been developed. In addition we have considered the use of prior information in conjunction with phaseless inversion. The EI framework was utilized to be able to make use of phaseless electric field data with a GNI algorithm, instead of complex measured data. The material presented in this chapter is based on the paper published in IEEE Transactions on Antennas and Propagation in September 2020 [41].[2]

Abstract

A phaseless Gauss-Newton inversion (GNI) algorithm is developed for microwave imaging applications. In contrast to full-data microwave imaging inversion that uses complex (magnitude and phase) scattered field data, the proposed phaseless GNI algorithm inverts phaseless (magnitude-only) total field data. This phaseless Gauss-Newton inversion (PGNI) algorithm is augmented with three different forms of regularization, originally developed for complex GNI. First, we use the standard weighted L_2 norm total variation multiplicative regularizer which is appropriate when there is no prior information about the object being imaged. We then use two other forms of regularization operators to

[1]The algorithm actually calculates the contrast of the region of interest, which is directly related to the relative permittivity (see Section 4.2).

incorporate prior information about the object being imaged into the PGNI algorithm. The first one, herein referred to as SL-PGNI, incorporates prior information about the expected relative complex permittivity values of the object of interest. The other, referred to as SP-PGNI, incorporates spatial priors (structural information) about the objects being imaged. The use of prior information aims to compensate for the lack of total field phase data. The PGNI, SL-PGNI, and SP-PGNI inversion algorithms are then tested against synthetic and experimental phaseless total field data.

4.1 Introduction

Electromagnetic inverse scattering algorithms are used in the microwave imaging (MWI) modality to calculate a quantitative image of the complex dielectric (permittivity) profile in a region of interest (ROI). The ROI, which is commonly referred to as the imaging/investigation domain, contains unknown objects that can often be characterized by analyzing these dielectric reconstructions.

In a microwave imaging system, transmitting antennas successively interrogate the ROI with incident microwave radiation and the resulting total electric (and/or magnetic) fields are measured by receiving antennas on a measurement domain S *outside* the ROI. Inverse scattering algorithms then process the measured data, as well as the known incident field data on S to reconstruct the complex dielectric profile in the ROI. Therefore, these algorithms inherently enable a non-destructive and non-ionizing imaging modality that can be used in many applications such as biomedical imaging, non-destructive evaluation, and remote-sensing [23, 74–76].

4.1.1 Full Data (Complex) Inversion

Typically, inverse scattering algorithms use the magnitude *and* phase (i.e. complex data) of the measured total and incident electric fields to reconstruct the complex permittivity profile within the ROI. (The total and incident fields refer to the measured fields in the presence and absence of the objects being imaged, respectively.) The availability of these complex data enable the calculation of the scattered field data, defined as the difference between the total and incident fields on S. The scattered field data facilitate the imaging process; these data can be thought of as being generated solely by the objects being imaged based on the electromagnetic volume equivalence principle. Therefore, the (complex) scattered field data are processed (inverted) to reconstruct the unknown complex permittivity profile in the ROI. The availability of the scattered field data also enable the use of the so-called scattered field calibration technique [103], which has shown promise to calibrate raw microwave imaging data. Several inverse scattering algorithms (or, simply, inversion algorithms) have been proposed to invert complex scattered field data [30, 78, 79, 104–107]. Some of these inversion algorithms utilize multiplicative regularization, e.g., the multiplicatively-regularized contrast source inversion (MR-CSI) [30] and multiplicatively-regularized Gauss-Newton inversion (MR-GNI) [78, 79] algorithms. Due to the use of the multiplicative regularization scheme, these algorithms offer automated adaptive regularization [31, 108]. Furthermore, in conjunction with the scattered field data, these algorithms have also been modified to take into account prior information regarding the ROI. For example, the multiplicative regularization schemes of these two methods have been modified to incorporate prior information about the expected complex permittivity values within the ROI [32, 40].

4.1.2 Phaseless Data Inversion - Overview

Although these state-of-the-art full data inverse scattering algorithms show promise with many applications, their requirement of using both magnitude and phase data can be

limiting in some ways. For example, measuring phase information is generally challenging at high frequencies and typically requires expensive equipment, e.g., vector network analyzers, as compared to magnitude-only measurements using affordable power meters. The affordability is, in particular, important depending on the specific imaging application. For example, it may not be reasonable for microwave biomedical imaging to be phaseless due to its required high sensitivity and specificity, however, for some industrial non-destructive testing applications the achievable accuracy from an affordable phaseless microwave imaging system can be sufficient and may be desirable. The use of phaseless data has also been considered in another area that is closely related to microwave imaging: near-field antenna measurements and diagnostics. Near-field antenna measurements generally require both magnitude and phase data for near-field to far-field transformation. However, phaseless near-field antenna measurement techniques can be helpful when phase data is not accurate or when near-field measurement system cost must be reduced. In particular, in planar near-field antenna measurements when relatively high probe positioning errors are present, it has been shown that a phaseless approach can outperform the full data (magnitude and phase) approach [109]. This is generally due to the fact that the measured phase data are more sensitive to probe positioning errors as compared to measured magnitude data [109]. For these reasons, phaseless (also known as magnitude-only, amplitude-only or intensity-only) approaches to inverse source and inverse scattering algorithms have been considered. In particular, many phaseless inverse scattering algorithms, such as phaseless MR-CSI [110, 111] have been reported in previous years [112–123].

4.1.3 Phaseless Data Inversion - Strategies

Broadly speaking, two main strategies are used in phaseless data inverse scattering algorithms [118]. The first strategy is a two-step process where the first step retrieves the phase data from measured magnitude-only data, and then standard full data (complex) inverse scattering algorithms invert the retrieved complex scattered field data in the second

step [117, 120]. This phaseless strategy in microwave imaging is similar to the iterative Fourier technique [124] in phaseless planar near-field antenna measurements in which the phase data on measurement planes are directly retrieved from two sets of magnitude-only data based on the correlation between the magnitude of the data on two different measurement planes via the iterative use of the plane wave spectrum. The second strategy (the focus of this paper) is a one-step process where the phaseless data are directly inverted to reconstruct the complex permittivity profile of the ROI [110, 112, 114]. This phaseless approach in microwave imaging is similar to the phaseless source reconstruction method in near-field antenna measurements where the phaseless data are directly inverted to reconstruct the equivalent currents of the antenna under test [24]. Herein, we provide a method that falls under the second strategy.

From an information point of view, it is clear that when the phase data are not available, we ideally need to provide the inversion algorithm with some extra information. For example, in phaseless planar near-field antenna measurements, the magnitude data are collected on two measurement planes as opposed to one measurement plane for the case of complex (magnitude and phase) near-field antenna measurements [24, 124]. Although having two planes of measured phaseless data is practical in antenna measurements due to the use of a mechanically scanning probe, this approach is not practical in typical microwave imaging systems because microwave imaging systems typically use co-resident stationary antenna elements [105, 125] to accelerate data collection in order to minimize image artefacts that may be caused from the potential movement of the objects being imaged. In addition, the use of a second measurement domain in phaseless microwave imaging, such as two rings of co-resident antennas, can result in blockage effects. Recently, the use of specialized probes to recover the phase from magnitude-only data has been proposed and experimentally tested with cylindrical dielectric targets [126, 127]. However, it is still worthwhile in phaseless microwave imaging, to investigate other methods to inject information into the inversion algorithm to compensate for the lack of phase data, without having to alter the hardware of existing microwave imaging systems.

In this paper, we first present a phaseless GNI algorithm (there is no explicit phase retrieval step). The phaseless GNI algorithm is then augmented with different forms of multiplicative regularization techniques in order to handle the inherent ill-posedness of the problem and to add prior information to make up for the lack of phase information. To the best of the authors' knowledge, this is the first time that a multiplicatively-regularized phaseless GNI algorithm has been developed. As will be seen, the presented phaseless GNI algorithm starts from a trivial initial guess (relative permittivity of the background) for the ROI, as opposed to a more sophisticated initial guess[3].

The first regularization scheme used herein is weighted L_2 norm total variation multiplicative regularization. When the basic phaseless GNI algorithm is augmented with this regularization scheme, we refer to it as PGNI ('p'haseless GNI). We emphasize that PGNI uses the same regularization technique as the phaseless MR-CSI algorithm in [110]. Then, we incorporate prior information into the PGNI algorithm to compensate for the lack of the phase data. First, the PGNI algorithm is augmented with another multiplicative regularizer that incorporates prior information about the expected complex permittivity values (shape and location regularization) in the ROI. We refer the resulting algorithm as SL-PGNI. Finally the PGNI is also augmented with a multiplicative regularizer that takes into account prior structural (spatial prior regularization) information in the ROI. Herein, this algorithm is referred to as SP-PGNI. These regularization methods, originally developed for full data (complex) inversion, are explained in more detail in later sections.

We start by briefly reviewing the full data (complex) MR-GNI algorithm in Section 4.2 for the sake of completeness. Then, in Section 4.3, the phaseless GNI formulation is developed, along with an overview of the different forms of regularization schemes used to augment this phaseless GNI algorithm. Section 4.4 will explain how the raw experimental data are calibrated prior to the inversion process and Section 4.4.3 will explain

[3]In contrast to the GNI algorithm, the standard initial guess for CSI relies on the back propagation technique which requires the phase of the data. Therefore, CSI's initial guess is not directly applicable to the phaseless implementation. In [110], an *ad hoc* procedure based on numerical simulations has been suggested to adapt this initial guess to the phaseless case. In particular, in [110], an *ad hoc* phase has been assumed for the total field data. Based on this assumption, the scattered data are formed and used for back propagation.

the limitation of our phaseless GNI implementation. Next in Section 4.5, reconstruction results obtained from the inversion of synthetic and experimental data sets are shown and discussed. Finally, the conclusions of this paper are presented in Section 4.6. A time-dependency of $\exp(j\omega t)$ is considered in this paper along with a 2D scalar configuration for the imaging setup where the electric field is assumed to be perpendicular to the cross section being imaged.

4.2 GNI – A Review

First, we formally define some terms and then briefly review the standard Gauss-Newton inversion (GNI) algorithm that utilizes full (complex) field data (i.e., magnitude and phase information). Let us denote the incident and total fields by E^{inc} and E respectively.[4] The difference between the total and incident fields, i.e., the scattered field, is then denoted by E^{scat}. For full data (FD), the inverse scattering problem may then be defined as the minimization of the following data misfit cost functional

$$\mathcal{C}^{\text{FD}}(\chi) = \eta \left\| F - E^{\text{scat}}(\chi) \right\|^2 \tag{4.1}$$

over χ where $\|\cdot\|$ is the L_2 norm taken over the measurement domain S. In addition, F is a complex vector that stores the measured scattered field data on S, and the normalization factor η is set to $\|F\|^{-2}$. Moreover, $E^{\text{scat}}(\chi)$ represents the *simulated* scattered field due to a predicted relative complex permittivity contrast χ. The contrast $\chi(\mathbf{r})$ in the ROI (the unknown we seek) is defined as

$$\chi(\mathbf{r}) \triangleq \frac{\epsilon(\mathbf{r}) - \epsilon_b}{\epsilon_b} \tag{4.2}$$

where $\epsilon(\mathbf{r})$ and is the relative complex permittivity at position $\mathbf{r}$ within the ROI. In addition, ϵ_b is the relative complex permittivity of the background medium. When the

[4] Due to the TM_z assumption the electric field vector in the formulation reduces to the $\hat{z}$-component.

GNI algorithm is applied to minimize (4.1), the contrast at the n^{th} iteration is updated as $\chi_{n+1} = \chi_n + \nu_n \Delta\chi_n$ where ν_n is the step length (calculated as in [128, Section 9]), and $\Delta\chi_n$ is the correction found by solving

$$[\mathbf{J}_n^H \mathbf{J}_n]\Delta\chi_n = -\mathbf{J}_n^H d_n. \tag{4.3}$$

In the above equation, $\mathbf{J}_n$ denotes the Jacobian (sensitivity) matrix that represents the derivative of the scattered field data on S with respect to the contrast χ. The subscript n of $\mathbf{J}_n$ indicates that this derivative is evaluated at $\chi = \chi_n$ and the superscript 'H' denotes the Hermitian (complex conjugate transpose) operator. Furthermore, d_n represents the complex discrepancy vector at the n^{th} iteration; i.e., $d_n = E^{\text{scat}}(\chi_n) - F$. Due to the ill-posedness of the inverse scattering problem, (4.1) needs to be augmented with a regularization term. For example, at the n^{th} iteration of the GNI algorithm, $\mathcal{C}^{\text{FD}}(\chi)$ may be multiplicatively regularized as $\mathcal{C}_n^{\text{reg}}(\chi) = \mathcal{C}^{\text{FD}}(\chi)\mathcal{C}_n^{\text{MR}}(\chi)$ where $\mathcal{C}_n^{\text{MR}}$ is the weighted L_2 norm total variation multiplicative regularizer (MR) given as [4, 78, 79]

$$\mathcal{C}_n^{\text{MR}}(\chi) = \frac{1}{A}\int_{\text{ROI}} \frac{|\nabla\chi(\mathbf{r})|^2 + \delta_n^2}{|\nabla\chi_n(\mathbf{r})|^2 + \delta_n^2} d\mathbf{s}. \tag{4.4}$$

In the above equation, A denotes the area of the ROI, and δ_n^2 is the steering parameter set to $\mathcal{C}^{\text{FD}}(\chi_n)/(\Delta x \Delta y)$ where $\Delta x \Delta y$ is the area of a single rectangular cell within the discretized ROI; the integration is performed over the area of the ROI. Applying the GNI algorithm to the multiplicatively-regularized cost functional $\mathcal{C}_n^{\text{reg}}$, (4.3) will change to the following regularized form

$$[\mathbf{J}_n^H \mathbf{J}_n + \beta_n \mathcal{L}_n]\Delta\chi_n = -\mathbf{J}_n^H d_n - \beta_n \mathcal{L}_n \chi_n \tag{4.5}$$

where $\mathcal{L}_n$ is the regularization operator. This operator, when operated on a vector of appropriate size, say x, is defined as

$$\mathcal{L}_n x = -\frac{1}{A}\nabla \cdot \left(\frac{1}{|\nabla\chi_n(\mathbf{r})|^2 + \delta_n^2}\nabla x\right). \tag{4.6}$$

In the above expression, '$\nabla\cdot$' and '∇' denote the divergence and gradient operators, respectively. Finally, the weight of this operator in (4.5), i.e., β_n, is $\mathcal{C}^{\mathrm{FD}}(\chi_n)/\eta$. Herein, we refer to this algorithm as the **MR-GNI** algorithm. We emphasize that the abbreviation MR-GNI, when used in this paper, implies the use of full (complex) data. This completes our review of the MR-GNI algorithm which was mainly based on [4, 78, 79]. It is instructive to note that the right hand side of (4.5) consists of two components. The first one represents the (negative) gradient of the data misfit cost functional $\mathcal{C}^{\mathrm{FD}}(\chi)$, thus, helping the algorithm extract the information within F to reconstruct χ. The second term represents the (negative) gradient of the regularization term $\mathcal{C}_n^{\mathrm{MR}}$ which helps the algorithm stabilize the inversion process and apply some edge-preserving operations. The relative weight of these two gradients are controlled by β_n which comes directly from the multiplicative nature of the regularized cost functional $\mathcal{C}^{\mathrm{reg}}$. Finally, the left hand side of (4.5) represents the operation of the Hessian matrix[5] on $\Delta\chi_n$. As expected, the Hessian consists of two parts as well: one for the data misfit cost functional, and the other for the regularization term.

4.3 Phaseless GNI

4.3.1 Phaseless Data Misfit Cost Functional

Herein, we begin to discuss the phaseless GNI algorithm. The lack of phase information prevents the scattered field data from being calculated. Therefore, the data to be inverted for the phaseless GNI algorithm will be the *magnitude* of the *total* field data. Herein the *magnitude* of the total field data is stored in the vector M. We then form the phaseless

[5]In the GNI algorithm, the Hessian matrix is obtained by ignoring the second derivative of E^{scat} with respect to χ, e.g., see [129]. In other words, the GNI algorithm applies Newton optimization to the regularized data misfit cost functional. However, the second-order derivative of the cost functional is calculated under the approximation that the second derivative of the scattered field (*not* the cost functional) with respect to χ is zero.

data misfit cost functional as

$$\mathcal{C}(\chi) = \zeta \left\| M^2 - |E(\chi)|^2 \right\|^2 \tag{4.7}$$

where $|E(\chi)|$ denotes the magnitude of the simulated total field data due to a predicted contrast χ. In addition, ζ is the normalization factor that has been set to

$$\zeta = \left\| M^2 - |E^{\text{inc}}|^2 \right\|^{-2}. \tag{4.8}$$

Similar to the full data (complex) MR-GNI algorithm, the contrast at the n^{th} iteration is updated according to $\chi_{n+1} = \chi_n + \nu_n \Delta\chi_n$ (where ν_n was calculated using the methods in [128, Section 9]). As derived in the Appendix B.1, the correction $\Delta\chi_n$ at the n^{th} iteration is then found from

$$\begin{aligned} \Big[2\mathbf{J}_n^H \text{diag}(2|E(\chi_n)|^2 - M^2)\mathbf{J}_n\Big]\Delta\chi_n = \\ -2\mathbf{J}_n^H[E(\chi_n) \odot (|E(\chi_n)|^2 - M^2)] \end{aligned} \tag{4.9}$$

where 'diag' represents the diagonal operator that turns a vector into a diagonal matrix, and $\odot$ denotes the element-wise (Hadamard product) of two vectors of the same size. Note that the Jacobian matrix $\mathbf{J}_n$ used in (4.9) is the same as that used in (4.3). This may come as a surprise since in the full data (complex) GNI, $\mathbf{J}_n$ represents the derivative of the *scattered* field with respect to the contrast at the n^{th} iteration of the algorithm; and in phaseless GNI $\mathbf{J}_n$ should represent the derivative of the *total* field with respect to the contrast at the n^{th} iteration. However, since the total field is the summation of the incident and scattered fields, and noting that the incident field does not depend on the contrast, the derivative of the total field with respect to the contrast is the same as the derivative of the scattered field with respect to the contrast; i.e., $\frac{\partial E^{\text{scat}}}{\partial \chi} = \frac{\partial E}{\partial \chi}$. Also, note that in (4.9), $E(\chi_n)$ represents the vector that contains the simulated total field on the measurement domain S due to the predicated contrast χ_n. As can be seen in (4.9), both magnitude and phase of $E(\chi_n)$ have been used. This is not contradictory

to phaseless inversion since $E(\chi_n)$ represents the simulated total field data due to the predicted contrast χ, and *not* the phaseless measured data. Finally, we note that in all the examples shown herein, we use a trivial initial guess, $\chi = 0$, to start the phaseless GNI algorithm.

4.3.2 Regularization

Similar to the full data (complex) GNI algorithm that required regularization, the phaseless GNI algorithm also requires the regularization of its cost functional (4.7). Note that regularization is typically performed on the contrast χ; therefore, the regularization operators for the phaseless problem can be the same as the complex problem. Herein, we consider three types of multiplicative regularization schemes. The first is the weighted L_2 norm total variation multiplicative regularizer given in (4.4), which does not assume any particular prior information about the contrast profile in the ROI. The second is developed for shape and location reconstruction [32, 40]. This regularization assumes prior information about the complex permittivity values (thus, the contrast values) within the ROI. The problem then becomes one of finding the shape and location of the dielectric scatterers within the ROI. The third assumes prior information about the shape (structural information) of the target's regions of identical relative permittivity [130, 131]. If this spatial prior regularizer is used, the problem becomes one of reconstructing the appropriate complex permittivity values within the known regions of the ROI. When the phaseless GNI algorithm is used with each of these three regularization schemes, we refer to the resulting three different regularized algorithms as PGNI, SL-PGNI and SP-PGNI, respectively.

4.3.3 PGNI Algorithm

Similar to the complex GNI algorithm, we multiplicatively regularize the phaseless data misfit cost functional as

$$\mathcal{C}_n^{\text{reg}}(\chi) = \mathcal{C}(\chi)\ \mathcal{C}_n^{\text{MR}}(\chi). \tag{4.10}$$

Applying the GNI algorithm to this regularized phaseless cost functional, (4.9) will turn into the following regularized form

$$\begin{aligned}\Big[2\mathbf{J}_n^H \text{diag}(2|E(\chi_n)|^2 - M^2)\mathbf{J}_n + \tau_n \mathcal{L}_n\Big]\Delta\chi_n = \\ -2\mathbf{J}_n^H[E(\chi_n) \odot (|E(\chi_n)|^2 - M^2)] - \tau_n \mathcal{L}_n \chi_n\end{aligned} \tag{4.11}$$

where τ_n is $\mathcal{C}(\chi_n)/\zeta$. Herein, we refer to this phaseless algorithm as the PGNI algorithm. Note that the PGNI algorithm does not use any particular prior information about the ROI, and can therefore be considered as a blind phaseless inversion algorithm.

4.3.4 SL-PGNI Algorithm

This regularization scheme incorporates prior information about the expected contrast values within the ROI.[6] Therefore, it is mainly used to reconstruct the shape and location of the dielectric scatterers within the ROI. To this end, we augment (4.10) with an extra regularization term

$$\mathcal{C}_n^{\text{SL,reg}}(\chi) = \mathcal{C}(\chi)\ \mathcal{C}_n^{\text{MR}}(\chi)\ \mathcal{C}_n^{\text{SL}}(\chi) \tag{4.12}$$

[6] In microwave biomedical imaging we might know the expected permittivity values of the objects being imaged. For example, for microwave breast imaging we are mainly reconstructing fatty, fibroglandular, and perhaps cancerous tissues. Depending on the frequency and the achievable resolution, we may be able to reconstruct skin tissue as well. Therefore, it is possible to know *a priori* some expected permittivity values in the inversion process.

where the superscript 'SL' notes the suitability of this regularizer for shape and location reconstruction. This regularization term is given as [32, 40]

$$\mathcal{C}_n^{\mathrm{SL}}(\chi) = \frac{1}{A}\int_{\mathrm{ROI}} \prod_{\ell=1}^{L} \frac{|\chi(\mathbf{r}) - \chi_\ell|^2 + \alpha_n^2}{|\chi_n(\mathbf{r}) - \chi_\ell|^2 + \alpha_n^2} d\mathbf{s} \tag{4.13}$$

where χ_ℓ for $\ell = 1$ to L denotes the expected values of the complex contrast, and $\prod_{\ell=1}^{L}$ denotes the product of L different functions. The simplest form of this regularization term is *binary* regularization in which we are dealing with two values of the contrast: $\chi_1 = 0$ which is for the background medium, and χ_2 which represents the expected contrast value of the scatterer. We emphasize that the given prior information χ_ℓ contains no knowledge about the shape and location of the scatterers. In addition, α_n^2 is the steering parameter which is set to $\alpha_n^2 = \mathcal{C}(\chi_n)$. Applying the GNI algorithm to (4.12) will change (4.11) to

$$\begin{aligned}\Big[2\mathbf{J}_n^H \mathrm{diag}(2|E_n|^2 - M^2)\mathbf{J}_n + \tau_n\mathcal{L}_n + \tau_n \textstyle\sum_{\ell=1}^{L} \mathcal{R}_{n,\ell}\Big]\Delta\chi_n \\ = -2\mathbf{J}_n^H\Big[E_n \odot (|E_n|^2 - M^2)\Big] - \tau_n\mathcal{L}_n\chi_n \\ - \tau_n \textstyle\sum_{\ell=1}^{L} \mathcal{R}_{n,\ell}(\chi_n - \chi_\ell)\end{aligned} \tag{4.14}$$

where the regularization operators $\mathcal{R}_{n,\ell}$ when operating on a vector x of appropriate size are given as [32]

$$\mathcal{R}_{n,\ell}x = \frac{1}{A}\mathrm{diag}\left(\frac{1}{|\chi_n(\mathbf{r}) - \chi_\ell|^2 + \alpha_n^2}\right)x. \tag{4.15}$$

We refer to this phaseless GNI algorithm with prior expected contrast values as SL-PGNI.

4.3.5 SP-PGNI Algorithm

In contrast to the above shape and location regularization scheme which assumed prior information about the expected complex permittivity values, we now consider a spatial prior regularization scheme which assumes prior spatial (or structural) information in the

ROI without making any assumptions regarding their complex permittivity values. In this prior information approach, the shapes of the regions having identical permittivity are assumed to be known.[7] If this regularization scheme is used, the resulting inverse scattering algorithm attempts to reconstruct the relative complex permittivity values within these regions. Intuitively, one can think of this regularizer as reducing the amount of χ variables in the ROI, because there are fewer regions of identical permittivity than the original number of discrete cells in the ROI. To this end, (4.10) is augmented with an extra regularization term

$$\mathcal{C}_n^{\mathrm{SP,reg}}(\chi) = \mathcal{C}(\chi)\ \mathcal{C}_n^{\mathrm{MR}}(\chi)\ \mathcal{C}_n^{\mathrm{SP}}(\chi) \tag{4.16}$$

where the superscript 'SP' denotes the spatial prior information given to the regularizer. This regularization term is given as [130, 131]

$$\mathcal{C}_n^{\mathrm{SP}}(\chi) = \frac{\|p \odot (\mathbf{A}\chi)\|^2 + \gamma_n^2}{\|p \odot (\mathbf{A}\chi_n)\|^2 + \gamma_n^2}. \tag{4.17}$$

In $\mathcal{C}_n^{\mathrm{SP}}(\chi)$, $\mathbf{A}$ is a sparse matrix consisting of only zeros and ± 1. Its purpose is to enforce equality between contrast values in the specified regions of identical permittivity. In other words, the prior structural information of the ROI is stored in the matrix $\mathbf{A}$ via several 0 and ± 1 elements. (This choice of $\mathbf{A}$ was also utilized in [133, 134] in the form of an additive regularization scheme for complex GNI.) The probability vector p contains elements $0 \leq p_i \leq 1$. In this work, p_i has been set to 1 for all i's. Finally, γ_n^2 is a steering parameter chosen to be $\gamma_n^2 = \mathcal{C}(\chi_n)N$ where N is the length of the vector χ [130, Section D]. Applying the GNI algorithm to (4.16) will result in

$$\begin{aligned}\Big[2\mathbf{J}_n^H \mathrm{diag}(2|E_n|^2 - M^2)\mathbf{J}_n + \tau_n\mathcal{L}_n + \tau_n\mathcal{S}_n\Big]\Delta\chi_n = \\ -2\mathbf{J}_n^H[E_n \odot (|E_n|^2 - M^2)] - \tau_n\mathcal{L}_n\chi_n - \tau_n\mathcal{S}_n\chi_n\end{aligned} \tag{4.18}$$

[7] For example, in a combined magnetic resonance imaging (MRI) and microwave imaging system, the high resolution structural information obtained from the MRI can be given as spatial prior information to the microwave imaging system [132].

where the operator $\mathcal{S}_n$ acting on a vector x of appropriate size is

$$\mathcal{S}_n x = \frac{1}{\|p \odot (\mathbf{A}\chi_n)\|^2 + \gamma_n^2} \mathbf{A}^H \left(p \odot (p \odot (\mathbf{A}x))\right). \tag{4.19}$$

Herein, we refer to this phaseless GNI algorithm with prior spatial information as SP-PGNI.

4.4 Calibration of the Experimental Data

4.4.1 Classification – Review

In microwave imaging, there will always be some discrepancy between the actual measurement environment, and the numerical model used in the inversion algorithm. To alleviate these discrepancies, so-called data calibration techniques such as the scattered field or the incident field calibration methods [103] are used.[8] For phaseless inversion, the scattered field data are not available, and therefore, the scattered field calibration technique cannot be used. Therefore, we decided to use the incident field calibration technique for our experimental data. There are at least two ways that incident field calibration can be applied. In the first method, a simulated incident field, such as a zeroth-order Hankel function of the second kind is assumed for the incident field, and then complex calibration coefficients are found to reduce the discrepancy between the simulated and measured incident field data. These calibration coefficients are then used to modify the raw experimental data. The second method is a more general way, which is based on the so-called source reconstruction method (SRM).[9]

[8] Similar to the calibration object in radar cross section measurements, the scattered field calibration technique in microwave imaging uses an object, such as a metallic cylinder [135], for which the complex scattered fields are analytically known. These analytical expressions and the measured scattered field data are then compared to construct complex-valued calibration coefficients, which will then used to calibrate the actual measured data.

[9] The source reconstruction method is, in fact, an electromagnetic inverse source algorithm [36].

4.4.2 SRM Calibration

In the SRM-based calibration method, the SRM is used to find equivalent surface current distributions for the transmitting antennas that can also generate the measured incident field data. Once these equivalent currents are found, they can be used in the GNI algorithm to represent the actual antennas. Since these equivalent currents are associated with the *raw* incident field data, the *raw* phaseless total field data are directly given to the inversion algorithm to be inverted. Therefore, as opposed to the previous calibration methods, the SRM-based calibration method makes it possible to invert the raw experimental data directly.

Herein, we have used the second method; i.e., the SRM for incident field calibration. The details of this calibration method can be found in [50]. To this end, we have utilized the SRM to replace each transmitting antenna with its equivalent currents. That is, for example, if 24 antennas are present in a microwave imaging setup, we have replaced them with 24 sets of equivalent currents. We have used both the magnitude and phase of the measured incident field. Thus, the inverse source problem associated with the SRM becomes a linear inverse source problem. Due to the fact that the L-curve method is particularly suited for linear ill-posed problems [33, 108], we have used the L-curve method to choose an appropriate solution when performing SRM.[10]

4.4.3 Calibration Limitation

Note that the above calibration method requires the magnitude and phase of the incident field data (*not* the phase of the total field data). The presence of the phase data for the incident field is not a bad assumption since it can be regarded as part of system characterization (antenna characterization) prior to performing imaging. This assumption is also present in many other phaseless microwave imaging algorithms [110, 111, 117, 118,

[10]The L-curve method requires determining the knee point of the L-curve; in our implementation the knee point is chosen in an *ad hoc* manner.

120]. In all of these algorithms, the total field data, but not the incident field data, are assumed to be phaseless. If this assumption is not made, we would have to use a phaseless SRM algorithm, e.g., see [24], to characterize the antennas using measured phaseless incident fields. Once the equivalent currents of the antennas are obtained using phaseless incident fields, it can be used in the phaseless GNI algorithm similar to the above. Therefore, in summary, similar to other phaseless microwave imaging algorithms, this paper assumes phaseless total field data but considers complex incident field data.

4.5 Results

Herein, we show synthetic and experimental results to evaluate the performance of our phaseless GNI algorithms. First, the PGNI, SL-PGNI, and SP-PGNI algorithms are used to reconstruct images of a pair of lossy concentric squares in the ROI using synthetically generated data. Next, experimental data collected from the Institut Fresnel in France [3] are used to validate the PGNI, SL-PGNI, and SP-PGNI algorithms. Because the experimental data from Institut Fresnel are from lossless targets, we then consider experimental data obtained from a skinless bovine leg [4] to evaluate the performance of the PGNI, SL-PGNI, and SP-PGNI algorithms against a lossy object. In addition to lossy versus lossless objects, there are two other differences between these two data sets: (I) the Fresnel data sets use a mechanical scanning probe to collect the data whereas the bovine leg data are collected by 24 co-resident dipole antennas; (II) the background medium in the Fresnel data sets is air whereas the background medium in the bovine leg data set is salty water.[11]

Since these experimental data sets all contained measured magnitude and phase data, we removed the phase of the measured total field data, and only worked with the measured

[11]To reduce unwanted reflections, the Fresnel data sets were collected in an anechoic chambers with absorbers. On the other hand, for the bovine leg data, salt has been added to water to make it lossy, thus reducing the reflections from the imaging chamber wall. This is necessary since the imaging algorithm assumes a free space Green's function that does not take into account the reflections from the walls of the imaging chamber.

magnitude-only total field data. Finally, we note that the iterative nature of the phaseless inversion algorithms means that a stopping condition is necessary. In this work, we stopped the algorithm when $\mathcal{C}(\chi_n)$ decreased below 10^{-3} or when the change in the reconstructed contrast was smaller than 10^{-4} after two consecutive iterations. More detail on the convergence behaviour of the proposed algorithms can be found in Appendix B.2.[12]

4.5.1 Synthetic Concentric Squares Data Set

To validate our phaseless GNI algorithms, synthetic data at 4 GHz were created from a pair of concentric dielectric squares with a background of free-space ($\epsilon_r = 1$). This experiment is similar to the synthetic examples in [110, Section IV] and [111, Section 5]. The relative complex permittivities of the outer and inner squares were $\epsilon_r = 1.3 - 0.4j$ and $\epsilon_r = 1.6 - 0.2j$, respectively, see Figure 4.1(a)-(b). For phaseless data collection, 36 transceivers were located on a circle of radius 76 cm around the origin. (The transceivers are assumed to be infinite line sources, thus, they are numerically modelled by zeroth-order Hankel functions of the second kind.) The ROI was discretized into 43 by 43 square elements and was 166 mm by 166 mm in size. The inversion was done at a single frequency of 4 GHz.[13] The results from attempting to reconstruct the lossy concentric squares from phaseless total field data using the PGNI, SL-PGNI, and SP-PGNI algorithms are shown in Figure 4.1(c)-(h). As noted earlier, the PGNI is *blind* phaseless inversion (no prior information is given to the algorithm). In the case of SL-PGNI, the phaseless inversion algorithm was provided with the true three contrast values as prior information, i.e., the contrast value of the background medium and the contrasts of the two squares. The SL-PGNI then reconstructs the shape and location of the objects being imaged. Finally, in the case of the SP-PGNI, the spatial map of the target (i.e. the regions of identical

[12] In this work we have not investigated the convergence behaviour of these phaseless GNI algorithms for various contrast values and imaging domain sizes. We speculate that with increasing contrast values and/or imaging domain sizes the degree of non-linearity of the problem increases; thus the algorithm might experience convergence to inappropriate local minima. To alleviate this the use of a non-trivial initial guess can be a potential solution.

[13] The synthetic data were created on a different grid to avoid the so-called inverse crime.

permittivity) was provided to the phaseless inversion algorithm as prior structural information. The SP-PGNI then reconstructs the complex permittivity values in these spatial regions. As can be seen, the SL-PGNI and SP-PGNI reconstructions were more accurate than that of the PGNI algorithm. This is to be expected as the latter two algorithms include more information about the objects being imaged whereas the PGNI algorithm is a blind inversion.

4.5.2 Experimental FoamDielIntTM Data Set

To study the performance the phaseless GNI algorithms with experimental data, we consider the measured data provided by the Institut Fresnel in France [3]. The phase of the measured total field was disregarded and only its magnitude data were used. The first target consists of two dielectric cylinders, one inside the other, and the background is air. The inner-most cylinder is 31 mm in diameter with a relative permittivity of $\epsilon_r = 3 \pm 0.3$, and is slightly offset from being concentric with the outer cylinder by 5 mm in the x-direction. The outer cylinder has a relative permittivity of $\epsilon_r = 1.45 \pm 0.15$ and a diameter of 80 mm. This target is referred to as FoamDielIntTM by [3] and is shown in Figure 4.2(a). Note that the imaginary parts of the complex permittivities of these cylinders are zero, and therefore, the objects being imaged are lossless. The experimental dataset used for the FoamDielIntTM inversions included eight transmitters and 241 receivers for each transmitter. The transmitters and receivers were located 1.67 m from the centre of the ROI [3] and the ROI was discretized into 65 by 65 elements and was 150 mm by 150 mm in size. The frequency of inversion was 2 GHz.

In Figure 4.2(b)-(c) the result of inverting the FoamDielIntTM data with PGNI are shown and the reconstructed overall shape and permittivities are reasonable; however, they are not very accurate. For example, the reconstructed size of the inner cylinder is greater than the actual one, and its reconstructed permittivity is smaller than its true permittivity. In addition, there is a small imaginary part present in the reconstructed permittivity.

In Figure 4.2(d)-(e), the reconstructed permittivity using SL-PGNI is shown. In the SL-PGNI algorithm, the relative permittivities of the cylinders are assumed to be known and are given as prior information to the phaseless inversion algorithm. As a result, the SL-PGNI algorithm reconstructs the shape and location of the target more accurately compared to the blind phaseless inversion algorithm (PGNI). Similar to the PGNI reconstruction, the SL-PGNI reconstruction also shows small imaginary parts in the complex permittivity (i.e., some small loss).[14]

We now invert these phaseless measured data using the SP-PGNI algorithm. To this end, we need to give the structural information of this target as prior information to SP-PGNI. Ideally, this spatial prior information should come from a higher resolution imaging modality such as magnetic resonance imaging (MRI). Once high resolution structural information is given to SP-PGNI, this inversion algorithm will aim to find the complex permittivity values in different regions from phaseless data. However, since MRI data were not available for this target, we use a different method to create the spatial prior map; we used the full data (complex) MR-GNI algorithm to invert the data set at 4 GHz, 6 GHz and 10 GHz simultaneously. The achieved inversion result is then used to create spatial priors for this target as shown in Figure 4.3(a) where R1, R2, and R3 denotes the three spatial regions.[15] (Note that we do not provide any prior information regarding the complex permittivity values for SP-PGNI.) These spatial priors are then given to the SP-PGNI algorithm to find the complex permittivity at these regions. The reconstruction results using the SP-PGNI algorithm are shown in Figure 4.2(f)-(g).

[14]The fact that there are small imaginary parts in the reconstructed permittivity using the SL-PGNI algorithm may come as a surprise. This is due to the fact that the SL-PGNI gets the value of the permittivity as the prior information. In this particular inversion, we have provided the SL-PGNI algorithm with the relative permittivity of 3 and 1.45 (and, of course the relative permittivity of 1 for the background). That is, the imaginary parts of the relative complex permittivities in the prior information were zero. However, these values are only enforced as *soft* regularization in the sense that the inversion algorithm will favour these values but still has the chance to not completely enforce them.

[15]The procedure to extract these spatial priors has been described in [130] which applies a MATLAB *kmeans* function to the final reconstruction obtained from full data inversion.

4.5.3 Experimental FoamTwinDielTM Data Set

Next, inversion results for the FoamTwinDielTM experimental data from the Institut Fresnel are shown [3]. (Note that we once again disregard the phase and invert just the magnitude of the total field data.) For this experiment, the target is similar to the FoamDielIntTM case, except there is another small cylinder with the same dielectric properties and size as the inner-most cylinder external to the outer cylinder. The two small cylinders are 55.5 mm apart. An illustration of the FoamTwinDielTM target is shown in Figure 4.4(a). The data collection for this test included 18 transmitters with 241 receivers each. Once again, the transmitters and receivers are located on a circle of radius 1.67 m and the ROI was discretized into a 65 by 65 grid with side lengths of 150 mm each. The results of the inversion using the PGNI, SL-PGNI and SP-PGNI algorithms are shown in Figure 4.4(b)-(g) for a frequency of 4 GHz. (Similar to the previous example, the spatial priors for the SP-PGNI algorithm, shown in Figure 4.3(b), were obtained through a multi-frequency full-data MR-GNI algorithm.) In addition, similar to the previous example, the relative permittivity values given as prior information to the SL-PGNI algorithm are 3, 1.45, and 1. It can be observed once again that adding more information through more sophisticated regularization schemes with the SL-PGNI and SP-PGNI algorithms enables sharper reconstructions, with more evidence of the larger cylinder. Comparing the reconstructions from the SL-PGNI and SP-PGNI algorithms shows that for the SL-PGNI algorithm, the permittivities are smooth but the shape of the reconstructed cylinders is not completely circular. In contrast the SP-PGNI algorithm has a much more accurate shape, but the permittivity is not as smooth overall for the small dielectric cylinders as the SL-PGNI algorithm. This result is expected as both algorithms do well reconstructing what they have been informed is prior information.

4.5.4 Experimental Skinless Bovine Leg Data Set

In order to test the phaseless GNI algorithms with a lossy target and background medium in the ROI, we use the experimental data collected from a skinless bovine leg in a salt-water medium using 24 co-resident dipole antennas [4]. (Similar to the previous cases, we ignore the phase of the measured total field data, and invert only its magnitude data.) The ROI is a square discretized into a 50 by 50 grid with a total length of 120 mm. The data was collected at 0.8 GHz with the relative complex permittivity of the background being $\epsilon_r = 76 - 14j$. The expected relative permittivity values of the bone (centre-most region of the bovine leg) is $\epsilon_r = 26 - 8j$, and flexor (region around bone) is $\epsilon_r = 54 - 18j$ [4]. Prior to showing the phaseless inversions, let us take a look at the inversion of the full data (magnitude and phase) as shown in Figure 4.5(a)-(b).[16]

For this lossy experimental data set, the blind phaseless inversion algorithm (i.e., the PGNI algorithm) failed to provide any meaningful reconstruction; thus, it is not shown here. We then tried the phaseless inversion algorithms incorporating prior information; i.e., the SL-PGNI and SP-PGNI algorithms; the reconstruction results using these phaseless algorithms are shown in Figure 4.5(c)-(f). It can be seen that the SL-PGNI algorithm performed poorly when compared with the SP-PGNI algorithm. This is an indication that the spatial prior information, shown in Figure 4.3(c), may have been more useful in reconstructing the true target than the prior knowledge of expected permittivities. Also, in the reconstruction process, we have limited the variation of the allowed relative complex permittivity as follows: $1 \leq \mathrm{Re}(\epsilon_r) \leq 80$ and $-30 \leq \mathrm{Im}(\epsilon_r) \leq 0$. Due to this enforcement, the reconstructed permittivity of the bone using the SP-PGNI method shown in Figure 4.5(e)-(f) looks very uniform, but is mistakenly similar to free-space and not bone (i.e., $\epsilon_r = 26 - 8j$) as it should be. In addition, the phaseless inversion of the skinless

[16]Herein, for the full data (complex) case, we have also used the SRM-based incident field calibration method. We note that the inversion of these full data using the scattered field calibration method, as shown in [4], seems to be better than the inversion shown in Figure 4.5(a)-(b) (and, also shown in [50]). However, since the use of the scattered field calibration method was not possible for the phaseless case, we have also calibrated the full data using the SRM-based incident field calibration method for consistency.

bovine leg data set had another challenge: the steering parameters of the phaseless inversion algorithms (i.e., δ_n^2, α_n^2, and γ_n^2) had to be modified for this particular example to work.[17] That is, the phaseless inversion of this data set was more sensitive to the overall regularization weight as compared to the other cases. This was perhaps due to the lossy nature of the complex permittivities which further reduces the information content of the measured data.

It is instructive to investigate the information content available for the phaseless inversion in this skinless bovine leg data set. To this end, let us take a look at Figure 4.6(a), where the measured squared magnitude of the total field (black) and the measured squared magnitude of the incident field (blue) are shown for a given transmitter. On the other hand, Figure 4.6(b) shows the phase of the total measured (black) and incident (blue) field data for the same transmitter. As can be seen, as opposed to the phase data, the magnitude data of the total and incident fields are quite similar, and therefore, the information content of the imaging experiment is mainly encoded in the phase data that cannot be used for phaseless inversion. This is the main reason behind the difficulty of performing phaseless inversion on this data set. Let us now take a look at the phaseless inversion result using the SL-PGNI algorithm shown in Figure 4.5(c)-(d). As can be seen this phaseless inversion was relatively unsuccessful, however, if we now take a look at the simulated squared magnitude of the total field data at the last iteration of this inversion algorithm, i.e., the red curve in Figure 4.6(a), we understand that the simulated data are quite similar to the measured magnitude data. Therefore, the phaseless inversion

[17]This modification was done in an *ad hoc* manner. Note that in the multiplicative regularization scheme, the steering parameter is the only parameter related to the regularization weight that the user has control over. (The other regularization-weight related parameter is τ_n which is automatically determined by the convergence behaviour of the algorithm; thus, the user has no control over this parameter.) If an inversion algorithm does not work properly, a likely reason is over-regularization or under-regularization. In this particular example, due to having a lossy object (skinless bovine leg) and a lossy matching fluid (salt-water), the problem is more ill-posed. In addition, due to the phaseless approach, the problem is also more nonlinear as compared to its full data counterpart. Since the phaseless SL-PGNI and SP-PGNI of the skinless bovine leg using the standard steering parameters did not work properly, our speculation was that the regularization scheme needs to be applied with a stronger weight. To this end, we made the steering parameters smaller for the skinless bovine leg example thereby changing the weight of the regularization operators. For example, consider the steering parameter for the spatial prior case, i.e., the SP-PGNI algorithm. If we make γ_n^2 smaller, then the weight of the regularization operator $\mathcal{S}_n$ can increase due to having γ_n^2 in the denominator of (4.19).

algorithm performed well; however, there was not a great deal of information left to be extracted from the magnitude-only data to improve the reconstruction result. Now, if we look at the simulated phase of the total field data at the last iteration of this phaseless algorithm, i.e., red curve in Figure 4.6(b), we see that the simulated phase data are different than the phase of the measured total field data (even if this phase difference is reduced by considering a phase shift of 2π at Rx number 9 for the simulated or measured total field). Since these measured phase data were not provided to the SL-PGNI inversion algorithm, the algorithm was not able to take advantage of the embedded information content in this dataset to improve its reconstruction.

4.6 Conclusion

A novel phaseless GNI algorithm was developed and was augmented with three forms of multiplicative regularization: (i) weighted L_2 norm total variation regularization, (ii) weighted L_2 norm total variation regularization combined with prior information regarding the expected complex permittivity values of the objects being imaged, and (iii) weighted L_2 norm total variation regularization combined with prior information regarding the structural information of the regions of identical permittivity of the objects being imaged. We have referred to these three implementations of the phaseless GNI algorithm as the PGNI, SL-PGNI, and SP-PGNI algorithms, respectively. These algorithms were shown to be able to invert synthetic phaseless data, experimental phaseless data from lossless and lossy targets. The incorporation of prior information was shown to play a strong role with these phaseless GNI algorithms to compensate for the lack of phase of the total field data.

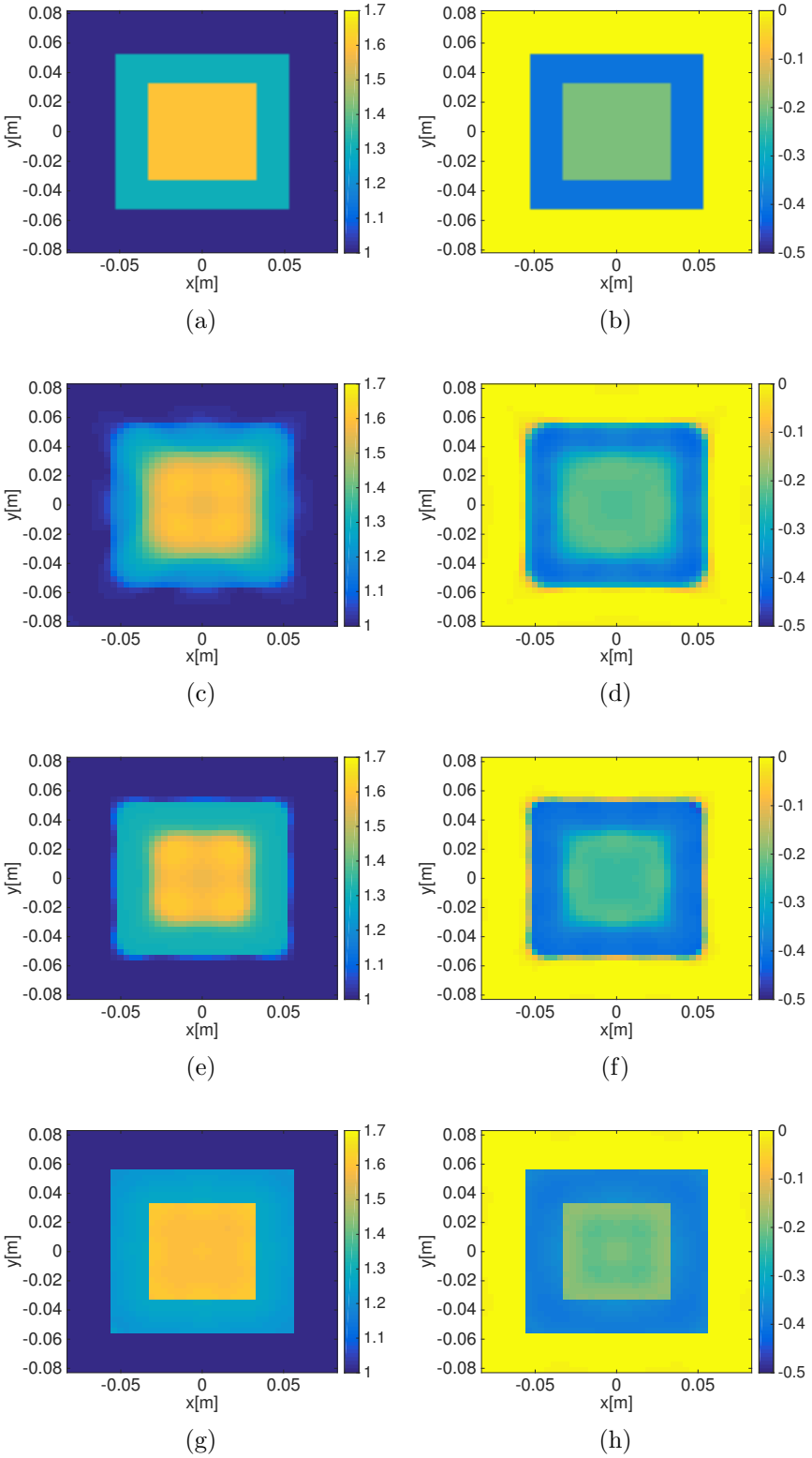

Figure 4.1: The real (left) and imaginary (right) parts of the reconstructed relative permittivity from the inversion of the synthetically generated phaseless total field data from two lossy concentric squares (first row) at 4 GHz using the PGNI (second row), SL-PGNI (third row), and SP-PGNI (fourth row) algorithms, respectively.

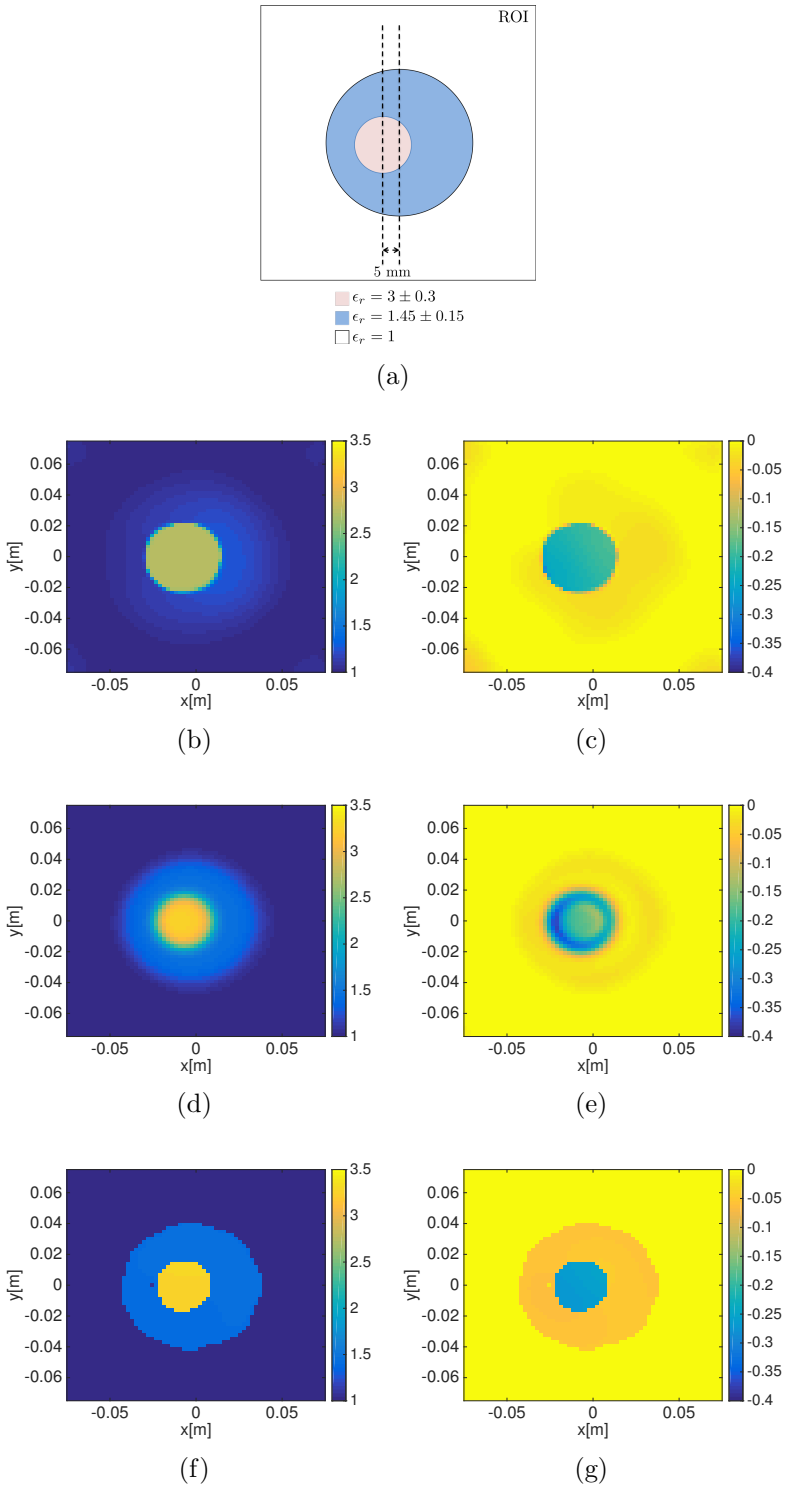

Figure 4.2: The FoamDielIntTM Fresnel data [3], *without* the phase of the measured total field, are inverted. An illustration of the true target is shown (top row) before showing the reconstructed permittivity results for a single frequency of 2 GHz from the PGNI (second row), SL-PGNI (third row), and SP-PGNI (fourth row) algorithms. The real (left) and imaginary (right) parts of the reconstructed relative permittivity from the inversion are reported.

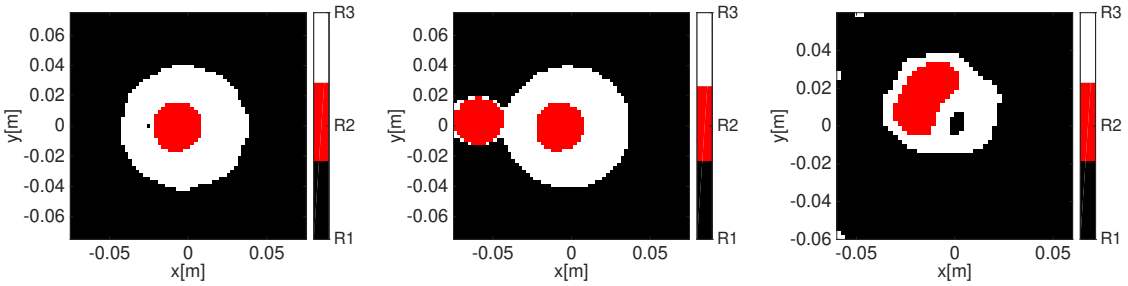

(a) (b) (c)

Figure 4.3: The spatial priors (SP) used in conjunction with the SP-PGNI algorithm for (a) FoamDielIntTM, (b) FoamTwinDielTM, and (c) skinless bovine leg. The colorbar indicates three spatial regions denoted by R1, R2, and R3. (Some of these spatial regions contain errors, e.g., the black region within R3 in (c) is likely to be an error.)

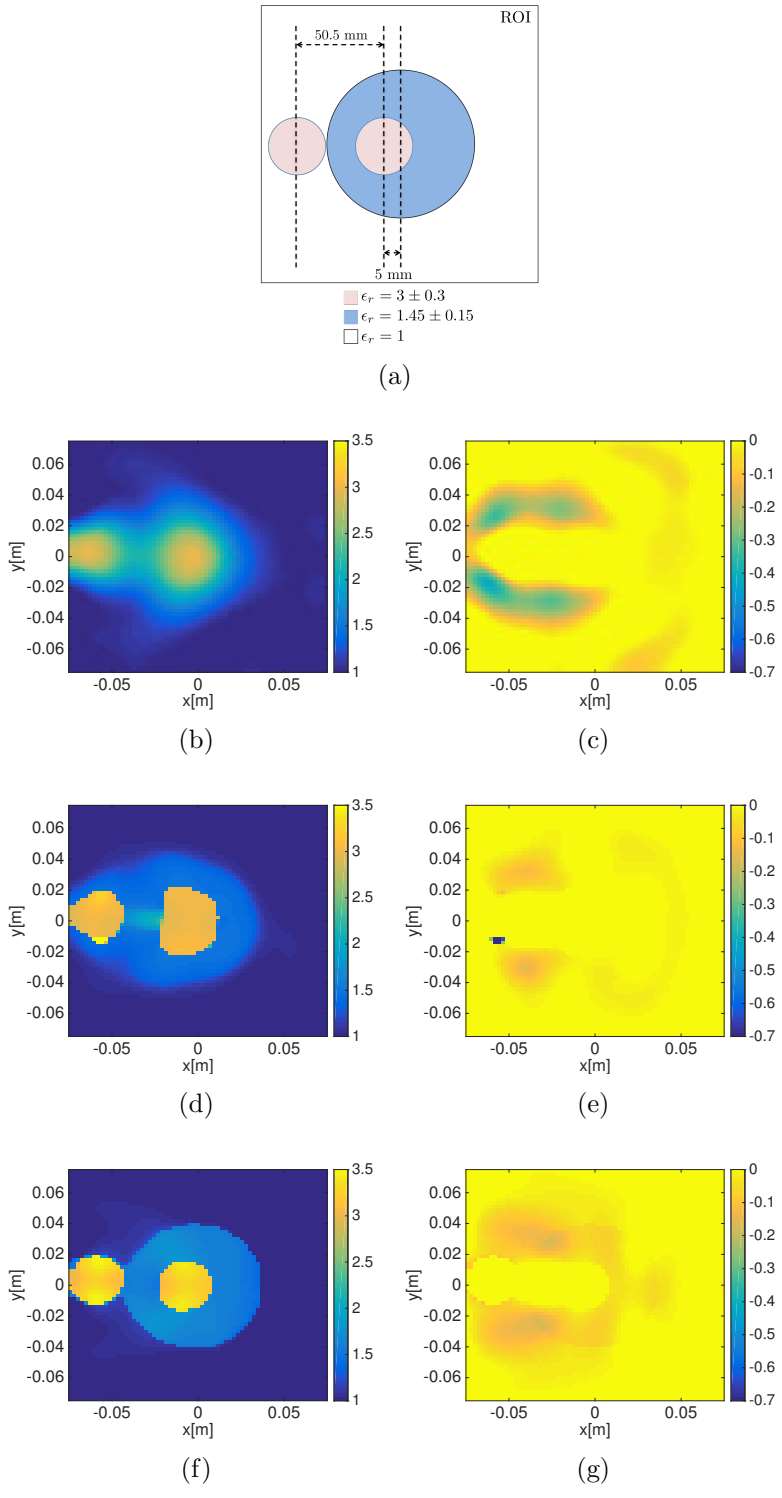

Figure 4.4: The FoamTwinDielTM dataset [3] *without* the phase of the measured total field, are inverted. An illustration of the true target (top row) is presented. The real (left) and imaginary (right) parts of the reconstructed relative permittivity from inversions at 4 GHz using the PGNI (second row), SL-PGNI (third row), and SP-PGNI (fourth row) algorithms are shown.

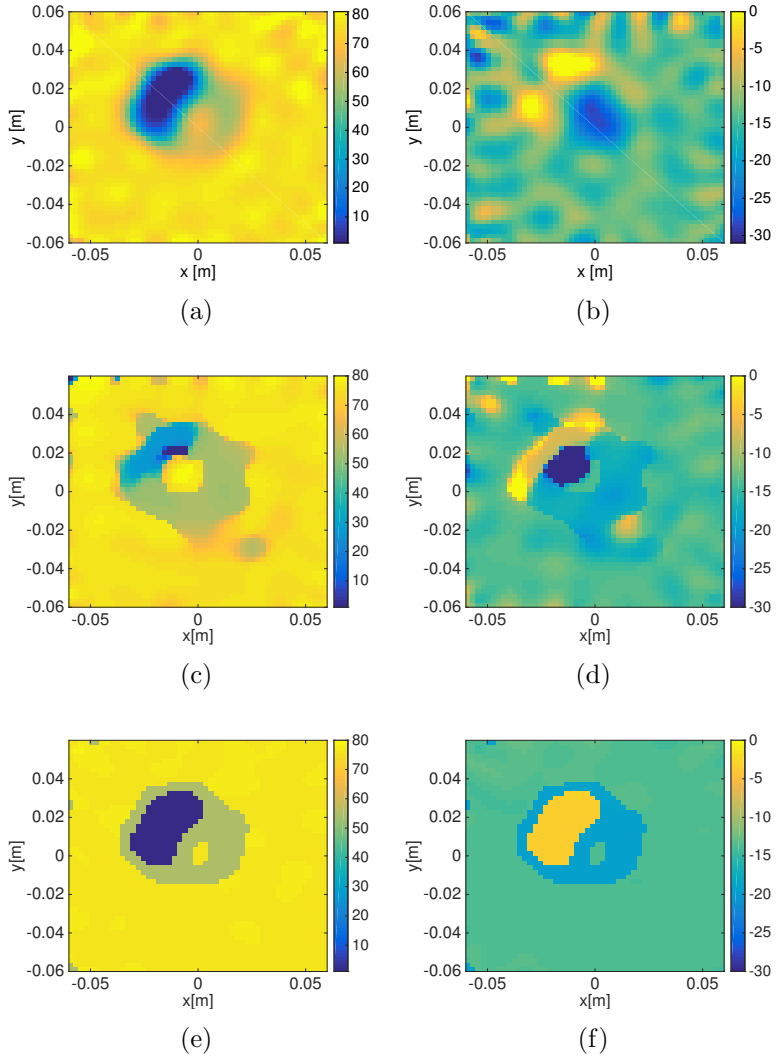

Figure 4.5: Experimental inversion results for a skinless bovine leg in a salt water medium [4]. The real (left) and imaginary (right) parts of the reconstructed relative permittivity at 0.8 GHz using the full data (complex) MR-GNI (first row), and the phaseless SL-PGNI (second row) and SP-PGNI (third row) algorithms are shown.

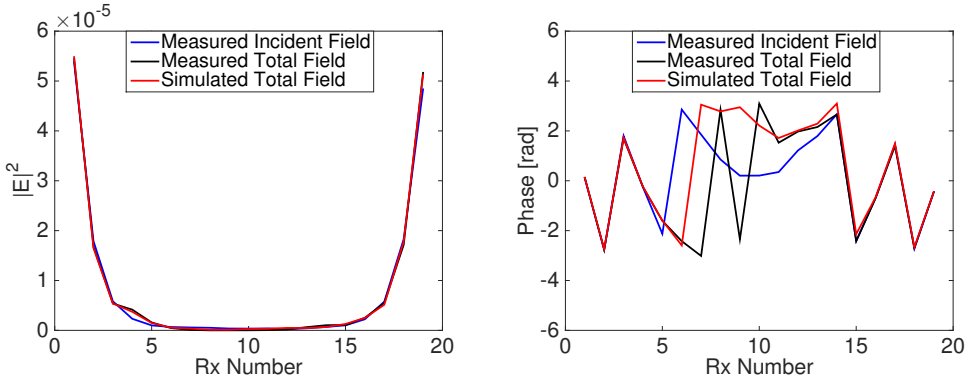

(a) (b)

Figure 4.6: The (a) squared magnitudes of the measured total field, the measured incident field, and simulated total field from the SL-PGNI algorithm are shown to be very similar showing the lack of information present about the bovine target in the measured magnitude data. The (b) phase distributions are then shown to be more varied (even if this phase difference is reduced by considering a phase shift of 2π at Rx number 9 for the simulated or measured total field). This is shown for one transmitter but the same plots are similar for all transmitters.

Chapter 5

A Combined Inverse Source and Scattering Technique for Dielectric Profile Design to Tailor Electromagnetic Fields

Preface

In the previous chapter, an inverse scattering approach was presented that could characterize dielectric objects with phaseless data. In this chapter we look to the *design* of dielectric lens/antennas using similar principles. One possibility to explore this concept was to use the algorithms developed in the previous chapter with *desired* electromagnetic data instead of *measured* data for inversion; we briefly explored this in [82]. However, to be able to facilitate the design of passive, lossless, and reflectionless dielectric lenses using a variety of different types of electromagnetic data, we develop a combined inverse source and scattering technique in this chapter.

In the developed method, complex electric field, phaseless electric field, and far-field criteria data can be used as the electromagnetic data to reconstruct a dielectric profile as the main property of interest. The physical model is based on Maxwell's equations in integral form, specifically, the data and domain equation are used for the inverse scattering part and the electric-field integral equations are used for the inverse source part. Two cost functionals need to be minimized separately: one for the inverse source problem, and one for the inverse scattering problem. Regularization techniques are utilized to bias the solution of a dielectric profile that can facilitate physical implementation. Note that in this method we are using the surface and volume equivalence principles separately to design the lens.

To the best of the authors' knowledge this is the first time a combined inverse source and scattering methodology has been presented that is capable of designing dielectric profiles that when illuminated by a single feed can satisfy user specified far-field performance criteria, including main beam direction, null locations, and half-power beam width (HPBW). The presented framework is capable of using existing inverse scattering algorithms that are used for characterization applications such as microwave imaging without much modification. In fact, in this chapter we show examples using contrast source inversion and Gauss-Newton inversion type inverse scattering algorithms.[1] The material presented in this chapter was published as a journal paper for IEEE Transactions on Antennas and Propagation [136].[2]

Abstract

This paper augments existing gradient-based inverse scattering algorithms to enable the design of reflectionless lossless permittivity profiles within a given design domain that can

[1]Contrast source inversion directly uses of the volume equivalence principle while it can be perceived that Gauss-Newton inversion algorithms use this principle indirectly.

transform an input incident field into an output field of desired characteristics. These desired characteristics are often some user-defined far-field performance criteria such as main beam directions, null directions, and half-power beamwidth (HPBW). To this end, two extra steps will be performed prior to the inverse scattering step. Firstly, an inverse source algorithm inverts the desired far-field performance criteria to infer a set of equivalent surface currents on a boundary close to the design domain. These equivalent currents are then converted to a set of fields values that constitute the required aperture fields. Secondly, these aperture fields are scaled such that the input incident power to the design domain is approximately equal to the output power leaving the design domain. Finally, the desired scattered fields are formed and then inverted by an inverse scattering algorithm to reconstruct a lossless reflectionless dielectric profile within the design domain. We also show that the inverse scattering algorithm can employ appropriate regularization methods, in particular a binary regularization term, to facilitate the physical implementation of reconstructed dielectric profiles.

5.1 Introduction

In electromagnetic inverse scattering, the goal is to infer the internal properties of an unknown irradiated domain from external electromagnetic fields. To this end, the unknown domain is illuminated by electromagnetic fields and the resulting emanating scattered electromagnetic fields of the domain are recorded. The desired internal properties of the domain are then found from these external scattered electromagnetic fields; for example, the domain's dielectric properties are often calculated. Electromagnetic inverse scattering techniques have been commonly used for imaging applications [107, 137, 138] within a wide range of frequencies, e.g., from a few Hertz [139] to the optical frequency range [140]. For example, in microwave breast imaging [74] these algorithms are used to infer (reconstruct) the dielectric profile (relative complex permittivity) of the breast from external measured scattered field data. To this end, inverse scattering algorithms iteratively update a predicted dielectric profile so that its simulated scattered fields match (ideally)

the *measured* scattered fields. This is done by minimizing a data misfit cost functional within an iterative process. Upon its convergence, this minimization yields a reconstructed dielectric profile [4, 30]. Several optimization approaches have been proposed to minimize the data misfit cost functional, which can be broadly classified into global [141] and gradient-based optimization approaches [142]. The latter has found more use in the literature due to its computational efficiency, and it is thus considered in this paper. We also note that inverse scattering can be done in a non-iterative fashion under some approximations such as the Born approximation (weak scatterers). These non-iterative inversion approaches are mainly concerned with creating qualitative reconstruction (as opposed to quantitative), and are therefore not considered in this paper.

More recently, the electromagnetic inverse scattering framework has been used for design applications [9, 22, 80–82, 143–145]. In such problems, the purpose is to design a dielectric profile that is capable of transforming the incident field of a feed antenna into a desired field. In this scenario, the inverse scattering algorithms are attempting the same procedure as in the imaging case, except that instead of measured scattered fields, we now use the *desired* scattered fields. Consequently, in this design problem, the non-uniqueness [28] of this inverse problem can be advantageous. In contrast to the imaging problem, a specific *true* dielectric profile is not sought; instead, an *appropriate* one needs to be found. Therefore, the non-uniqueness of the problem can be exploited through different regularization techniques to choose a dielectric profile that may be, for example, easier to fabricate. However, the problem of existence is more of an issue in the design problem than the imaging case: one must ensure that the desired fields must be physically realizable by interrogation of a dielectric profile of certain size. For example, to be able to transform an incident field to a power pattern of high directivity, we first need to make sure that the size of the dielectric profile provides a sufficient effective aperture size for this transformation; e.g., see [9] for a method to avoid super directivity.

There are also certain practical challenges that must be addressed when using inverse scattering for design. Firstly, it would be advantageous if the design framework could make use of different types of desired data. In previous work, the desired field pattern is

specified as either (i) complex field values or (ii) power or amplitude values [9, 22, 82]. For example, in inverse scattering for dielectric cloak design [22], the desired scattered field is conveniently known: it needs to be zero to represent no scattering signature. However, in most practical design problems, only certain (far-field) specifications such as the main beam direction, half-power beam width (HPBW), and null locations are known. In such cases, obtaining desired scattered fields are not straightforward, and consequently it is not clear how to apply existing state-of-the-art gradient-based inverse scattering algorithms to such design problems. This is in particular due to the complexity of finding the gradient operators (and the Hessian matrix) for such general cases[3], and the enforcement of power conservation for the input and output fields. Therefore, a more flexible design framework is necessary to enable the use of gradient-based inverse scattering algorithms for the design of dielectric profiles from the knowledge of performance criteria such as HPBW or null directions. Secondly, there is the challenge of facilitating the physical implementation of the designed dielectric profile. It would be preferred that a given inverse scattering design technique make it easy for the designers to not only generate the desired field specifications, but also reduce the effort of physically implementing the final dielectric profile. This can be seen in [9, 80, 143], where the unknown of interest is expanded on a set of basis functions to simplify the fabrication process. For example, in one case the dielectric profile is implemented with a set of dielectric rods (projection-based regularization) [80]. This is easier to implement than a continuously varying dielectric profile. As another example, appropriate regularization terms have been used with inverse scattering algorithms to favour positive permittivity values [9] or to favour circular symmetry etc [143].

In this work, we present a flexible gradient-based inverse scattering design methodology that can address the challenges stated above. The method involves three main steps: (i) determine the desired electromagnetic fields in the required form at the required locations using an inverse source algorithm, (ii) enforce total power conservation, and (iii) solve the inverse scattering problem using the appropriate algorithm and regularization to facilitate

[3]Note that this is not the case for global optimization algorithms, e.g., in [146, 147] a genetic algorithm and a particle swarm optimization algorithm are used for dielectric lens design.

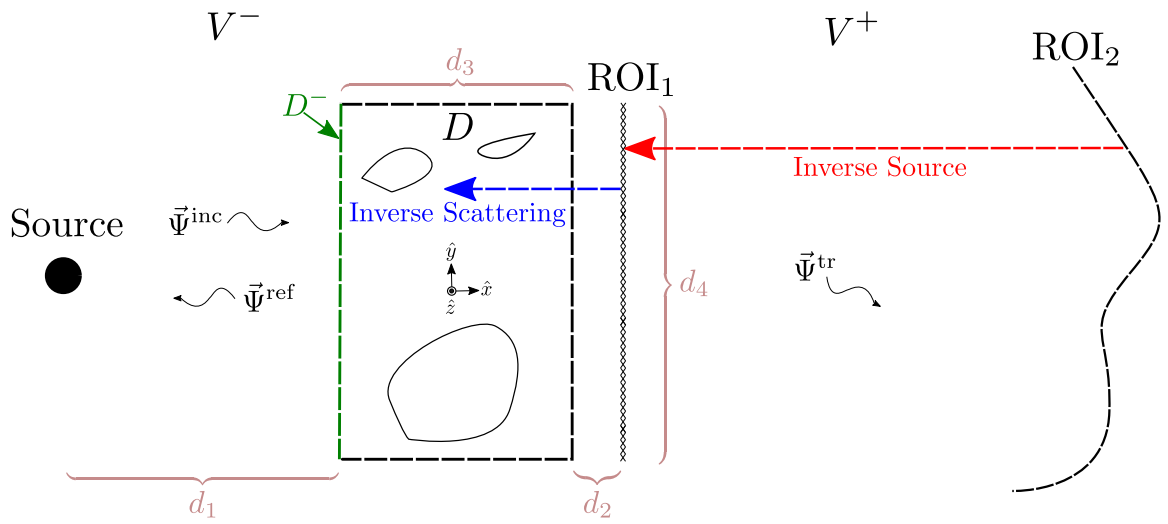

Figure 5.1: The schematic of the design problem. A dielectric profile in the design domain D (shown by a dashed rectangle) with a width of d_3 and a height of d_4 is to be determined such that it can transform an incident field $\vec{\Psi}^{\text{inc}}$ to a desired output/transmitted field ($\vec{\Psi}^{\text{tr}}$) when illuminated by a known source/feed (black circle) from a distance d_1. The feed is on the input side V^- of D and the transmitted field is on the output side V^+. The input boundary of D is denoted by D^-. The dielectric profile is designed by utilizing the desired complex field on a region of interest ROI$_1$ with a size of d_4 a distance d_2 from D with the appropriate inverse scattering algorithm and regularization methods. If only far-field specifications are known (e.g., main beam direction, null locations, etc.), then an inverse source problem is first solved to obtain the fields on ROI$_1$ from the specifications on ROI$_2$ before the dielectric profile is designed with the inverse scattering algorithm.

physical implementation. We start by defining the problem and scope in Section 5.2. Then we explain our inverse scattering methodology in detail in Section 5.3 before using it to design dielectric objects capable of near-field and far-field transformations in Section 5.4. In this paper, we consider the two-dimensional (2D) transverse magnetic (TM$_z$) problem with the time dependency of $\exp(j\omega t)$.

5.2 Problem Description

Let us consider the design domain D shown in Figure 5.1. This is the domain that will support a *lossless* non-magnetic permittivity profile to transform an incident field

generated by a source (feed) located in the input side V^- to a desired field in the output side V^+. In V^-, the source, shown by a black circle in Figure 5.1, is placed at a distance d_1 from the input side of D, and generates an incident field $\vec{\Psi}^{\text{inc}}$ where $\Psi = \{\boldsymbol{E}, \boldsymbol{H}\}$ (i.e., Ψ refers to the set of electric and magnetic fields). In addition, there could be a reflected field from D, which is denoted by $\vec{\Psi}^{\text{ref}}$. Since the feed is known, $\vec{\Psi}^{\text{inc}}$ is known. Furthermore, in this work, we desire minimal reflections from the design domain D; thus, we assume $\vec{\Psi}^{\text{ref}} = 0$.[4]

In terms of desired data to be given to the inversion algorithm, we consider two scenarios. Let us begin by the simpler scenario where we assume that the desired complex electric and magnetic fields are specified on the first region of interest denoted by ROI_1 in Figure 5.1. The region ROI_1 is in V^+ and at a distance d_2 from the output side of D. It is here where the desired transmitted field $\vec{\Psi}^{\text{tr}}$ needs to be defined. As will be seen later, ROI_1 needs to be electrically close to the design domain D so that we can scale the desired output field to equalize the input and output powers.[5] However, in most practical applications, the designer does not know the complex fields on ROI_1; instead, the designer knows some performance criteria often located in the far-field zone. This will then bring us to the second case where only some desired far-field performance criteria are known. For example, consider the case in which we wish to convert the incident field to an output field which exhibits a certain HPBW, main beam and null directions in the far-field zone. These desired performance criteria cannot be easily represented by complex fields on ROI_1. In such situations, we take advantage of the second region of interest, denoted by ROI_2, and construct a desired power pattern on ROI_2 that meets the desired performance criteria. We will then use an inverse source algorithm (also known as a source reconstruction method) to infer the required field values on ROI_1 from the knowledge of the desired specifications on ROI_2.[6]

[4] As will be seen later, we implicitly enforce this zero reflection (matched condition) by requiring that the power going into D in the $\hat{x}$ direction to be the same as the power leaving D toward $\hat{x}$ direction. Since D is a passive domain, this will automatically favour zero reflection.

[5] For example, in our examples, d_2 has been set to 0.14λ where λ denotes the wavelength in free space.

[6] This step is similar to the inverse source algorithm used for the design of electromagnetic metasurfaces from far-field performance criteria [2, 68].

Once we have the total complex desired fields on ROI_1, we make sure that the total power of the field on the input side of D (denoted by D^-) is conserved by comparing it to the output power on ROI_1. This step is crucial for inverse scattering for design as it links the magnitude of the desired output field to the known incident field magnitude of the feed. For example, if we wish to convert a given incident field to a normalized power pattern, we would only know the relative amplitude of the fields, and not its actual values. (This is in contrast to imaging applications where the actual field values are measured, and thus are known.) Once the total power conservation is enforced, the desired scattered field on ROI_1 can be obtained and can then be given to an inverse scattering algorithm to reconstruct an appropriate passive and lossless permittivity profile in D. The next section explains each of these steps in detail.

5.3 Methodology

Herein, we utilize a three-step method to design permittivity profiles in D capable of transforming a known source incident field to a desired output field that satisfies user-defined specifications. These steps are explained in detail below. In addition, the overall procedure is shown in the form of a flowchart in Figure 5.2.

5.3.1 Step I: Specify Fields on ROI_1

In this step there are two possible scenarios depending on the type of known desired field information.

5.3.1.1 Desired complex field is known on ROI_1

In this scenario we assume that the total complex desired field (tangential electric and magnetic field) is fully defined on ROI_1 or can easily be inferred. For example, in a plane

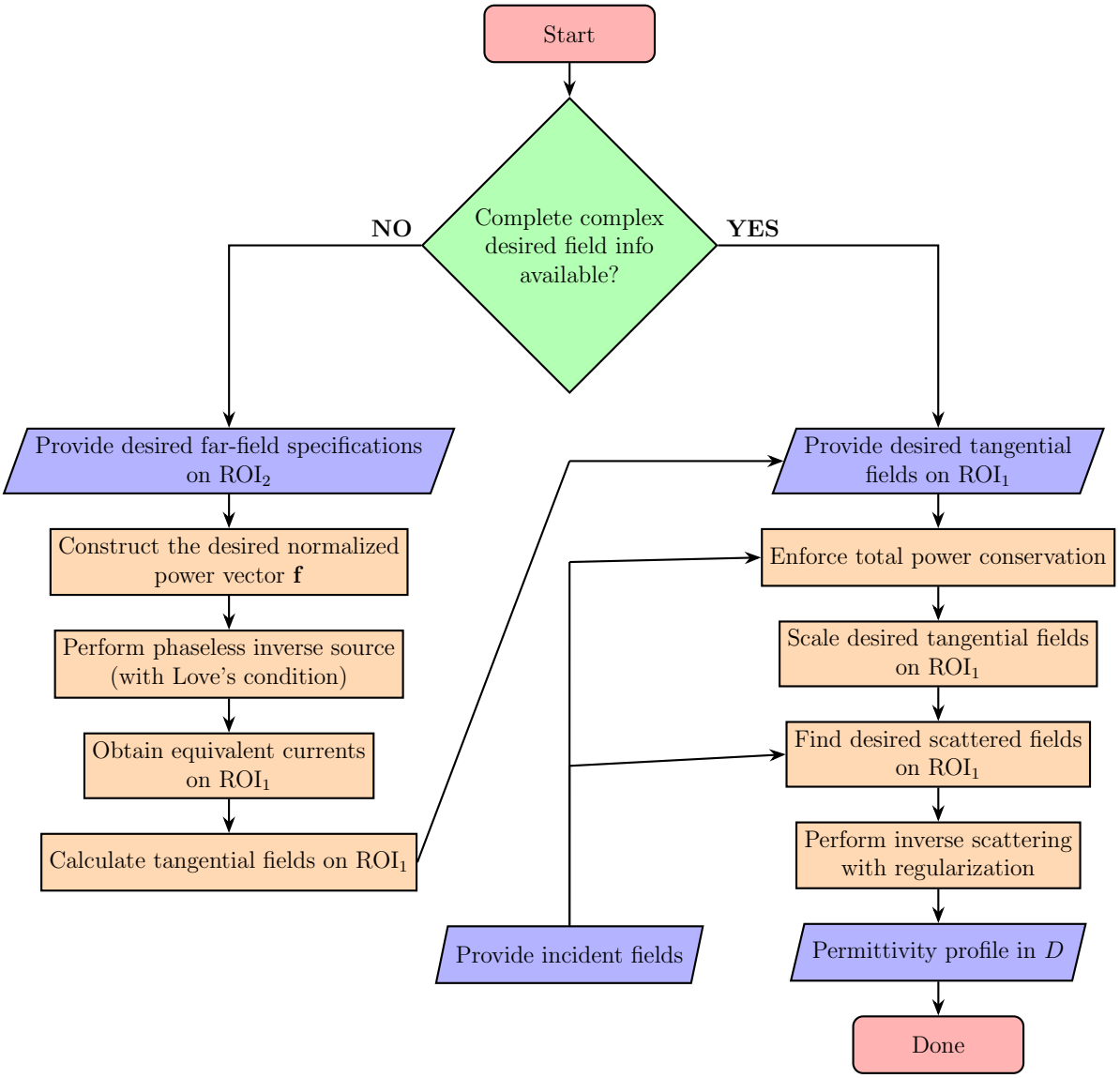

Figure 5.2: A flowchart summarizing the proposed inverse design framework presented in Section 5.3. The diamond decision box represents the two scenarios considered herein.

wave refraction design example it is easy to mathematically define the desired field on ROI_1 if one knows the intended refraction angle and the frame of reference. Or if we desire to transform the incident field emanating from a line source, which can be described with a zeroth order Hankel function of the second kind $H_0^2(\cdot)$, to a plane wave travelling in the $\hat{x}$ direction, we can simply assume that the electric field on ROI_1 is $1\angle 0^\circ$ (uniform amplitude and phase).[7] In these and similar cases, the field can already be specified in the desired form for the next step so no further action is needed. (This scenario corresponds to the right side of the diamond-shape decision box in the flowchart shown in Figure 5.2.)

5.3.1.2 Desired far-field specifications are known

If far-field specifications must be satisfied, we first perform an intermediate step to infer the associated complex field components on ROI_1 from the specifications on ROI_2, thereby transforming the given desired specifications into a form that may be used with existing inverse scattering algorithms. (This scenario corresponds to the left side of the diamond-shape decision box in the flowchart shown in Figure 5.2.) To solve for the complex tangential electric and magnetic fields on ROI_1 from far-field specifications (e.g. main beam direction, null locations, etc.) on ROI_2 we use the process outlined in [2, Section VII-C] which is briefly outlined here for completeness. First, we transform the given far-field specifications to a normalized power pattern that can be used to formulate the appropriate data misfit cost functional for the next step. To this end, we construct a real-valued vector $\mathbf{f}$ in which each element represents a desired normalized power value at a specific location. For example, main beam directions are met by setting the elements of $\mathbf{f}$ to 1 (0 dB) in the appropriate location and nulls are specified by setting the appropriate elements of $\mathbf{f}$ to a small value such as 10^{-6} (-60 dB). Also, the HPBW criterion for each main beam is met by modelling each beam as a cosine distribution and symmetrically varying the beam from 1 at the max to 0.5 (-3 dB) at the appropriate locations in $\mathbf{f}$ [2, Section VII-C].

[7] The notation $A\angle\theta^\circ$ is the phasor representation of a quantity with the magnitude of A and the phase of θ.

Once the vector $\mathbf{f}$ is constructed, we formulate an inverse source problem with the following objective: determining a set of equivalent electric and magnetic current densities on ROI_1 that can create a power pattern on ROI_2 to meet constraints set in $\mathbf{f}$. To this end, we represent the discretized equivalent electric ($\boldsymbol{J}$) and magnetic ($\boldsymbol{M}$) current densities on ROI_1 with the complex vector $\mathbf{x} = [\boldsymbol{J}; \boldsymbol{M}]$ over which we minimize the following cost functional

$$C_{\mathrm{spec}}(\mathbf{x}) = \left\| \mathbf{W} \left(|\mathbf{A}\mathbf{x}|^2 - \mathbf{f} \right) \right\|_2^2 . \tag{5.1}$$

In the above cost functional, $\|.\|_2$ denotes the L_2 norm, and $\mathbf{A}$ is an operator mapping equivalent electric and magnetic current densities $\mathbf{x}$ on ROI_1 to E_z on ROI_2. Note that since we consider TM_z, the calculation of E_z is sufficient. In addition, as described in [2, 35], this operator is augmented so as to map the electric and magnetic current densities on ROI_1 to E_z values on an inward surface with respect to ROI_1 in order to enforce Love's condition. Consequently, the vector $\mathbf{f}$ needs to be augmented by zero elements to represent null fields associated with Love's condition. Due to the enforcement of Love's condition, the equivalent currents on ROI_1 are directly related to the tangential fields on ROI_1, i.e., E_z and H_y. Finally, $\mathbf{W}$ is a diagonal weighting matrix that allows the nulls and main beams to be more evenly considered during the minimization of $C_{\mathrm{spec}}(\mathbf{x})$ [2, Section VII-C]. We then minimize $C_{\mathrm{spec}}(\mathbf{x})$ with respect to $\mathbf{x}$ on ROI_1, iteratively using a conjugate gradient method with analytically derived gradients [2, Section VII-C] thereby solving for a set of sources on ROI_1 that can produce the required far-field specifications on ROI_2. Once the equivalent currents $\mathbf{x}$ are determined, we need to convert them to equivalent electric and magnetic fields. The enforcement of Love's condition allows us to relate the current densities on ROI_1 to the tangential fields according to the following relations

$$\begin{aligned} \hat{y}\, H_y|_{\mathrm{ROI}_1} &= -\hat{x} \times \hat{z}\, J_z|_{\mathrm{ROI}_1}, \\ \hat{z}\, E_z|_{\mathrm{ROI}_1} &= \hat{x} \times \hat{y}\, M_y|_{\mathrm{ROI}_1}, \end{aligned} \tag{5.2}$$

where $H_y|_{\mathrm{ROI}_1}$ and $E_z|_{\mathrm{ROI}_1}$ are the magnetic and electric fields tangential to ROI_1, respectively. Similarly, $J_z|_{\mathrm{ROI}_1}$ and $M_y|_{\mathrm{ROI}_1}$ are the reconstructed equivalent electric and magnetic current densities on ROI_1, respectively. (Note that the vector $\mathbf{x}$ is the result of

concatenation of the discretized J_z and M_y vectors.) In addition to providing a way of relating the current densities on ROI_1 to the fields, we also enforce Love's condition as a way of reducing reflections.[8]

It should be noted that this step (to some extent) addresses the existence issue of ill-posedness that will be encountered in the inverse scattering step. If we are able to find a current distribution on ROI_1 that can satisfy the required far-field specifications, it is likely that we can design a permittivity profile in D that can produce the field distribution on ROI_1. This is because these currents are solved using full-wave physics operators and so they will be close to physical (they can not be exactly physical due to the presence of numerical error) and if these currents can satisfy the constraints on ROI_2 while being confined to ROI_1 with a size of d_4 (the same length as D) the inverse scattering algorithm should be able to find a solution. (Note that the size of ROI_1 determines the aperture size of the radiating system, thus, directly affecting the HPBW in the far-field zone.) The other item that affects the existence of the solution is the thickness of the design domain, denoted by d_3 in Figure 5.1, which will be discussed in Section 5.3.3.

Now that we have inferred the required tangential fields on ROI_1, we can move on to the next step.

5.3.2 Step II: Total Power Conservation

Once we have the tangential electric and magnetic fields on ROI_1, we ensure that the total input power going into D in V^- is approximately equal to the output power on ROI_1.[9] This is necessary to ensure that the field transformation can be done using a passive and lossless permittivity profile. In order to do this we calculate the electric and magnetic field on the input boundary of D, denoted by D^- in Figure 5.1. To this end,

[8]Note that when Love's condition is enforced when solving the inverse source problem, it favours the current density distributions that do not direct energy back toward the design domain D from ROI_1. This serves to reduce reflections towards the source.

[9]This is similar to the total power conservation used in the design of metasurface pairs or cascaded metasurfaces [99, 102].

D^- is discretized into $m = 1, 2 \cdots, M$ edges where the tangential fields on the mth edge are denoted by $E_{z,m}|_{D^-}$ and $H_{y,m}|_{D^-}$. Then, the power going into D^- in the $\hat{x}$ direction is approximated by

$$\hat{x}\, P_{\text{in}} \approx \frac{1}{2} \sum_{m=1}^{M} \left| \text{Re}\left(\hat{z}\, E_{z,m}|_{D^-} \times \hat{y}\, H^*_{y,m}|_{D^-} \right) \right| \Delta A_m \tag{5.3}$$

where Re(.) is an operator extracting the real component of a complex number and $*$ represents the complex conjugate operator. In addition, ΔA_m denotes the element area[10] at the mth edge on D^-. Note that since we are assuming a reflectionless design domain (i.e., $\Psi^{\text{ref}} = 0$), the field on D^- will be the incident field of the feed which is known.

Similarly, we can calculate the output power P_{out} leaving ROI_1 in the $\hat{x}$ direction.[11] However, note that $E_z|_{\text{ROI}_1}$ and $H_y|_{\text{ROI}_1}$ can be scaled by any number, say $\alpha \in \mathbb{R}$, and they will still satisfy the required desired specifications, such as a normalized power pattern or HPBW, on ROI_2. Therefore, in a more general form, P_{out} can be written as

$$\hat{x}\, P_{\text{out}} \approx \frac{1}{2} \sum_{m=1}^{M} \left| \text{Re}\left(\hat{z}\, \alpha E_{z,m}|_{\text{ROI}_1} \times \hat{y}\, \alpha H^*_{y,m}|_{\text{ROI}_1} \right) \right| \Delta A_m \tag{5.4}$$

where ROI_1 is discretized to $m = 1, \cdots, M$ edges. Note that so far the incident field is completely decoupled from the tangential fields on ROI_1. The way that we relate the incident field to the required tangential fields on ROI_1 is by enforcing that the input power needs to be equal to the output power, i.e., $P_{\text{in}} = P_{\text{out}}$. This results in determination of the scaling parameter α as follows

$$\alpha = \sqrt{\frac{\sum_{m=1}^{M} \left| \text{Re}\left(E_{z,m}|_{D^-}\, H^*_{y,m}|_{D^-} \right) \right|}{\sum_{m=1}^{M} \left| \text{Re}\left(E_{z,m}|_{\text{ROI}_1}\, H^*_{y,m}|_{\text{ROI}_1} \right) \right|}}. \tag{5.5}$$

[10] Due to the 2D framework assumed in this paper, this reduces to element length in the implementation.

[11] The choice of $\hat{x}$ direction (i.e., the normal direction) for comparing the input and output power levels is inspired by a similar approach in [94].

Once we have α, the desired *scattered* electric field on ROI_1 can be determined as follows

$$E_z^{\mathrm{scat,desired}}|_{\mathrm{ROI}_1} = \alpha E_z|_{\mathrm{ROI}_1} - E_z^{\mathrm{inc}}|_{\mathrm{ROI}_1}, \tag{5.6}$$

where $E_z^{\mathrm{inc}}|_{\mathrm{ROI}_1}$ is the $\hat{z}$ component of the incident electric field on ROI_1. This is the scattered field that will be used by the inverse scattering algorithm to reconstruct a dielectric profile within the design domain D. Note that since the problem is 2D TM_z, the above scattered electric field is sufficient for inverse scattering algorithms. (We note that in [80, 143], the scaling parameter has been included as an extra unknown in the iterative optimization process associated with the contrast source inversion algorithm.)

5.3.3 Step III: Perform Inverse Scattering

In the final step, we solve for the permittivity profile in the design domain D with the knowledge of the desired scattered field on ROI_1, see (5.6), and the source (incident) field. To this end we use the multiplicatively-regularized contrast source inversion (MR-CSI) [30] and multiplicatively-regularized Guass-Newton Inversion (MR-GNI) algorithms [4, 79], but other inverse scattering algorithms may also be used. Note that the major difference between the use of the inverse scattering framework for this design problem versus the imaging problem lies in the fact that in imaging we often use multiple illuminations; however, in the considered design problem, we have only one illumination. This increases the non-uniqueness of the inverse problem which is not an issue for the design problem as we need *a* solution, as opposed to the true solution. In the inverse scattering step, the main purpose is to find the dielectric profile contrast χ defined as

$$\chi(\boldsymbol{r}) \triangleq \epsilon(\boldsymbol{r}) - 1 \tag{5.7}$$

where $\boldsymbol{r}$ is the position vector spanning the design domain D, ϵ is the relative permittivity at location $\boldsymbol{r} \in D$, and the right hand side "1" denotes the relative permittivity of the background medium (air). For a predicted $\chi(\boldsymbol{r})$, let us assume that the simulated

scattered field on ROI_1 is denoted by $E_z^{\mathrm{scat,sim}}$. Inverse scattering algorithms typically attempt to iteratively minimize the discrepancy between the simulated and desired scattered fields. For example, in the case of GNI-type algorithms, they minimize the following nonlinear data misfit cost function over the unknown contrast χ

$$\left\| E_z^{\mathrm{scat,sim}}(\chi) - E_z^{\mathrm{scat,desired}} \right\|_2^2 \quad \text{subject to regularization.} \tag{5.8}$$

The augmentation of the above data misfit cost functional by a regularization term [108] projects the solution into a subspace which often limits high spatial frequency components to avoid solution instability. In addition, the use of regularization can facilitate the physical implementation of the object in D. Herein we use the following forms of regularization.

- The weighted L_2 norm total variation regularization scheme: this regularizer attempts to preserve the edges of permittivity profiles in D, and also has smoothing effects [30] that can lead to permittivity profiles that are easier to physically implement. Because this regularization scheme does not assume any prior information about the dielectric profile in D, we refer to this as 'blind' regularization.

- The expected permittivity regularization: this regularizer assumes knowledge of a finite set of permittivity values that are present in D, and tries to place these values in D at the correct locations to achieve the scattered fields [32, 40, 41]. This regularizer is especially helpful for design, as one can specify the permittivity values they have access to for physical implementation. In this paper, we show an example wherein we utilize the binary MR-GNI or BMR-GNI algorithm [32] that favours only two permittivity values, one of which will be air. Therefore, if a designer has access to nylon ($\epsilon = 3$), the BMR-GNI algorithm favours two permittivity *contrast* values: 0 (air) and 2 (nylon).

The way that these regularization schemes work is (partly)[12] through the modification of the gradient of the cost functional. For example, in the case of the BMR-GNI where we favour the contrast value of χ^h, the gradient of the cost functional will be additively augmented by $(\chi - \chi^h)$ (with an appropriate weight) [32], thus, aiming to bring the contrast value χ closer to the preferred contrast value χ^h.

In addition to what was noted in Section 5.3.2 (aperture size), the other item that affect the existence of the solution is the thickness of the design domain, denoted by d_3 in Figure 5.1. In fact, the incident field needs to go through sufficient electrical length to be able to tailor itself to the desired field on ROI_1. From our numerical experience, we have found that if d_3 is smaller, the inverse scattering algorithm tends to reconstruct higher dielectric values to increase the electrical length (i.e., d_3/λ) of the system.[13] Finally, note that we do *not* explicitly enforce the reflections from the design domain D to be zero. However, as will be shown in Section 5.4, these reflections are in fact very small. This is due to the fact that the enforcement of total power conservation between the input and output sides of D implicitly enforces the reflections to be small.

5.4 Results

Herein, we implement the aforementioned inverse design methodology for two scenarios. In the first scenario, we design a dielectric profile that can transform the electric field of a line source to a plane wave. In this transformation, the desired complex field is known on ROI_1, and therefore we do not solve an inverse source problem. In the second scenario, we solve for a dielectric profile in D that can transform the electric field of a line source

[12]The other aspect of regularization schemes is the choice of the regularization weight. That is, the relative weight between the gradient of the data misfit cost functional and that of the regularization term. This is done in an automatic fashion in multiplicative regularization. (Also, note that in addition to modifying the gradient vector, the regularization scheme modifies the Hessian matrix in the GNI algorithm.)

[13]Note that if d_3 goes to zero, we enter the realm of metasurfaces, which are described by surface electric, magnetic, and magneto-electric susceptibilities [6, 148]. However, herein, we only rely on a permittivity profile which is related to volumetric electric susceptibility.

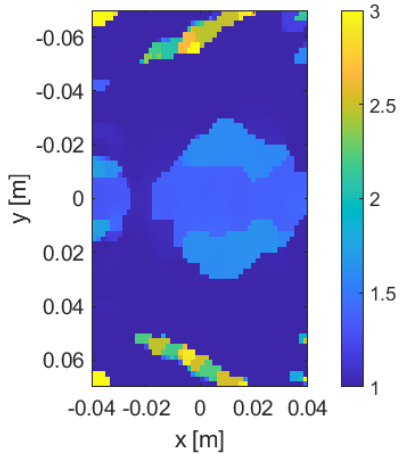

(a) Relative permittivity

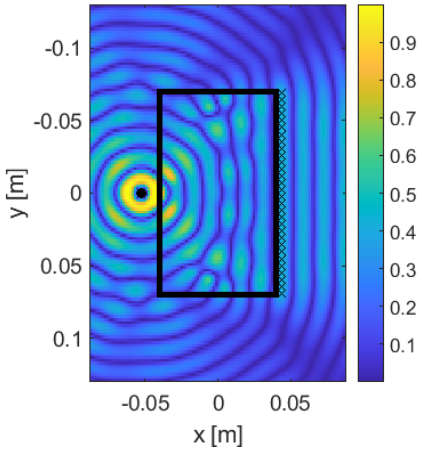

(b) $|E_z|$ at a fixed phase (V/m)

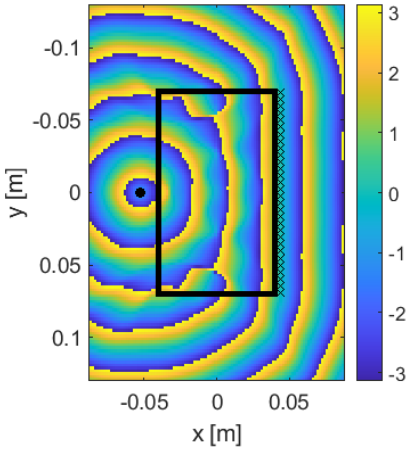

(c) Phase of E_z (radians)

Figure 5.3: Near-field results for a line source to plane wave transformation example under blind inversion are shown. The designed permittivity profile in the design domain D is shown in (a), the electric field magnitude ($|E_z|$) is shown in (b), and the phase of E_z is shown in (c). In (b) and (c) the black border represents the design domain D, the black dot represents the position of the line source, and the crosses represent the position of ROI_1. The MR-CSI algorithm was used in the inverse scattering design step and the frequency of operation was 10.5 GHz.

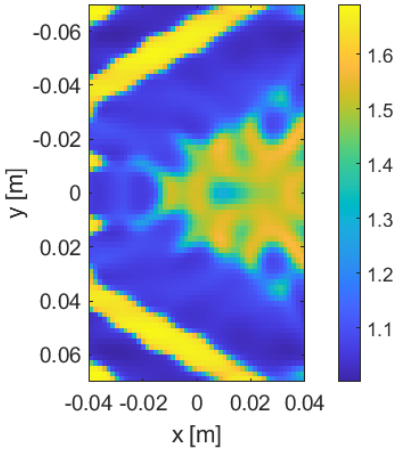

(a) Relative permittivity

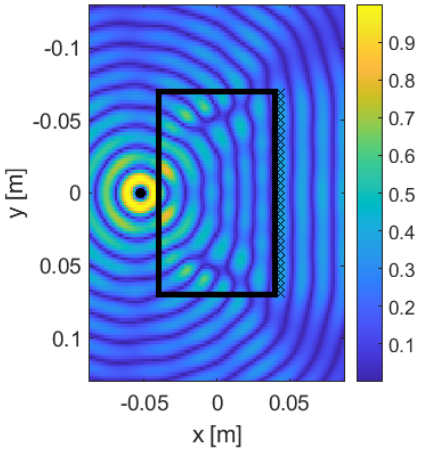

(b) $|E_z|$ at a fixed phase (V/m)

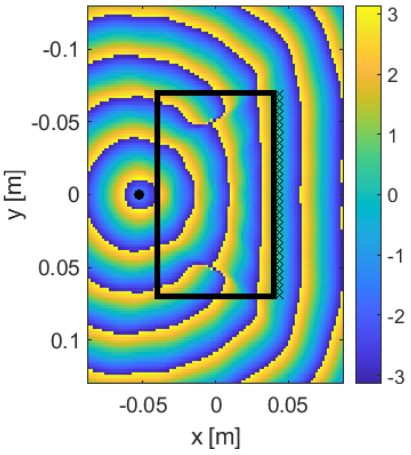

(c) Phase of E_z (radians)

Figure 5.4: Near-field results for a line source to plane wave transformation example under binary inversion are shown. The designed permittivity profile in the design domain D is shown in (a), the electric field magnitude ($|E_z|$) is shown in (b), and the phase of E_z is shown in (c). In (b) and (c) the black border represents the design domain D, the black dot represents the position of the line source, and the crosses represent the position of ROI_1. The BMR-GNI algorithm was used in the inverse scattering design step and the frequency of operation was 10.5 GHz. The expected permittivity values that were used were $\epsilon_r = 1.7$ and $\epsilon_r = 1$ (background).

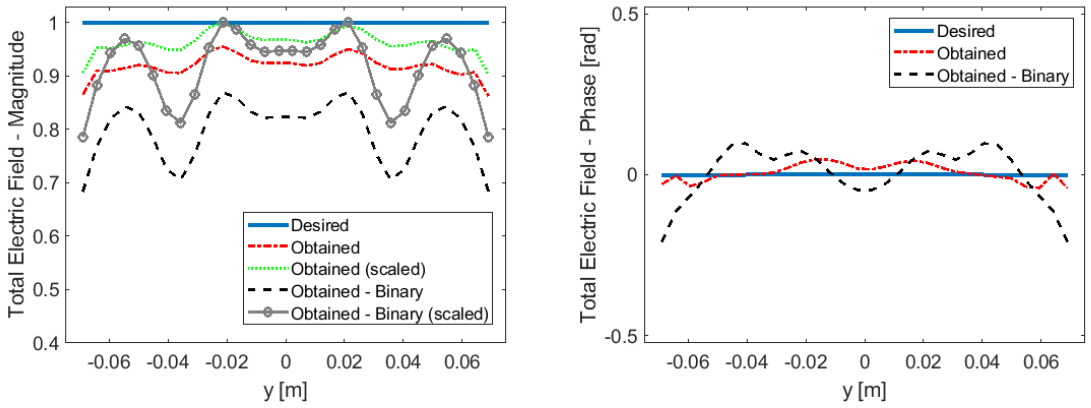

(a) (b)

Figure 5.5: The electric field E_z magnitude (a) and phase (b) are shown on ROI_1 for the line source to plane wave transformation example using the MR-CSI and BMR-GNI inverse scattering algorithms at a frequency of 10.5 GHz. The desired field corresponds to the desired E_z magnitude and phase needed on ROI_1 to achieve a normally incident plane wave. The obtained field corresponds to the E_z achieved by illuminating the designed permittivity profile shown in Figure 5.3(a) (Obtained) and Figure 5.4(a) (Obtained - Binary). The obtained magnitude plots were also scaled by a real scalar value to increase the maximum magnitude of E_z to one to allow for a more meaningful comparison with the desired magnitude distribution.

to achieve a set of desired far-field specifications. To this end, we define the far-field specifications on ROI_2 and we solve an inverse source problem to calculate the tangential fields on ROI_1 before proceeding with the total power conservation and inverse scattering steps.

For all these examples, the frequency of operation is at 10.5 GHz. The design domain D is a rectangle of the size 8×14 cm^2 which is *approximately* $3\lambda \times 5\lambda$ where λ denotes the wavelength in air. The design domain is then discretized into 50×70 cells. All the blind inversion is done by the MR-CSI algorithm where the number of iterations has been set to 3024.[14] For the case of binary reconstruction, we have used the BMR-GNI algorithm. In addition, in all the cases considered, the transmitter (line source) is placed at (x, y) equal to $(-5.2, 0)$ cm. That is, in Figure 5.1, $d_1 = -1.2$ cm, which is 0.42λ. In addition,

[14]The number of iterations has been chosen in an ad-hoc manner.

for all the cases, ROI_1 is the vertical line $x = 4.4$ cm. In other words, $d_2 \approx 0.14\lambda$ in Figure 5.1. On ROI_1, we consider 30 equally-spaced data points. Given that the length of the ROI_1 is about 5λ, the separation between the data points on ROI_1 is about $\lambda/6$.

Furthermore, note that the reconstructed permittivity is, in general, complex. Since we desire a lossless dielectric profile, we enforce the imaginary part of ϵ to be zero at each iteration of the inverse scattering algorithm.[15] In addition, since we would like to use practical dielectric values, we enforce the minimum of the real part of ϵ to be one and the maximum to be three at each iteration of the inverse scattering algorithm.

5.4.1 Line source to plane wave transformation

In this example, the objective is to find a lossless relative permittivity profile in D to transform the electric field emitted by a line source (cylindrical waves) to a plane wave propagating along the $\hat{x}$ direction. Since the electric field of a plane wave (uniform amplitude, phase, and polarization) is analytically known, we assign E_z on ROI_1 to be $1\angle 0°$. Next we utilize the parameter α to ensure that the input and output powers are equal. Having found α, the desired total electric field E_z on ROI_1 will then be $\alpha\angle 0°$. Knowing the incident field (line source), we can determine the desired *scattered* field on ROI_1 which can then be given to the inverse scattering algorithm for inversion.

In the first set of results, the inverse scattering method utilized to invert the data on ROI_1 was MR-CSI. Note that this algorithm makes use of the multiplicative L_2 norm total variation regularizer to influence the permittivity profile solution in D to be easier to fabricate, and to regularize the inverse problem. Figure 5.3(a) shows the reconstructed dielectric profile in D. As can be seen, we have an inhomogeneous relative permittivity

[15] We are also implicitly enforcing a lossless medium via applying total power conservation.

profile ranging from one to three.[16] Figure 5.3(b) shows the normalized magnitude of E_z in the near-field in and around D where D has been identified by a black rectangle and the source by a black circle on the left side of D.[17] It is worthwhile to note that the domain D is almost reflectionless and has not perturbed the cylindrical waves on D^-. In addition, on the right side of D, we see that E_z forms a planar wavefront. The small crosses just outside and on the right side of D marks the discretized locations on ROI_1 on which we have enforced the desired scattered field. It can be observed that the generated planar wavefront is approximately the size of the ROI_1 which is partly related to the size of ROI_1. Similarly, Figure 5.3(c) shows the phase of E_z in the near-field in and around D where the design domain D has been again shown by a black rectangle, and the source is identified by a black circle located just to the left of D. As can be seen, the phase distribution is close to uniform as the waves arrive at ROI_1 shown by small black crosses just to the right of D. The permittivity profile successfully achieves the desired transformation.

Next, in order to achieve the same transformation we use a binary inversion algorithm (BMR-GNI) where a multiplicative expected permittivity regularizer as in [32, 40] is used to regularize the data misfit cost functional. Through the use of the expected permittivity regularizer, we favour two relative permittivity values in D: $\epsilon_r = 1.7$ and $\epsilon_r = 1$ (air/background). This can further facilitate fabrication as the designer can choose the permittivity values they have available and there is only one other permittivity value in the profile other than the background (air). The reconstructed permittivity profile for this case is shown in Figure 5.4(a). By looking at this figure, it can be seen that the inverse scattering algorithm favoured a permittivity profile with the previously specified

[16]Note that the practical implementation of a lens, for example via 3D printing, would involve some level of permittivity value discretization. We expect that the performance of the lens degrades after such post-processing. This is especially the case for continuously varying profiles relative to the profiles designed using expected permittivity regularization. We speculate that the amount of degradation would depend on the level of discretization and the range of the required relative permittivity values actually covered by the available materials, but this requires further study.

[17]Note that in the absence of the dielectric object we only have the fields of the line source which are in the form of cylindrical waves. Since the dielectric lens is (almost) reflectionless these cylindrical waves are still visible on the input side of the dielectric lens. However, as can be seen in Figure 5.3(b), once the input field enters the dielectric lens, it is tailored to become a truncated plane wave.

values.[18] Also, comparing the reconstructed dielectric profile in Figure 5.4(a) with that in Figure 5.3(a) clearly demonstrates the non-uniqueness of this inverse scattering problem. Then looking at the normalized magnitude and phase of E_z in Figure 5.4(b)-(c), we can see that the profile in D appears to be able to transform the line source electric field to a plane wave despite its relative simplicity compared to the previous example when a continuous set of relative permittivity values were allowed in D.

To show the difference between the two line source transformation examples in more detail, Figures 5.5(a)-(b) show the magnitude and phase of the desired and obtained E_z on ROI_1 for both the binary and blind inverse scattering cases. Let us first focus on Figure 5.5(a) where we can compare the *desired* normalized magnitude (i.e. a flat blue line of magnitude one) with what has been *obtained* from the blind inversion (red dash-dot curve) and the binary inversion (black dashed curve). As can be seen, the magnitude distribution that was obtained in the blind inversion is closer to an ideal plane wave than the binary case. This is expected as the blind inverse scattering algorithm has a wide range of permittivity values to choose from, whereas the binary case sacrifices degrees of freedom to facilitate physical implementation.

Note that in both cases (blind and binary inversion cases), the magnitude of E_z on ROI_1 is below the desired level. This is an indication of power loss in the transformation. Since the reconstructed permittivity is lossless, this power loss cannot be attributed to the loss within the dielectric materials. The other source of power loss is through reflections at the interface of D^-. However, as can be seen in Figure 5.3(b) and Figure 5.4(b), there is minimal reflected energy. The major source of power *loss* between D^- and ROI_1 is the power that escapes through the top and bottom edges of the design domain D. This is visible in Figure 5.3(b) and Figure 5.4(b) and (its interference with the desired radiation) can be practically reduced by placing absorbers along the top and bottom sides

[18]Note that the binary inversion performed herein may be considered soft regularization as the inversion algorithm is not forced to choose between only two values. That's why the final reconstruction has permittivity values other than $\epsilon_r = 1.7$ and $\epsilon_r = 1$. As post-processing one may convert this reconstruction to a perfect binary image for the ease of fabrication. Although not investigated here, it is expected that the performance will degrade after such post-processing.

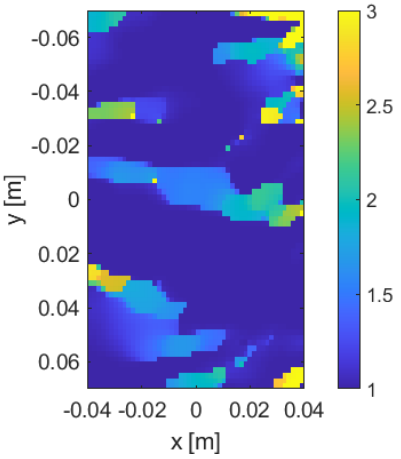

(a) Relative permittivity

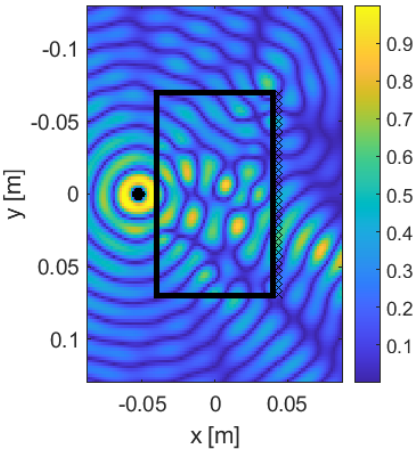

(b) $|E_z|$ at a fixed phase (V/m)

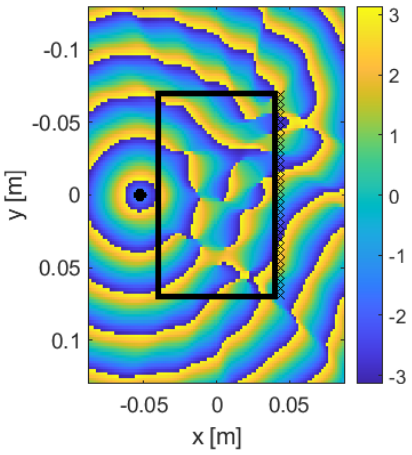

(c) Phase of E_z (radians)

Figure 5.6: Near-field results for a far-field (single) beam forming example described in Section 5.4.2.1 is shown. The designed permittivity profile in the design domain D is shown in (a), the electric field magnitude ($|E_z|$) is shown in (b), and the phase of E_z is shown in (c). In (b) and (c) the black border represents the design domain D, the black dot represents the position of the line source, and the crosses represent the position of ROI_1. The MR-CSI algorithm was used in the inverse scattering design step and the frequency of operation was 10.5 GHz.

of D.[19] Now that we understand why there are differences in scale between the obtained magnitude of E_z on ROI_1 and the desired magnitude, we can scale the obtained and desired electric fields so their maximums are equal to better compare the shapes of the

[19]In addition to this method of suppressing unwanted radiation, we may also increase the size of d_4 of ROI_1 to create a larger area where we can control the output field.

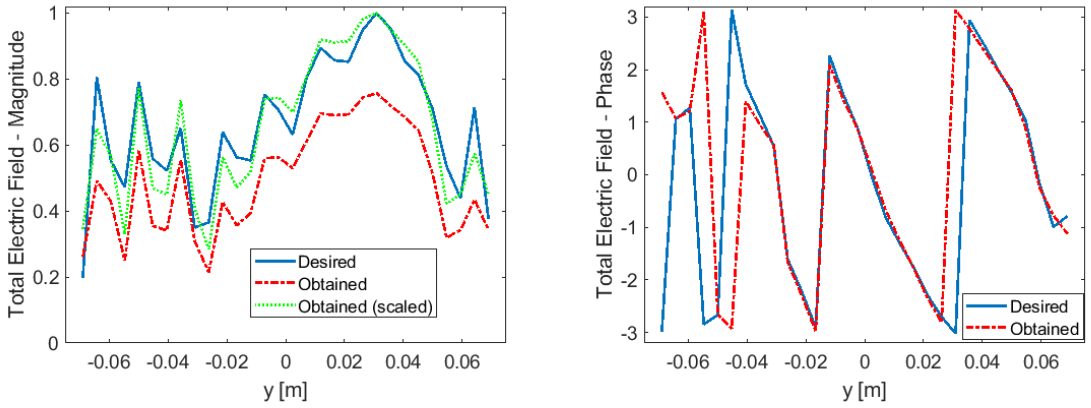

(a) (b)

Figure 5.7: The electric field E_z magnitude (a) and phase (b) are shown on ROI_1 for the beam forming example described in Section 5.4.2.1 using the MR-CSI inverse scattering algorithm at a frequency of 10.5 GHz. The desired field corresponds to the desired E_z magnitude and phase needed on ROI_1 to achieve the desired far-field specifications. The obtained field corresponds to the E_z achieved by illuminating the designed permittivity profile shown in Figure 5.6(a). The obtained magnitude plot was also scaled by a real scalar value to increase the maximum magnitude of E_z to one to allow for a more meaningful comparison with the desired magnitude distribution.

obtained and desired magnitude curves. These scaled curves are shown in Figure 5.5(a). In particular, the variation of the scaled version of obtained E_z for the blind inversion is $0.9 < |E_z|_{\text{ROI}_1} \leq 1$, which is reasonable. In addition, we can see the phase data on ROI_1 in Figure 5.5(b) where the desired phase ($\angle 0°$) is flat line, and the obtained phase under the blind inversion is very close to the desired phase. On the other hand, the obtained phase from the binary inversion shows more variance as we have significantly limited the degrees of freedom. Note that the plots of the scaled version are not present in the phase data as our scaling factor is a real number and therefore does not change the phase data.[20]

[20]According to [149, Ch. 4], the region of pseudo plane wave, known as the quiet zone in far-field antenna ranges, requires peak-to-peak variations of magnitude and phase to not exceed ± 0.5 dB and $\pm 5°$ respectively. The reconstruction using the blind inversion has the absolute maximum variations of 0.9 dB and 5.1° phase, and thus satisfies the above criteria. On the other hand, the binary inversion has the absolute maximum variation of 2.1 dB and 17.55° and thus does not satisfy the above criteria.

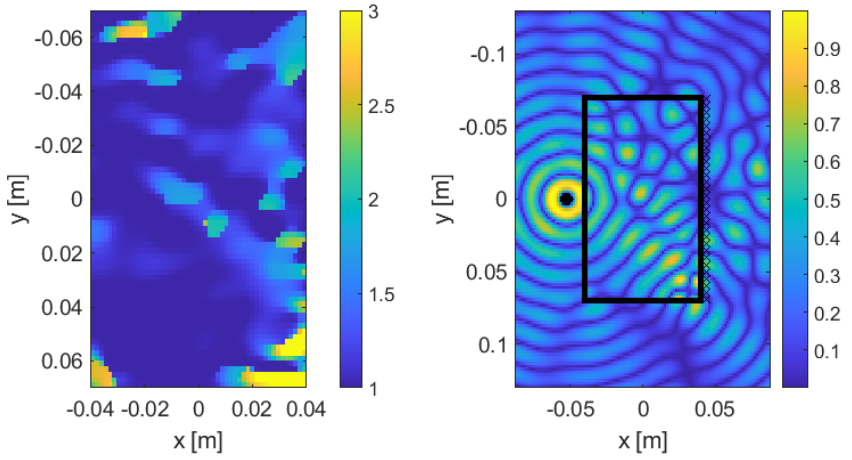

(a) Relative permittivity

(b) $|E_z|$ at a fixed phase (V/m)

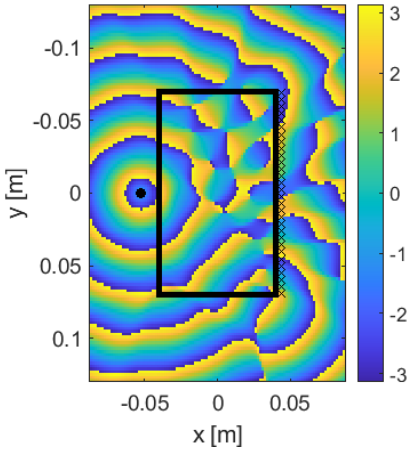

(c) Phase of E_z (radians)

Figure 5.8: Near-field results for a far-field (double) beam forming described in Section 5.4.2.2 are shown. The first beam is required to be in the $\varphi = -50°$ direction with a HPBW of 50° and nulls at $\varphi = -85°$ and $\varphi = -15°$. The second is required to be at $\varphi = 25°$, with a HPBW of 30° with nulls at $\varphi = 0°$ and $\varphi = 50°$. The designed permittivity profile in the design domain D is shown in (a), the electric field magnitude ($|E_z|$) is shown in (b), and the phase of E_z is shown in (c). In (b) and (c) the black border represents the design domain D, the black dot represents the position of the line source, and the crosses represent the position of ROI_1. The MR-CSI algorithm was used in the inverse scattering design step and the frequency of operation was 10.5 GHz.

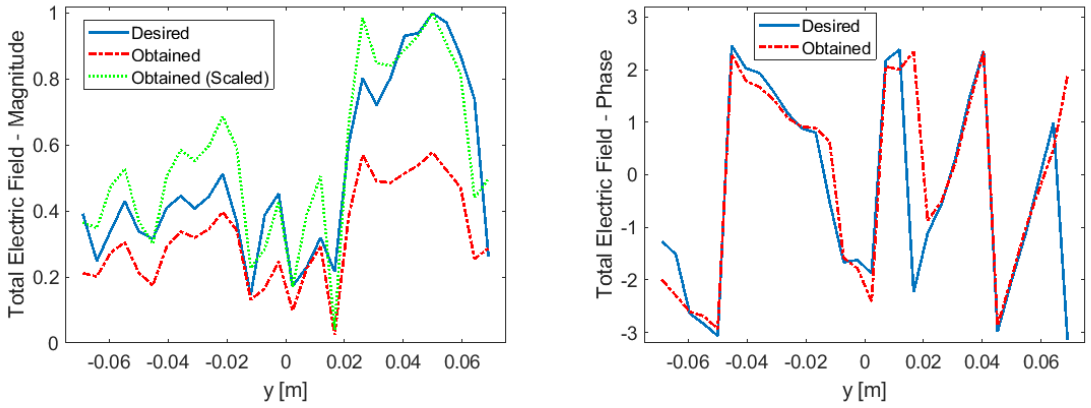

(a) (b)

Figure 5.9: The electric field E_z magnitude (a) and phase (b) are shown on ROI_1 for the beam forming example described in Section 5.4.2.2 using the MR-CSI inverse scattering algorithm at a frequency of 10.5 GHz. The desired field corresponds to the desired E_z magnitude and phase needed on ROI_1 to achieve the desired far-field specifications. The obtained field corresponds to the E_z achieved by illuminating the designed permittivity profile shown in Figure 5.8(a). The obtained magnitude plot was also scaled by a real scalar value to increase the maximum magnitude of E_z to one to allow for a more meaningful comparison with the desired magnitude distribution.

5.4.2 Far-field specifications

In this section we present examples where the goal is to design a permittivity profile in D to meet desired far-field specifications. Specifically, a main beam direction, HPBW, and null locations are known in the far-field (i.e. on ROI_2). We first solve an inverse source problem to calculate the complex tangential fields on ROI_1. Next, after the power equalization step, we use the MR-CSI algorithm[21] with L_2 norm total variation regularization to solve for the permittivity profile in D. Note that since we are considering the 2D TM_z problem with the design domain in the xy plane, we are working on $\theta = 90°$ plane, and the angular dependency of patterns will be in terms of the azimuth angle φ.

[21]For these cases, the binary inversion was not successful, and therefore is not shown.

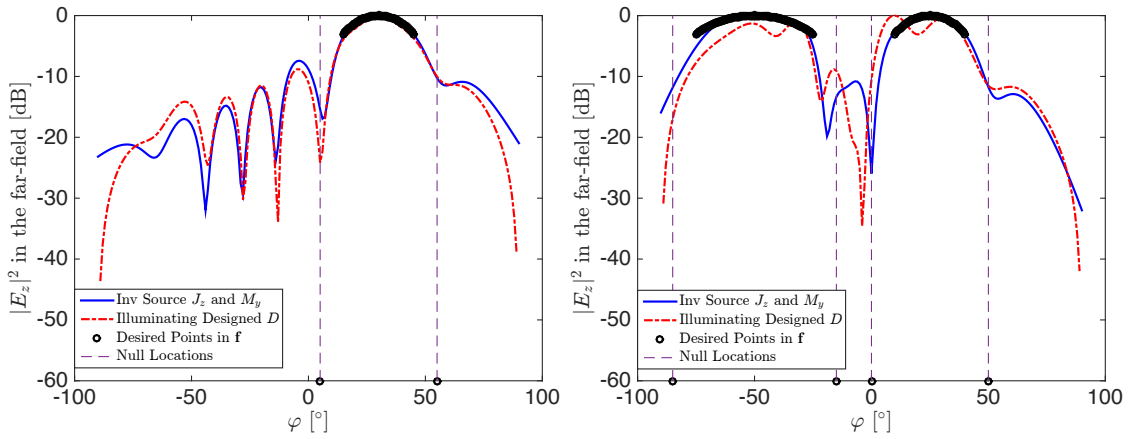

(a) (b)

Figure 5.10: The far-field power patterns are shown for the far-field single beam example described in Section 5.4.2.1 (a) and the far-field double beam example described in Section 5.4.2.2 (b). The far-field from the reconstructed electric and magnetic current densities on ROI_1 after the inverse source step (blue solid line). This inverse source step tries to match the desired far-field specifications by first translating the specifications into desired far-field points (black circle markers) in a normalized power vector $\mathbf{f}$ and then minimizing the appropriate data-misfit cost functional with respect to electric and magnetic current densities on ROI_1 (see Section 5.3.1). Finally, the far-field from illuminating the designed permittivity profile in D after the inverse scattering step, measuring the resulting fields on ROI_1, and then propagating these near-fields to the far-field is shown (red dash-dot line).

5.4.2.1 Single main beam

In this example we desire a main beam at $\varphi_{\text{main}} = 30°$ and a HPBW of $\Delta\varphi|_{\text{3dB}} = 30°$. In addition we require nulls at $\varphi_{\text{null1}} = 55°$ and $\varphi_{\text{null2}} = 5°$. Note that these are performance criteria and not explicit field values. The lossless relative permittivity profile calculated by the inverse scattering algorithm (MR-CSI) is shown in Figure 5.6(a). The normalized magnitude and phase of E_z around and within the design domain D are shown in Figures 5.6(b) and 5.6(c) respectively. Similar to the line source to plane wave transformation example, the amount of reflected energy is low. In Figure 5.7(a)-(b) the magnitude and phase of the desired and obtained E_z on ROI_1 (near-field zone) is shown. There is again unwanted power dispersion from the the top and bottom sides of D that can be seen in Figure 5.6(b). Because our final objective is to satisfy the aforementioned

performance criteria in the far-field zone, the shape of the magnitude distribution of E_z on ROI_1 must match the desired magnitude curve closely. For this reason, we have also shown the scaled version of the obtained E_z on ROI_1 in Figure 5.7(a). (We scale E_z by a real number so the maximum of the obtained $|E_z|$ is one.) As can be seen, the scaled version of the obtained $|E_z|$ is relatively close to the desired one. Similarly, the desired and obtained phase of E_z on ROI_1 are reasonably close. In summary, since the obtained and desired $|E_z|\angle E_z$ are relatively close on ROI_1, we expect to be able to satisfy our far-field performance criteria.

To this end, the far-field pattern obtained when the reconstructed dielectric profile is interrogated by the line source is required. To calculate the far-field we use the obtained fields on the ROI_1, which is defined on an edge that is at $x = 4.4$ cm and spans from $-7 < y < 7$ [cm]. The fields along the ROI_1 (i.e., along $x = 4.4$ cm) and spanning $|y| \geq 7$ [cm] are assumed to be zero. Using this assumption, we can calculate the far-field pattern simply by propagating $2M_y$ values along ROI_1 to the far-field; i.e., we are using the electromagnetic equivalence principle and the assumption that there is a perfect electric conductor behind the ROI_1. Figure 5.10(a) shows three different curves. The black circle markers show the enforcement of the desired performance criteria, which later on form the desired normalized power vector $\mathbf{f}$. For example, the two black circles at -60 dB level indicate the two desired nulls at $\varphi_{\text{null1}} = 55^\circ$ and $\varphi_{\text{null2}} = 5^\circ$. Note that this means we could have a main beam with the maximum magnitude of 1, and desired null levels set to 10^{-6} in the vector $\mathbf{f}$. This wide dynamic range of 1 to 10^{-6} shows the importance of the weighting matrix $\mathbf{W}$ in (5.1).

As noted before in Section 5.3, our first step is to reconstruct a set of equivalent currents on ROI_1 (see the unknown vector $\mathbf{x}$ in (5.1)) that can meet the far-field constraints on ROI_2. It is instructive to check the far-field pattern of these equivalent currents. This is shown in Figure 5.10(a) with a blue solid line. The main beam is quite accurate; however, although we see some nulls at 5° and 55°, they are not as deep as we have

desired (-60 dB).[22] Lastly, once we transform the near-field data that we have obtained after illumination of the reconstructed dielectric profile to the far-field zone, we get the radiation pattern shown by the red dash-dot line. As can be seen, this curve satisfies the main beam direction and null locations. However, the null levels are not as deep as originally desired and the obtained HPBW is $\Delta\varphi|_{\text{3dB}} = 26^\circ$ instead of the required $\Delta\varphi|_{\text{3dB}} = 30^\circ$ (this level of accuracy may be appropriate for many applications).

5.4.2.2 Two main beams

In this example, we desire two separate main beams in the far-field zone. The first beam is required to be in the $\varphi|_{\text{main}} = -50^\circ$ direction with a HPBW of $\Delta\varphi|_{\text{3dB}} = 50^\circ$ and nulls at $\varphi|_{\text{null1}} = -85^\circ$ and $\varphi|_{\text{null2}} = -15^\circ$. The second beam is required to be at $\varphi|_{\text{main}} = 25^\circ$, with a HPBW of $\Delta\varphi|_{\text{3dB}} = 30^\circ$ with nulls at $\varphi_{\text{null1}} = 0^\circ$ and $\varphi_{\text{null2}} = 50^\circ$. Note that in this example, there are more performance criteria than the previous example, but we maintain the same amount of unknowns in D and the same amount of sampling on ROI_1.

Figure 5.8(a) shows the reconstructed relative permittivity profile. The normalized magnitude and phase of E_z within and around the near field of D (shown as a black rectangle) are shown in Figure 5.8(b)-(c). As can be seen by looking at the left side of the design domain (i.e, D^-), the design domain is still almost reflectionless. Similar to what we did in the previous single beam example, let us now compare the desired and obtained fields on ROI_1 in Figure 5.9(a)-(b): the obtained electric field magnitude and phase distributions on ROI_1 follow the same shape as the desired magnitude and phase, but less so than the previous example. Specifically, the magnitude curve is not as accurate in this example when compared with the what was obtained in Figure 5.7(a). This is an indication that we were not able to construct a permittivity profile in D that can produce the required far-field when illuminated by our line source. The far-field results, shown in Figure 5.10(b), which were obtained in the same way as the previous example support

[22] It is instructive to note that we do not know whether it is possible to meet the null level of -60 dB along with the other performance criteria with any set of equivalent currents on ROI_1, i.e. there may not be enough degrees of freedom.

this theory. The two main beam shapes are present in the intended direction, but there are imperfections within the beams. The nulls are present, but their locations are shifted more than the previous example. Also, similar to the previous example, the nulls are not as deep as the desired level. One way we might go about improving this result is to increase the size of D to perhaps gain more degrees of freedom to produce the required electric field magnitude and phase on ROI_1.

5.5 Conclusion

We presented an inverse design framework that is capable of constructing lossless permittivity profiles that can achieve far-field and near-field transformations when illuminated with a single source/feed. This design methodology can achieve far-field specifications including main beam direction, null location, and HPBW. This framework utilizes existing gradient-based inverse scattering algorithms that have been primarily used for microwave imaging applications. However, this inverse scattering process requires two extra steps: (i) the use of an inverse source algorithm to convert desired performance criteria to equivalent currents in close proximity to the design domain, and (ii) ensuring total power conservation between the input and output power levels. In addition, the latter step implicitly favours the reconstruction of reflectionless lossless dielectric profiles within the design domain.

Herein, we utilized this inversion method to design permittivity profiles that are capable of transforming the electric field from a line source to a plane wave, and meeting two different sets of far-field specifications. Furthermore it was shown that this method cannot always meet all the desired far-field specifications and may require more degrees of freedom to do so. It was also demonstrated that different forms of regularization such as the weighted L_2 norm total variation regularization and expected permittivity regularization can be used to reconstruct different dielectric profiles for the same transformation, thus, benefiting from the non-uniqueness of the problem.

Chapter 6

Conclusions and Suggested Future Work

6.1 Conclusion

The purpose of this thesis was to improve upon and develop new antenna characterization and design techniques by utilizing the EI framework. In Chapter 1, it was explained how the current distribution of an antenna is its fundamental spatial property. We then explained that in many cases, equivalent currents may be used instead of the true internal currents of a radiator. Next, we introduced the Electromagnetic Surface and Volume Equivalence Principles; it was explained that EI algorithms use these principles for antenna design and characterization applications. Following this, we outlined our common EI methodology that we used to contribute to EI algorithms in different antenna design and characterization applications. In Chapter 2 we presented a brief overview of the antenna design and characterization applications contributed to by this work, while explaining how they are unified in their need/use of equivalent currents. This chapter also served to explain why the applications of metasurface design, microwave imaging, and

dielectric lens/antenna design were chosen for this thesis. Next, in Chapter 3 we used the surface equivalence principle to contribute to the area of metasurface design wherein we developed a novel gradient-based EI metasurface design algorithm that is capable of designing the circuit admittance profile of a three admittance layer metasurface from desired magnetic field data. We showed that our method could meet the magnitude and phase constraints in the desired data. To be able to characterize and design radiators of a larger cross-section, we then turned to the volume equivalence principle. To this end, we indirectly used this principle in Chapter 4 to contribute to the area of dielectric scatterer characterization through the context of microwave imaging. Specifically, a phaseless Gauss-Newton inversion algorithm was developed to reconstruct a dielectric profile (the unknown scatter) in a region of interest from a set of phaseless measured electric field data. Finally, to apply these principles to the design of dielectric lenses/antennas, we introduced a combined inverse source and scattering technique for the purpose of tailoring electromagnetic fields in Chapter 5. This technique is capable of designing passive, lossless, and reflectionless dielectric scatterers from complex, phaseless, or far-field criteria data. In summary, we showed that EI framework's flexibility allows for the design and characterization of antennas in many applications. This can be helpful in our ever expanding wireless technology landscape. The main contributions that resulted from this work are summarized in the next section.

6.1.1 Summary of Main Contributions

- **Metasurface Design Algorithm:** In Chapter 3, a novel gradient-based metasurface design algorithm was developed that can directly calculate the required circuit admittance profile needed to implement a passive lossless three admittance layer metasurface using complex or phaseless desired field data. To this end, we constrain the algorithm to reconstruct only purely-imaginary admittances necessitating a metasurface design without loss or gain, and local power conservation is

inherently enforced in contrast to previous work that may enforce this with additive regularization. In addition, the ability to reconstruct the circuit admittances directly enables constraints to be placed, which could not be done previously.

- **Antenna Characterization/Microwave Imaging Algorithm:** In Chapter 4, a novel phaseless multiplicatively-regularized Gauss-Newton inversion imaging algorithm was developed and verified with synthetic and experimental data. The flexibility of the EI framework was used to be able to make use of phaseless electric field data with a GNI algorithm, instead of complex measured data. It was demonstrated that more regularization is necessary to overcome the lack of phase information in the measured data for some imaging experiments.

- **Dielectric Lens/Antenna Design Algorithm:** In Chapter 5, a new combined inverse source and scattering methodology has been presented that is capable of designing dielectric profiles that when illuminated by a single feed can satisfy user specified far-field performance criteria, including main beam direction, null locations, and half-power beam width (HPBW). In addition, the technique is capable of designing, passive, lossless, and reflectionless dielectric profiles. The presented framework is also capable of using existing inverse scattering algorithms that are used for microwave imaging without much modification.

6.2 Suggested Future Work

This work can be extended in several ways. Herein, avenues for extending the work specifically for certain algorithms, and for all the algorithms in general.

- **Metasurface Design Algorithm:** This EI algorithm can design metasurfaces to meet complex and phaseless desired data. To increase its utility, it could extended to meet desired far-field criteria such as main beam direction, HPBW and null location. Furthermore, this algorithm introduced the ability to apply constraints

to the admittance profile that define the metasurface directly, and an example was shown where the admittance profile of the metasurface was smoothed within each layer. However, there may be cases where there are maximum and minimum limits to the admittances that can be physically implemented. To this end, a regularizer can be developed to take this type of constraint into account. In this work passive, lossless, reflectionless metasurfaces were being sought to match the magnitude and phase of the desired magnetic field pattern. As can be seen from the results in Chapter 3, an *ideal* solution could not be found that completely met all the constraints (magnitude, phase, and full efficiency). Therefore, a means of determining what the best possible solution is/can be should be explored.

- **Antenna Characterization/Microwave Imaging Algorithm:** It was demonstrated that regularization methods were important in supplementing the magnitude only information in some scenarios while using the developed phaseless GNI algorithms for MWI. Further research could be conducted on what the *best* possible reconstruction could be based on a set of phaseless measurements. For example, in Section 4.5.4 it was shown that there was little information content in the measured phaseless total field data as it was very similar to the phaseless incident field. It would be instructive to know what the most accurate reconstruction could be in these types of scenarios. This could also help determine how much regularization is needed to achieve a reconstruction to a desired accuracy.

  Additionally, in this work, we are able to characterize dielectric scatterers, but we could extend this to include metallic/perfect electric conductor scatterers as well. This would allow the characterization of more types of devices, including electronics. Being able to work with metals and dielectrics may also facilitate design.

- **Dielectric Lens/Antenna Design Algorithm:** The presented technique was developed to design passive, lossless, and reflectionless dielectric profiles to tailor electromagnetic fields, however, there may be cases where a specific reflected field is desired. To this end, it can be investigated how a dielectric profile could be designed if a desired transmitted and reflected field are required.

- **General:** These algorithms make use of additive and multiplicative regularization terms, and therefore, multi-objective optimization concepts can be used to determine appropriate solutions. For example, if we can determine multiple Pareto optimal solutions, we can offer a set of feasible solutions for the metasurface design problem or the dielectric lens design problem. In addition, other than some preliminary 3D work (see [2, 150]), the presented algorithms were presented in a 2D framework and so they can be fully extended to a 3D framework.

Appendix A

Appendix for Gradient-Based Electromagnetic Inversion for Metasurface Design Using Circuit Models

The material in this appendix is published in [38].[1]

A.1 Derivation of Gradient Vectors

We first show a detailed derivation of the gradient $\mathbf{g}_{\mathbf{Y}_1}^{\text{data}}$ for the field (amplitude and phase) pattern synthesis case. (The gradients with respect to layers $\mathbf{Y}_2$ and $\mathbf{Y}_3$ can be derived in a similar manner.) To this end, we first isolate $\mathbf{Y}_1$ from $\mathcal{C}_{\text{data}}(\mathbf{Y})$ by writing

[1] © 2021 IEEE. Reprinted, with permission, from C. Narendra, T. Brown and P. Mojabi, "Gradient-Based Electromagnetic Inversion for Metasurface Design Using Circuit Models," in *IEEE Transactions on Antennas and Propagation*, doi: 10.1109/TAP.2021.3118811.

$\mathbf{A}(\mathbf{Y})$, $\mathbf{B}(\mathbf{Y})$, $\mathbf{C}(\mathbf{Y})$, and $\mathbf{D}(\mathbf{Y})$ as

$$\begin{aligned}
\mathbf{A}(\mathbf{Y}) &= (m_{11}^p m_{11} + jm_{12}^p m_{11}\mathbf{Y_2} + m_{12}^p m_{21} \\
&\quad + jm_{11}^p m_{12}\mathbf{Y_3} - m_{12}^p m_{12}\mathbf{Y_2} \odot \mathbf{Y_3} + jm_{12}^p m_{22}\mathbf{Y_3}) \\
\mathbf{B}(\mathbf{Y}) &= (m_{11}^p m_{12} + m_{12}^p m_{22} + jm_{12}^p m_{12}\mathbf{Y_2}) \\
\mathbf{C}(\mathbf{Y}) &= (jm_{11}^p m_{11}\mathbf{Y_1} + m_{21}^p m_{11} - m_{12}^p m_{11}\mathbf{Y_1} \odot \mathbf{Y_2} \\
&\quad + jm_{22}^p m_{11}\mathbf{Y_2} + jm_{12}^p m_{21}\mathbf{Y_1} + m_{22}^p m_{21} \\
&\quad - m_{11}^p m_{12}\mathbf{Y_1} \odot \mathbf{Y3} + jm_{21}^p m_{12}\mathbf{Y_3} \\
&\quad - jm_{12}^p m_{12}\mathbf{Y_1} \odot \mathbf{Y_2} \odot \mathbf{Y_3} - m_{22}^p m_{12}\mathbf{Y_2} \odot \mathbf{Y_3} \\
&\quad - m_{12}^p m_{22}\mathbf{Y_1} \odot \mathbf{Y_3} + jm_{22}^p m_{22}\mathbf{Y_3}) \\
\mathbf{D}(\mathbf{Y}) &= (jm_{11}^p m_{12}\mathbf{Y_1} + m_{21}^p m_{12} - m_{12}^p m_{12}\mathbf{Y_1} \odot \mathbf{Y_2} \\
&\quad + jm_{22}^p m_{12}\mathbf{Y_2} + jm_{12}^p m_{22}\mathbf{Y_1} + m_{22}^p m_{22})
\end{aligned} \tag{A.1}$$

where the constants m_{ij} and m_{ij}^p can be found as

$$\begin{bmatrix} m_{11} & m_{12} \\ m_{21} & m_{22} \end{bmatrix} = \mathbf{T}_{\text{sub}}, \quad \begin{bmatrix} m_{11}^p & m_{12}^p \\ m_{21}^p & m_{22}^p \end{bmatrix} = \mathbf{T}_{\text{sub}} \cdot \mathbf{T}_{\text{bpl}} \tag{A.2}$$

Therefore, we can rewrite (3.11) for the field pattern synthesis case as a linear function of $\mathbf{Y}_1$ and obtain

$$\mathcal{C}_{\text{data}}(\mathbf{Y_1}) = \zeta_f || \underbrace{\mathbf{L}_1\mathbf{Y_1} + \mathbf{h}_1}_{\mathcal{G}(\mathbf{Y})} - \mathbf{f}||^2, \tag{A.3}$$

where the discrete operator $\mathbf{L_1}$ and vector $\mathbf{h}_1$ arise from factoring $\mathbf{Y}_1$ from $\mathcal{G}(\mathbf{Y})$. (The expression for the operator $\mathbf{L_1}$ will be provided later.) This also means that $\mathbf{L_1}$ and the vector $\mathbf{h}_1$ can be functions of $\mathbf{Y}_2$ and/or $\mathbf{Y}_3$, but not $\mathbf{Y}_1$. (Note that $\mathbf{Y}_2$ and $\mathbf{Y}_3$ are treated as constant vectors in the derivation of the gradient with respect to $\mathbf{Y}_1$.)

To find $\mathbf{g}_{\mathbf{Y}_1}^{\text{data}}$, we first start by finding the differential of the functional with respect to $\mathbf{Y_1}$ as

$$\delta\mathcal{C}_{\text{data}} = \zeta_f \lim_{\epsilon \to 0} \frac{\|\mathbf{L}_1(\mathbf{Y_1} + \epsilon\mathbf{\Psi}) - \mathbf{f}'\|^2 - \|\mathbf{L}_1\mathbf{Y_1} - \mathbf{f}'\|^2}{\epsilon} \tag{A.4}$$

where ϵ is a real number, $\mathbf{f}' = \mathbf{f} - \mathbf{h}_1$, and $\boldsymbol{\Psi}$ is a vector of the same size as $\mathbf{Y}_1$ along which we perturb $\mathbf{Y}_1$. The above limit can be calculated as

$$\begin{aligned}\delta\mathcal{C}_{\text{data}} = \zeta_f \lim_{\epsilon\to 0} \frac{1}{\epsilon}(&\|\mathbf{L}_1\mathbf{Y}_{\mathbf{1}} - \mathbf{f}'\|^2 + \epsilon^2 \|\mathbf{L}_1\boldsymbol{\Psi}\|^2 \\ &+ 2\epsilon \text{Re}\left\langle \mathbf{L}_1\mathbf{Y}_1 - \mathbf{f}', \mathbf{L}_1\boldsymbol{\Psi}\right\rangle \\ &- \|\mathbf{L}_1\mathbf{Y}_{\mathbf{1}} - \mathbf{f}'\|^2)\end{aligned} \tag{A.5}$$

where $\langle\cdot,\cdot\rangle$ denotes the inner product on the ROI. The above differential can then be simplified as

$$\delta\mathcal{C}_{\text{data}} = 2\zeta_f \text{Re}\left\langle \mathbf{L}_1^H(\mathbf{L}_1\mathbf{Y}_1 - \mathbf{f}'), \boldsymbol{\Psi}\right\rangle \tag{A.6}$$

which shows the variation in $\mathcal{C}_{\text{data}}$ due to a small perturbation in $\mathbf{Y}_1$ along the auxiliary vector $\boldsymbol{\Psi}$. Then, similar to [129, Appendix D.5], the gradient vector for the field pattern synthesis case can be identified as

$$\begin{aligned}\mathbf{g}_{\mathbf{Y}_1}^{\text{data}} &= 2\zeta_f \text{Re}\{\mathbf{L}_1^H(\mathbf{L}_1\mathbf{Y}_1 - \mathbf{f}')\} \\ &= 2\zeta_f \text{Re}\{\mathbf{L}_1^H(\mathbf{L}_1\mathbf{Y}_1 + \mathbf{h}_1 - \mathbf{f})\} \\ &= 2\zeta_f \text{Re}\{\mathbf{L}_1^H(\mathcal{G}(\mathbf{Y}) - \mathbf{f})\}\end{aligned} \tag{A.7}$$

which is what is shown in (3.26).

The expression for the matrix $\mathbf{L}_1$ and the other two similar matrices needed to calculate the gradient with respect to $\mathbf{Y}_2$ and $\mathbf{Y}_3$ are

$$\begin{aligned}\mathbf{L}_1 &= \mathbf{A}_{\text{H}_z\text{J}_y}\text{diag}\left(\mathbf{z}_{11}\right) + \mathbf{A}_{\text{H}_z\text{M}_z}\text{diag}\left(\mathbf{z}_{12}\right), \\ \mathbf{L}_2 &= \mathbf{A}_{\text{H}_z\text{J}_y}\text{diag}\left(\mathbf{z}_{21}\right) + \mathbf{A}_{\text{H}_z\text{M}_z}\text{diag}\left(\mathbf{z}_{22}\right), \\ \mathbf{L}_3 &= \mathbf{A}_{\text{H}_z\text{J}_y}\text{diag}\left(\mathbf{z}_{31}\right),\end{aligned} \tag{A.8}$$

where diag$(\cdot)$ is an operator that takes a vector and converts it to a matrix with the original elements of the vector on the diagonal. Also, the above $\mathbf{z}$ vectors are defined as

$$\begin{aligned}
\mathbf{z_{11}} &= (jm_{11}^p m_{11} - m_{12}^p m_{11}\mathbf{Y_2} + jm_{12}^p m_{21} - m_{11}^p m_{12}\mathbf{Y_3} \\
&\quad - jm_{12}^p m_{12}\mathbf{Y_2} \odot \mathbf{Y_3} - m_{12}^p m_{22}\mathbf{Y_3}) \odot \mathbf{E_y^-} \\
\mathbf{z_{12}} &= (m_{12}^p m_{12}\mathbf{Y_2} - jm_{11}^p m_{12} - jm_{12}^p m_{22}) \odot \mathbf{E_y^-} \\
\mathbf{z_{21}} &= (-m_{12}^p m_{11}\mathbf{Y_1} + jm_{22}^p m_{11} - jm_{12}^p m_{12}\mathbf{Y_1} \odot \mathbf{Y_3} \\
&\quad - m_{22}^p m_{12}\mathbf{Y_3}) \odot \mathbf{E_y^-} \\
&\quad - (jm_{12}^p m_{11} + m_{12}^p m_{21} - m_{12}^p m_{12}\mathbf{Y_3}) \odot \mathbf{H_z^-} \\
\mathbf{z_{22}} &= (jm_{12}^p m_{12})\,\mathbf{H_z^-} - (-m_{12}^p m_{12}\mathbf{Y_1} + jm_{22}^p m_{12}) \odot \mathbf{E_y^-} \\
\mathbf{z_{31}} &= (-m_{11}^p m_{12}\mathbf{Y_1} + jm_{21}^p m_{12} - jm_{12}^p m_{12}\mathbf{Y_1} \odot \mathbf{Y_2} \\
&\quad - m_{22}^p m_{12}\mathbf{Y_2} - m_{12}^p m_{22}\mathbf{Y_1} + jm_{22}^p m_{22}) \odot \mathbf{E_y^-} \\
&\quad - (jm_{11}^p m_{12} - m_{12}^p m_{12}\mathbf{Y_2} + jm_{12}^p m_{22}) \odot \mathbf{H_z^-}
\end{aligned} \tag{A.9}$$

where the constants m_{ij} and m_{ij}^p are shown in (A.2).

The derivation of the gradient vector with respect to $\mathbf{Y}_1$ is now presented for the power pattern synthesis case. We begin by calculating the following differential

$$\begin{aligned}
\delta\mathcal{C}_{\text{data}} = \zeta_p \lim_{\epsilon\to 0} \frac{1}{\epsilon}\Big(&\Big\||\mathbf{L}_1(\mathbf{Y_1} + \epsilon\mathbf{\Psi}) + \mathbf{h}_1|^2 - |\mathbf{f}|^2\Big\|^2 \\
&- \Big\||\mathbf{L}_1\mathbf{Y_1} + \mathbf{h}_1|^2 - |\mathbf{f}|^2\Big\|^2\Big)
\end{aligned} \tag{A.10}$$

which can be simplified to

$$\begin{aligned}
\delta\mathcal{C}_{\text{data}} &= 4\zeta_p \text{Re}\left\langle |\mathbf{L}_1\mathbf{Y_1} + \mathbf{h}_1|^2 - |\mathbf{f}|^2, \text{Re}(\mathbf{L}_1\mathbf{\Psi} \odot \mathbf{h}_1^*)\right\rangle \\
&+ 4\zeta_p \text{Re}\left\langle |\mathbf{L}_1\mathbf{Y_1} + \mathbf{h}_1|^2 - |\mathbf{f}|^2, \text{Re}(\mathbf{L}_1\mathbf{Y}_1 \odot (\mathbf{L}_1\mathbf{\Psi})^*)\right\rangle \\
&= 4\zeta_p \text{Re}\left\langle \mathbf{L}_1^H((\mathbf{L}_1\mathbf{Y_1} + \mathbf{h}_1) \odot (|\mathbf{L}_1\mathbf{Y_1} + \mathbf{h}_1|^2 - |\mathbf{f}|^2)), \mathbf{\Psi}\right\rangle.
\end{aligned} \tag{A.11}$$

Thus, the gradient vector of the data misfit cost functional with respect to $\mathbf{Y}_1$ for the power pattern synthesis case can be identified as

$$\begin{aligned}\mathbf{g}_{\mathbf{Y}_1}^{\text{data}} &= 4\zeta_p \text{Re}(\mathbf{L}_1^H((\mathbf{L}_1\mathbf{Y_1} + \mathbf{h}_1) \odot (|\mathbf{L}_1\mathbf{Y_1} + \mathbf{h}_1|^2 - |\mathbf{f}|^2))) \\ &= 4\zeta_p \text{Re}(\mathbf{L}_1^H(\mathcal{G}(\mathbf{Y}) \odot (|\mathcal{G}(\mathbf{Y})|^2 - |\mathbf{f}|^2)))\end{aligned} \tag{A.12}$$

which is what is shown in (3.27).

We use the same procedure to find $\mathbf{g}_{\mathbf{Y}_i}^{\text{JTV}}$, $\mathbf{g}_{\mathbf{Y}_i}^{\text{MTV}}$, and $\mathbf{g}_{\mathbf{Y}_i}^{\text{YTV}}$. For example, for the case of $\mathbf{g}_{\mathbf{Y}_1}^{\text{JTV}}$, we first find the differential of $\mathcal{C}_{\text{JTV}}$ where $\mathbf{Y}_1$ is perturbed by $\epsilon\mathbf{\Psi}$. The differential can then be simplified as

$$\delta\mathcal{C}_{\text{JTV}} = -2\text{Re}\langle\frac{\partial^2}{\partial y^2}(\mathbf{z}_{i1}\mathbf{Y}_i + \mathbf{h}_{\mathbf{J}_i}) \odot \mathbf{z}_{i1}^*, \mathbf{\Psi}\rangle. \tag{A.13}$$

Thus, $\mathbf{g}_{\mathbf{Y}_1}^{\text{JTV}}$ can be identified as

$$\mathbf{g}_{\mathbf{Y}_1}^{\text{JTV}} = -2\text{Re}\{\frac{\partial^2}{\partial y^2}(\mathbf{z}_{i1}\mathbf{Y}_i + \mathbf{h}_{\mathbf{J}_i}) \odot \mathbf{z}_{i1}^*\}. \tag{A.14}$$

For the details of the gradient of TV-based cost functional, we refer the reader to similar derivations available in [129, Appendix D.3] and [99].

A.2 Derivation of Step Length

Herein, we show the derivation of the step length α_1 used in the update of the $\mathbf{Y}_1$ layer according to (3.24) assuming all quantities are in the kth iteration. (The step lengths corresponding to the update for $\mathbf{Y}_2$ and $\mathbf{Y}_3$ are derived in the same manner.) To this end, we need to minimize $\mathcal{C}(\mathbf{Y}_1 + \alpha_1\mathbf{g}_{\mathbf{Y}_1})$ over α_1. Note that the total cost functional $\mathcal{C}$ is the summation of a few cost functionals as shown in (3.22). Herein, for brevity, we perform the procedure merely on its data misfit component, i.e., $\mathcal{C}_{\text{data}}$. Let us first begin

by the data misfit cost functional for the field pattern synthesis case as

$$\begin{aligned}\mathcal{C}_{\text{data}}(\mathbf{Y}_1 + \alpha_1 \mathbf{g}_{\mathbf{Y}_1}) &= \zeta_f \left\| \mathbf{L}_1(\mathbf{Y}_1 + \alpha_1 \mathbf{g}_{\mathbf{Y}_1}) + \mathbf{h}_1 - \mathbf{f} \right\|^2 \\ &= \zeta_f \left\| \mathcal{G}(\mathbf{Y}) - \mathbf{f} \right\|^2 + \alpha_1^2 \zeta_f \left\| \mathbf{L}_1 \mathbf{g}_{\mathbf{Y}_1} \right\|^2 \\ &+ 2\alpha \zeta_f \text{Re}\{\langle \mathcal{G}(\mathbf{Y}) - \mathbf{f}, \mathbf{L}_1 \mathbf{g}_{\mathbf{Y}_1} \rangle\}\end{aligned} \tag{A.15}$$

where $\mathbf{L}_1$ and $\mathbf{h}_1$ have been already defined for (A.3). To solve for the step length, we take the derivative with respect to α_1, set the expression to zero, and solve for α_1 as

$$\alpha_1 = \frac{\text{Re}\{\langle \mathcal{G}(\mathbf{Y}) - \mathbf{f}, \mathbf{L}_1 \mathbf{g}_{\mathbf{Y}_1} \rangle\}}{\left\| \mathbf{L}_1 \mathbf{g}_{\mathbf{Y}_1} \right\|^2}. \tag{A.16}$$

As noted above, the above expression needs to be augmented due to the presence of other cost functionals.

Similarly, for the power pattern synthesis case, let us focus merely on the data misfit cost functional for brevity and write $\mathcal{C}_{\text{data}}(\mathbf{Y}_1 + \alpha_1 \mathbf{g}_{\mathbf{Y}_1})$ as

$$\zeta_p \left\| |\mathbf{L}_1(\mathbf{Y}_1 + \alpha_1 \mathbf{g}_{\mathbf{Y}_1}) + \mathbf{h}_1|^2 - |\mathbf{f}|^2 \right\|^2. \tag{A.17}$$

Expanding the above norm, taking the derivative with respect to α_1, and equating the resulting equation to zero, we arrive at the following equation

$$a_3 \alpha_1^3 + a_2 \alpha_1^2 + a_1 \alpha_1 + a_0 = 0 \tag{A.18}$$

where the coefficients are

$$
\begin{aligned}
a_3 &= 4\left\||\mathbf{L}_1\mathbf{g}_{\mathbf{Y}_1}|^2\right\|^2 \\
a_2 &= 12\mathrm{Re}\{\left\langle|\mathbf{L}_1\mathbf{g}_{\mathbf{Y}_1}|^2, (\mathbf{L}_1\mathbf{g}_{\mathbf{Y}_1}) \odot (\mathbf{h}_1^* + (\mathbf{L}_1\mathbf{Y}_1)^*)\right\rangle\ \} \\
a_1 &= 8\left\|\mathrm{Re}\{(\mathbf{L}_1\mathbf{g}_{\mathbf{Y}_1}) \odot (\mathbf{h}_1^* + (\mathbf{L}_1\mathbf{Y}_1)^*)\}\right\|^2 \\
&\quad + 4\left\langle|\mathbf{L}_1\mathbf{Y}_1|^2 + |\mathbf{h}_1|^2 + 2\mathrm{Re}(\mathbf{L}_1\mathbf{Y}_1 \odot \mathbf{h}_1^*) - |\mathbf{f}|^2, |\mathbf{L}_1\mathbf{g}_{\mathbf{Y}_1}|^2\right\rangle \\
a_0 &= 4\mathrm{Re}\langle|\mathbf{L}_1\mathbf{Y}_1|^2 + |\mathbf{h}_1|^2 + 2\mathrm{Re}(\mathbf{L}_1\mathbf{Y}_1 \odot \mathbf{h}_1^*) - |\mathbf{f}|^2, \\
&\qquad\qquad (\mathbf{L}_1\mathbf{g}_{\mathbf{Y}_1}) \odot (\mathbf{h}_1^* + (\mathbf{L}_1\mathbf{Y}_1)^*)\rangle
\end{aligned}
\tag{A.19}
$$

Once we solve (A.18), its real root serves as our step length for the update of $\mathbf{Y}_1$ in the power pattern synthesis case. Note that for the complete implementation, the expressions in (A.19) need to be augmented by some other components due to the involvement of the other cost functionals.

Appendix B

Appendix for Phaseless Gauss-Newton Inversion for Microwave Imaging

The material in this appendix is published in [41].[1]

B.1 Required Derivative Operators

Herein, we show in more detail how we minimize the phaseless data misfit cost functional $\mathcal{C}(\chi)$ using the Gauss-Newton inversion framework. In particular, we aim to derive the main (unregularized) update equation given in (4.9). At the n^{th} iteration, we update our latest χ_n as $\chi_{n+1} = \chi_n + \nu_n \Delta\chi_n$ by minimizing the regularized form of $\mathcal{C}(\chi)$. This requires the derivative operators of both the phaseless data misfit functional and the regularization terms. Since the regularizations terms for full data (complex) inversion

[1] © 2021 IEEE. Reprinted, with permission, from C. Narendra and P. Mojabi, "Phaseless Gauss-Newton Inversion for Microwave Imaging," in *IEEE Transactions on Antennas and Propagation*, vol. 69, no. 1, pp. 443-456, Jan. 2021, doi: 10.1109/TAP.2020.3026427.

and phaseless inversion are the same, we focus on the required derivative operators for the phaseless data misfit cost functional. The phaseless cost functional $\mathcal{C}(\chi)$ maps the complex vector χ to a real number and is not analytic with respect to χ in the complex domain. Therefore, in order to calculate $\Delta\chi_n$ within the GNI framework, we use Wirtinger calculus [129, 151–153] to define the required derivative operators. This is based on treating χ and its complex conjugate χ^* as two independent functions (or, vectors in the discrete domain).[2] The GNI framework calculates the update $\Delta\chi_n$ by approximating $\mathcal{C}(\chi + \Delta\chi_n)$ by a quadratic model. The update $\Delta\chi_n$ is then found for the minimum of this quadratic model. Within the Wirtinger calculus framework, we consider the cost functional $\mathcal{C}(\chi, \chi*) = \mathcal{C}(\chi)$, where $\mathcal{C}(\chi, \chi*)$ is analytic with respect to χ for a fixed $\chi*$ and also analytic with respect to $\chi*$ for a fixed χ. Minimizing $\mathcal{C}(\chi, \chi*)$ is equivalent to minimizing $\mathcal{C}(\chi)$. Applying Newton optimization to the phaseless cost functional leads to $\Delta\chi_n$ obeying the following relation

$$\begin{pmatrix} \frac{\partial^2\mathcal{C}}{\partial\chi\partial\chi} & \frac{\partial^2\mathcal{C}}{\partial\chi\partial\chi^*} \\ \\ \frac{\partial^2\mathcal{C}}{\partial\chi^*\partial\chi} & \frac{\partial^2\mathcal{C}}{\partial\chi^*\partial\chi^*} \end{pmatrix} \begin{pmatrix} \Delta\chi_n \\ \\ \Delta\chi_n^* \end{pmatrix} = - \begin{pmatrix} \frac{\partial\mathcal{C}}{\partial\chi} \\ \\ \frac{\partial\mathcal{C}}{\partial\chi^*} \end{pmatrix} \tag{B.1}$$

where $\frac{\partial\mathcal{C}}{\partial\chi}$ and $\frac{\partial\mathcal{C}}{\partial\chi^*}$ are the derivative operators with respect to χ and χ^*, respectively at the n^{th} iteration. These derivative operators, in the discrete domain, act on a complex vector and output a complex number. Similarily, $\frac{\partial^2\mathcal{C}}{\partial\chi\partial\chi}$ is a second derivative operator, in this case, with respect to χ and then χ again evaluated at the n^{th} iteration of the algorithm. In the discrete domain, the second order derivative operators act on a complex vector and output a complex vector.

[2] An alternative approach would be to optimize over the real and imaginary parts of the contrast. This has been shown to be the same as treating χ and χ^* as two independent functions (vectors), see [129, Appendix D.5].

B.1.1 First Order Derivative Operators

In order to derive the required first order derivative operators, we use the following relation

$$\delta\mathcal{C} = \lim_{\epsilon \to 0} \frac{\mathcal{C}(\chi + \epsilon\psi) - \mathcal{C}(\chi)}{\epsilon} \tag{B.2}$$

where $\epsilon \in \mathbb{R}$ is a scalar, and ψ is an arbitrary function (vector) that is used to modify χ. Since we are treating χ and χ^* as two independent functions, δC will be[3]

$$\delta\mathcal{C} = \frac{\partial\mathcal{C}}{\partial\chi}(\psi) + \frac{\partial\mathcal{C}}{\partial\chi^*}(\psi^*). \tag{B.3}$$

As will be seen later, the two terms on the right hand side of (B.3) are complex conjugates of each other. Therefore, $\delta\mathcal{C}$ will be a real number. This is expected since $\mathcal{C}(\chi) \in \mathbb{R}$. Also, note that the range of these two first order derivative operators will be complex numbers. In other words, the operation of these derivative operators can be represented by inner products. In our case, the inner product over the ROI is defined as

$$\langle\varphi, \psi\rangle = \int_{\text{ROI}} \varphi\ \psi^* ds. \tag{B.4}$$

Based on this, the right hand side of (B.3) can be represented by two inner products, from which we can obtain the expression for the first order derivative operators. In (B.5), we have shown how to write $\delta\mathcal{C}$ based on two inner products. It should be noted that $\frac{\partial E}{\partial\chi}$ in (B.5) should be evaluated at the current estimate of χ, and 'Re' denotes the real-part operator. For example, when we are at the n^{th} iteration, this derivative operator should be evaluated at $\chi = \chi_n$. In addition, the second order derivative $\frac{\partial^2 E}{\partial\chi^2}$ has been neglected (GNI approximation) in (B.5). Noting (B.5) and the definition of the inner product over the ROI given in (B.4), it is now possible to identify our first order derivative operators.

[3]To understand this better, let us consider a function such as $f(x, y)$, then $\delta f = \frac{\partial f}{\partial x}\delta x + \frac{\partial f}{\partial y}\delta y$. Since we have treated χ and χ^* as two independent functions, we have a similar form for $\delta\mathcal{C}$ as shown in (B.3).

$$
\begin{aligned}
\delta\mathcal{C} &= \lim_{\epsilon\to 0}\frac{\zeta}{\epsilon}\left(\left\|M^2-|E(\chi+\epsilon\psi)|^2\right\|^2-\left\|M^2-|E(\chi)|^2\right\|^2\right)\\
&= \lim_{\epsilon\to 0}\frac{\zeta}{\epsilon}\left(\left\|M^2-\left|E(\chi)+\epsilon\frac{\partial E}{\partial\chi}\psi\right|^2\right\|^2-\left\|M^2-|E(\chi)|^2\right\|^2\right)\\
&= \lim_{\epsilon\to 0}\frac{\zeta}{\epsilon}\left(\left\|M^2-\left(|E(\chi)|^2+\left|\epsilon\frac{\partial E}{\partial\chi}\psi\right|^2+2\epsilon\mathrm{Re}\left\{E(\chi)^*\frac{\partial E}{\partial\chi}\psi\right\}\right)\right\|^2-\left\|M^2-|E(\chi)|^2\right\|^2\right)\\
&= \lim_{\epsilon\to 0}\frac{\zeta}{\epsilon}\left(4\epsilon^2\left\|\mathrm{Re}\left\{E(\chi)^*\frac{\partial E}{\partial\chi}\psi\right\}\right\|^2+2\mathrm{Re}\left\langle M^2-|E(\chi)|^2,-2\zeta\epsilon\mathrm{Re}\left\{E(\chi)^*\frac{\partial E}{\partial\chi}\psi\right\}\right\rangle\right)\\
&= -2\zeta\mathrm{Re}\left\langle M^2-|E(\chi)|^2,2\mathrm{Re}\left\{E(\chi)^*\frac{\partial E}{\partial\chi}\psi\right\}\right\rangle\\
&= -2\zeta\left\langle M^2-|E(\chi)|^2,E(\chi)^*\frac{\partial E}{\partial\chi}\psi+E(\chi)\left(\frac{\partial E}{\partial\chi}\psi\right)^*\right\rangle\\
&= -2\zeta\left\langle M^2-|E(\chi)|^2,E(\chi)^*\frac{\partial E}{\partial\chi}\psi\right\rangle-2\zeta\left\langle M^2-|E(\chi)|^2,E(\chi)\left(\frac{\partial E}{\partial\chi}\psi\right)^*\right\rangle\\
&= \underbrace{\left\langle 2\zeta\left(\frac{\partial E}{\partial\chi}\right)^a\left(E(\chi)\left(|E(\chi)|^2-M^2\right)\right),\psi\right\rangle}_{\frac{\partial\mathcal{C}}{\partial\chi^*}(\psi^*)}+\underbrace{\left\langle 2\zeta\left(\left(\frac{\partial E}{\partial\chi}\right)^a\left(E(\chi)\left(|E(\chi)|^2-M^2\right)\right)\right)^*,\psi^*\right\rangle}_{\frac{\partial\mathcal{C}}{\partial\chi}(\psi)=\left(\frac{\partial\mathcal{C}}{\partial\chi^*}(\psi^*)\right)^*}
\end{aligned}
\tag{B.5}
$$

In the discrete domain, the first order derivative operators evaluated at χ_n are

$$
\begin{aligned}
\left.\frac{\partial\mathcal{C}}{\partial\chi^*}\right|_{\chi=\chi_n} &= 2\zeta\mathbf{J}_n^H\left[E(\chi_n)\odot\left(|E(\chi_n)|^2-M^2\right)\right]\\
\left.\frac{\partial\mathcal{C}}{\partial\chi}\right|_{\chi=\chi_n} &= \left(\left.\frac{\partial\mathcal{C}}{\partial\chi^*}\right|_{\chi=\chi_n}\right)^*
\end{aligned}
\tag{B.6}
$$

where ζ is the normalization coefficient of the phaseless data misfit cost functional, see (4.8), and $\mathbf{J}_n$ denotes the Jacobian (sensitivity) matrix that represents the derivative of the total field data on the measurement domain with respect to the contrast χ (i.e., $\frac{\partial E}{\partial\chi}$).[4]

[4]The derivation and expression for the Jacobian matrix can be found in [129, Appendix D.1]. This requires the calculation of the so-called inhomogeneous (or, distorted) Green's function. Also, we remind the reader that the derivative of the total field with respect to the contrast is the same as the derivative of the scattered field with respect to the contrast.

$$
\begin{aligned}
\delta^2\mathcal{C}_1 &= \lim_{\epsilon\to 0}\frac{1}{\epsilon}\left[\left\langle 2\zeta\frac{\partial E}{\partial\chi}\Big|_{\chi+\epsilon\psi}(\varphi),\left[E(\chi+\epsilon\psi)(|E(\chi+\epsilon\psi)|^2-M^2)\right]\right\rangle - \left\langle 2\zeta\frac{\partial E}{\partial\chi}(\varphi),\left[E(\chi)(|E(\chi)|^2-M^2)\right]\right\rangle\right] \\
&= \lim_{\epsilon\to 0}\frac{1}{\epsilon}\left[2\zeta\left\langle\left(\frac{\partial E}{\partial\chi}+\epsilon\frac{\partial^2 E}{\partial\chi^2}(\psi)\right)(\varphi),\left(E(\chi)+\epsilon\frac{\partial E}{\partial\chi}(\psi)\right)\left(\left|E(\chi)+\epsilon\frac{\partial E}{\partial\chi}(\psi)\right|^2-M^2\right)\right\rangle\cdots\right. \\
&\qquad\qquad \left. -2\zeta\left\langle\frac{\partial E}{\partial\chi}(\varphi),E(\chi)\left(|E(\chi)|^2-M^2\right)\right\rangle\right] \\
&= \lim_{\epsilon\to 0}\frac{1}{\epsilon}\left[2\zeta\left\langle\frac{\partial E}{\partial\chi}(\varphi),\left(E(\chi)+\epsilon\frac{\partial E}{\partial\chi}(\psi)\right)\left(|E(\chi)|^2+\epsilon^2\left|\frac{\partial E}{\partial\chi}(\psi)\right|^2+2\epsilon\mathrm{Re}\left(E(\chi)^*\frac{\partial E}{\partial\chi}(\psi)\right)-M^2\right)\right\rangle\cdots\right. \\
&\qquad\qquad \left. -2\zeta\left\langle\frac{\partial E}{\partial\chi}(\varphi),E(\chi)(|E(\chi)|^2-M^2)\right\rangle\right] \\
&= \lim_{\epsilon\to 0}\frac{1}{\epsilon}\left[2\zeta\left\langle\frac{\partial E}{\partial\chi}(\varphi),\left(E(\chi)2\epsilon\mathrm{Re}\left(E(\chi)^*\frac{\partial E}{\partial\chi}(\psi)\right)\right)\right\rangle+2\zeta\left\langle\frac{\partial E}{\partial\chi}(\varphi),\epsilon\frac{\partial E}{\partial\chi}(\psi)\left(|E(\chi)|^2-M^2\right)\right\rangle\right] \\
&= 2\zeta\left\langle\frac{\partial E}{\partial\chi}(\varphi),E(\chi)E(\chi)^*\frac{\partial E}{\partial\chi}(\psi)\right\rangle+2\zeta\left\langle\frac{\partial E}{\partial\chi}(\varphi),E(\chi)E(\chi)\left[\frac{\partial E}{\partial\chi}(\psi)\right]^*\right\rangle+2\zeta\left\langle\frac{\partial E}{\partial\chi}(\varphi),\frac{\partial E}{\partial\chi}(\psi)\left(|E(\chi)|^2-M^2\right)\right\rangle \\
&= \underbrace{\left\langle 2\zeta\left(\frac{\partial E}{\partial\chi}\right)^a\left(2|E(\chi)|^2-M^2\right)\frac{\partial E}{\partial\chi}(\varphi),\psi\right\rangle}_{\frac{\partial^2\mathcal{C}}{\partial\chi^*\partial\chi}(\varphi)(\psi^*)}+\underbrace{\left\langle 2\zeta\left(\left(\frac{\partial E}{\partial\chi}\right)^a E^2(\chi)\left(\frac{\partial E}{\partial\chi}(\varphi)\right)^*\right)^*,\psi^*\right\rangle}_{\frac{\partial^2\mathcal{C}}{\partial\chi\partial\chi}(\varphi)(\psi)}
\end{aligned}
\tag{B.8}
$$

B.1.2 Second Order Derivative Operators

To calculate the second order derivative operators required to calculate $\Delta\chi_n$, we first calculate a second order differential as [129, Appendix D.2]

$$
\delta^2\mathcal{C}_1 = \lim_{\epsilon\to 0}\frac{\frac{\partial\mathcal{C}}{\partial\chi}|_{\chi+\epsilon\psi}(\varphi)-\frac{\partial\mathcal{C}}{\partial\chi}|_{\chi}(\varphi)}{\epsilon}, \tag{B.7}
$$

where the vertical lines denote that the derivative operators are evaluated at $\chi+\epsilon\psi$ and χ respectively. Note that the first order derivative operators are operating on an arbitrary function φ (or, vector in the discrete domain). Also, note that the expressions for the first-order derivative operators have been derived in (B.5), which will now be used to find the second-order derivative operators. Similar to the first order derivative case, some of the intermediate steps are shown in (B.8). (For simplicity of notation, the derivative operator $\frac{\partial E}{\partial\chi}$ when used without a vertical line indicates that this operator is evaluated at χ as opposed to at $\chi+\epsilon\psi$.) Using the result in (B.8), the second order derivative operators can be found by noting that $\delta^2 C$ can be written as

$$\delta^2\mathcal{C} = \overbrace{\left[\frac{\partial^2\mathcal{C}}{\partial\chi^*\partial\chi}(\varphi)(\psi^*) + \frac{\partial^2\mathcal{C}}{\partial\chi\partial\chi}(\varphi)(\psi)\right]}^{\delta^2\mathcal{C}_1} + \underbrace{\left[\frac{\partial^2\mathcal{C}}{\partial\chi^*\partial\chi^*}(\varphi^*)(\psi^*) + \frac{\partial^2\mathcal{C}}{\partial\chi\partial\chi^*}(\varphi^*)(\psi)\right]}_{\delta^2\mathcal{C}_2=(\delta^2\mathcal{C}_1)^*} = 2\mathrm{Re}(\delta^2\mathcal{C}_1). \tag{B.9}$$

Thus, it follows that, in the discrete domain, the second order derivative operators derived from (B.8) are

$$\frac{\partial^2\mathcal{C}}{\partial\chi^*\partial\chi}(\varphi)(\psi^*) = 2\zeta\mathbf{J}_n^H\mathrm{diag}(2|E(\chi_n)|^2 - M^2)\mathbf{J}_n, \tag{B.10}$$

$$\frac{\partial^2\mathcal{C}}{\partial\chi\partial\chi}(\varphi)(\psi) = 2\zeta\mathbf{J}_n^T\mathrm{diag}(E^2(\chi))^*\mathbf{J}_n, \tag{B.11}$$

$$\frac{\partial^2\mathcal{C}}{\partial\chi\partial\chi^*}(\varphi^*)(\psi) = \left(\frac{\partial^2\mathcal{C}}{\partial\chi^*\partial\chi}(\varphi)(\psi^*)\right)^*, \tag{B.12}$$

$$\frac{\partial^2\mathcal{C}}{\partial\chi^*\partial\chi^*}(\varphi^*)(\psi^*) = \left(\frac{\partial^2\mathcal{C}}{\partial\chi\partial\chi}(\varphi)(\psi)\right)^*. \tag{B.13}$$

In addition to assuming that $\frac{\partial^2 E}{\partial\chi^2}$ is negligible in (B.8), we make the following extra assumption: $\frac{\partial^2\mathcal{C}}{\partial\chi\partial\chi}$ and consequently $\frac{\partial^2\mathcal{C}}{\partial\chi^*\partial\chi^*}$ are disregarded since they are not hermitian (self adjoint) operators.[5]

Based on the above approximation and assumption, (B.1) at the n^{th} iteration will simplify to

$$\left.\frac{\partial^2\mathcal{C}}{\partial\chi^*\partial\chi}\right|_{\chi=\chi_n}\Big(\Delta\chi_n\Big) = -\left.\frac{\partial\mathcal{C}}{\partial\chi^*}\right|_{\chi=\chi_n}. \tag{B.14}$$

Note that the above equation in the continuous domain indicates the equality of two operators. However, in the discrete domain, it represents the equality of two vectors. In

[5]Note that this extra assumption was not needed in the development of the complex GNI algorithm [129, Equation (D.33)]. In fact, in the complex GNI algorithm, the assumption of a negligible $\frac{\partial^2 E}{\partial\chi^2}$ is sufficient to have $\frac{\partial^2\mathcal{C}}{\partial\chi\partial\chi}$ and $\frac{\partial^2\mathcal{C}}{\partial\chi^*\partial\chi^*}$ as zero.

particular, using (B.10) and (B.6), the discrete form of (B.14) will become

$$\left[2\zeta \mathbf{J}_n^H \mathrm{diag}(2|E(\chi_n)|^2 - M^2)\mathbf{J}_n\right]\Delta\chi_n = \\ -2\zeta \mathbf{J}_n^H \left[E(\chi_n) \odot (|E(\chi_n)|^2 - M^2)\right]. \tag{B.15}$$

This is the main update equation (in un-regularized form) which was shown in (4.9).

B.2 Convergence Behaviour

Herein, we provide some more detail on the convergence and computational requirements for the proposed phaseless GNI algorithms. First, since these algorithms are iterative by nature, they require stopping criteria. In this work, we chose to stop the algorithm when $\mathcal{C}(\chi_n)$ decreased below a tolerance of 10^{-3} (to ensure the functional error had decreased appropriately) or when the change in $\mathcal{C}$ value was smaller than a tolerance of 10^{-4} after two consecutive iterations (to stop the algorithm when the cost functional is stagnant). The actual tolerance values were chosen in an *ad hoc* manner from past experience.

All of these results were generated on a laptop computer with a 2.4 GHz Intel Core i5 processor and 16 GB 1600 MHz DDR3 RAM in MATLAB. To compare the performance of each of the proposed phaseless GNI imaging schemes, Table B.1 shows the average iteration time for the PGNI, SL-PGNI, and SP-PGNI algorithms from the synthetic concentric square examples in Section 4.5.1. As can be seen, in this example, all the algorithms show a similar average iteration time. This is expected because all these algorithms, at each iteration, require the same number of forward scattering solver runs. (The utilized forward solver is a CG-FFT accelerated method of moments.) However, their computational time per iteration are not identical since each inversion algorithm requires a different matrix-vector multiplication to solve for $\Delta\chi_n$. It should be noted that in some cases, one of the phaseless methods can take many more iterations due to the difference of the regularization schemes. For example, for the experimental FoamTwinDielTM

Table B.1: Comparison of Average Iteration Time Between the PGNI, SL-PGNI, and SP-PGNI Algorithms for the Concentric Square Example

	PGNI	SL-PGNI	SP-PGNI
Time [s]	12.27	11.30	12.76
Total Iterations	7	8	8

dataset shown in Section 4.5.3, the SL-PGNI algorithm took 19 iterations to converge in a time of 8495.58 seconds, however, the functional error at convergence was 0.029 as compared to a functional value of 0.043 in the SP-PGNI case which converged in only 8 iterations. In this case, the SL-PGNI regularization technique was able to decrease the functional more than others and this resulted in more iterations and a longer total solution time (this was the longest solution time of all the results in the paper).

We note that it is not possible to make a general statement about if a particular regularization scheme will always converge more quickly than others based on the experiments that were carried out. However, the SL-PGNI, and SP-PGNI algorithm always converged to a lower $\mathcal{C}(\chi_n)$ value than the PGNI algorithm. This is to be expected as the former two algorithms incorporate more information into the inverse scattering problem.

Appendix C

Antenna Characterization using Multi-Plane Near-Field Data

Preface

This work is a demonstration of using an electromagnetic inverse source algorithm for the purpose of antenna characterization. The material presented in this appendix was published as a conference paper for the 2018 18th International Symposium on Antenna Technology and Applied Electromagnetics (ANTEM) conference in December 2018 [15].[1]

Abstract

We deal with a specific planar near-field measurement system where magnetic field data is collected by a compact 2-D array of magnetic probes. To enable this *planar* system to

[1] © 2018 IEEE. Reprinted, with permission, from C. Narendra, T. Brown, N. Bayat and P. Mojabi, "Multi-Plane Magnetic Near-Field Data Inversion Using the Source Reconstruction Method," *2018 18th International Symposium on Antenna Technology and Applied Electromagnetics (ANTEM)*, 2018, pp. 1-2, doi: 10.1109/ANTEM.2018.8572920.

utilize a more complete set of magnetic field data, we present a method that can invert *multiple* planes of magnetic data collected by rotating the antenna under test. It is then synthetically shown that by using the presented method the far-field accuracy of an inset-fed patch antenna can be improved compared to the original case where only one plane of magnetic data is utilized.

C.1 Introduction

Near-field antenna measurement systems and techniques are commonly utilized in industrial applications and research communities due to their many advantages such as: requiring less physical space than most far-field measurement systems, generally being less expensive than far-field systems because they don't require as much specialized equipment (*e.g.* reflectors in compact ranges) and space, and readily enabling antenna diagnostics. These benefits make near-field systems sought after tools for antenna engineers.

EMSCAN Corp. has developed compact, bench-top, fast magnetic near-field measurement systems [154]. For example, their RFxpert system measures the tangential magnetic field data produced by the antenna under test (AUT) over a single planar surface. This magnetic field data is then processed using modal expansion techniques to calculate (in quasi real-time) the far-field pattern of the AUT for the user. This method is more suited for directive AUTs because most of the energy emitted from the device can be measured by the planar array of magnetic probes.

In this work we present a method (based on simulation studies) that demonstrates the potential to use EMSCAN bench-top measurement systems with less directive antennas. Our method requires the rotation of the AUT on the EMSCAN measurement system to acquire *multiple* planes of magnetic data. Then we use the source reconstruction method (SRM) [47, 155] with a method of moments (MoM) based solver to invert the complete set of magnetic measurement data to find equivalent sources that produce the far-field of the AUT.

We first briefly explain the theory behind our technique, then we show synthetic tests that demonstrate the far-field accuracy improvement afforded by incorporating multiple planes of magnetic field measurement data from an inset-fed patch antenna.

C.2 Theory

The SRM is founded from the electromagnetic equivalence principle [11]. It enables the calculation of a set of equivalent currents on an enclosing reconstruction surface D that replaces the original source. This is done by measuring the tangential electric or magnetic field components on a measurement surface S (of arbitrary shape) and solving an electromagnetic inverse source problem to calculate the equivalent currents. The currents can then be used for diagnostics or in a forward solver to calculate the far-field radiation pattern [47].

In our case, we assume that we have multiple planes of tangential magnetic field data which can be acquired, for example, from EMSCAN's RFxpert system. The consolidation of the individual planes defines the complete measurement surface S. We also assume to know the approximate geometry of the AUT so we can define a reconstruction surface D enclosing the AUT. The magnetic field measurements on S are related to the equivalent currents on D according to equations that can be found from the well-known electric field integral equations (EFIE) and the principle of duality [11, 47].

When solving these integral equations for the equivalent electric and magnetic currents on D, we discretize the problem using the MoM and we use Rao-Wilton-Glisson (RWG) basis functions to represent the currents [156]. Once discretized we are left with a linear matrix equation where an operator matrix maps the electric and magnetic currents to the measured magnetic field data. The resulting inverse source problem is solved by applying the conjugate gradient method [29]. Once a set of equivalent currents have been found, we can create an operator to map the currents to the far-field by using the EFIE.

C.3 Results

To evaluate the performance of the proposed method, we perform a near-field to far-field transformation using synthetic data generated from ANSYS HFSS. The AUT is an inset-fed patch antenna of dimensions 50 mm × 49.7 mm × 1.6 mm operating at a frequency of 2.35 GHz. Synthetic magnetic field data is generated on six measurement planes, as depicted in Figure C.1. Each measurement plane has dimensions of 16 cm × 24 cm

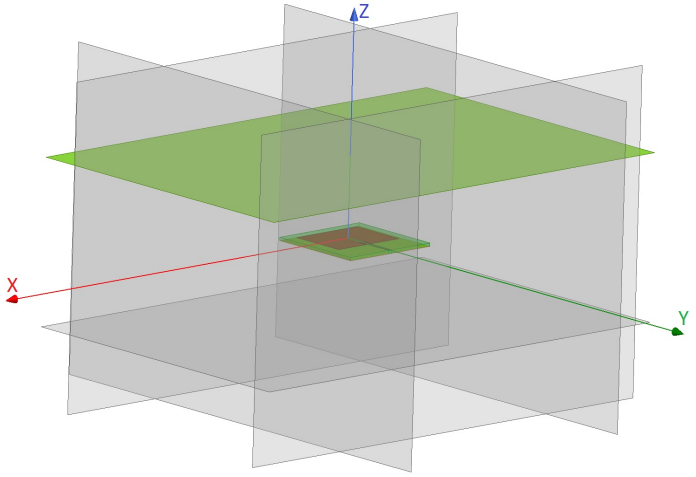

Figure C.1: A diagram of the inset-fed patch antenna and the six planes upon which synthetic magnetic field data is generated. The direction of the main beam is toward the positive z-axis (*i.e.* toward the highlighted plane).

with data collected at 1 cm intervals, matching the specifications of EMSCAN's RFxpert system (RFX model). Each measurement plane is placed a distance of 4 cm away from the nearest edge of the antenna. The reconstruction surface D is a box of dimensions 6 cm × 6 cm × 3 cm, discretized into 364 triangular elements.

The developed SRM is used to produce the far-field radiation pattern using all six planes of synthetically collected data, and compared to the standard planar case using a single measurement plane (the plane intersecting the z-axis and highlighted in Figure C.1) as well as the true far-field pattern produced by HFSS. The E-plane and H-plane cuts of the far-field pattern are shown in Figure C.2. The normalized L^2 norm percent relative error (calculated as in [24]) between the far-field pattern produced using a single measurement

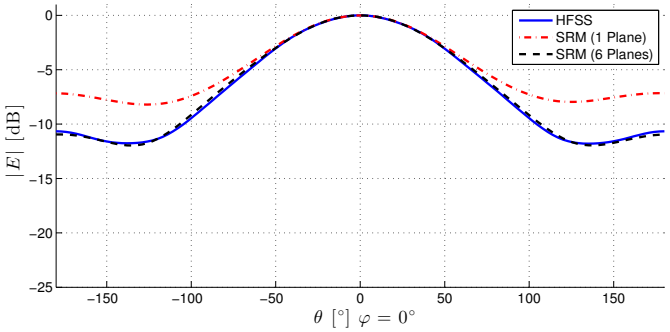

(a)

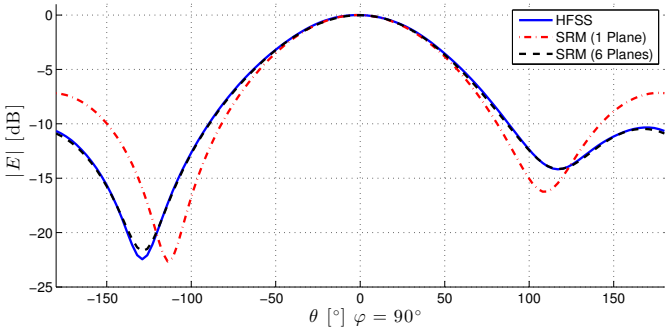

(b)

Figure C.2: A comparison of the patch antenna far-field radiation pattern produced by: SRM using only one plane ($z = 4$ cm) of measurement data (dash-dotted line), SRM using six planes of measurement data (dashed line), and HFSS (solid line). The E-plane pattern ($\varphi = 0°$) is shown in (a) while the H-plane pattern ($\varphi = 90°$) is shown in (b).

plane and the pattern generated using HFSS is 14.96%, while using six measurement planes reduced the difference to 0.972%.

C.4 Conclusion and Future Work

We presented a method that has the potential to enable an existing compact planar magnetic near-field measurement system to utilize more data. By rotating the antenna on this system, multiple planes of magnetic field data can be collected. Then this consolidated set of data can be inverted using the source reconstruction method and the far-field pattern of the AUT can be calculated. It was synthetically shown that this method provides an

improvement in the calculated far-field accuracy of an inset-fed patch antenna when compared to the original case where a single plane of magnetic data is used to calculate the far-field. We intend to improve this work by validating it with experimental data from the RFxpert system. It is also our goal to modify our method to be capable of de-embedding the effect of RFxpert's ground plane from the multiple planes of magnetic field data that our method requires. This can be, for example, based on the work presented in [157] and will be discussed at the conference.

Appendix D

List of Publications

A list of publications resulting from the work herein is listed below as well the contributions of the authors:

Journal Papers:

1. **Chaitanya Narendra** and Puyan Mojabi, "A Combined Inverse Source and Scattering Technique for Dielectric Profile Design to Tailor Electromagnetic Fields," in *IEEE Transactions on Antennas and Propagation*,
   doi: 10.1109/TAP.2021.3119049.
   - Chaitanya Narendra: manuscript preparation, algorithm development, simulations
   - Puyan Mojabi: advisory role, simulations
2. **Chaitanya Narendra**, Trevor Brown and Puyan Mojabi, "Gradient-Based Electromagnetic Inversion for Metasurface Design Using Circuit Models", in *IEEE Transactions on Antennas and Propagation*,
   doi: 10.1109/TAP.2021.3118811.
   - Chaitanya Narendra: manuscript preparation, algorithm development, simulations

- Trevor Brown: manuscript preparation, gradient derivation
- Puyan Mojabi: advisory role

3. **Chaitanya Narendra** and Puyan Mojabi, "Phaseless Gauss-Newton Inversion for Microwave Imaging," in *IEEE Transactions on Antennas and Propagation*, vol. 69, no. 1, pp. 443-456, Jan. 2021, doi: 10.1109/TAP.2020.3026427.
   - Chaitanya Narendra: manuscript preparation, algorithm development, verification
   - Puyan Mojabi: advisory role, algorithm development, manuscript preparation
4. Trevor Brown, **Chaitanya Narendra**, Yousef Vahabzadeh, Christophe Caloz, and Puyan Mojabi, "On the Use of Electromagnetic Inversion for Metasurface Design", *IEEE Transactions on Antennas and Propagation*, vol. 68, no. 3, pp. 1812-1824, 2020.
   - Trevor Brown: manuscript preparation, inversion framework development and evaluation, simulations
   - Chaitanya Narendra: manuscript preparation, conjugate gradient algorithm
   - Yousef Vahabzadeh: finite-difference frequency domain simulation code
   - Christophe Caloz and Puyan Mojabi: advisory role

Conference Papers:

1. P. Mojabi, T. Brown and **C. Narendra**, "Phaseless Electromagnetic Inversion for Imaging, Characterization, and Design," *2021 IEEE 19th International Symposium on Antenna Technology and Applied Electromagnetics (ANTEM)*, 2021, pp. 1-2.
   - Puyan Mojabi: main author, manuscript preparation
   - Trevor Brown: provided advice and access to past results for this review paper

- Chaitanya Narendra: provided advice and access to past results for this review paper

2. **C. Narendra** and P. Mojabi, "A Phaseless Gauss-Newton Inversion Algorithm for Imaging and Design," *2020 14th European Conference on Antennas and Propagation (EuCAP)*, 2020, pp. 1-5.
   - Chaitanya Narendra: manuscript preparation, algorithm development, verification
   - Puyan Mojabi: advisory role, algorithm development, manuscript preparation
3. Trevor Brown, **Chaitanya Narendra**, Yousef Vahabzadeh, Christophe Caloz, and Puyan Mojabi, "Metasurface Design Using Electromagnetic Inversion", *2019 IEEE International Symposium on Antennas and Propagation and USNC-URSI Radio Science Meeting*, pp. 1817-1818, 2019.
   - Trevor Brown: manuscript preparation, algorithm development and evaluation, simulations
   - Chaitanya Narendra: conjugate gradient algorithm manuscript preparation
   - Yousef Vahabzadeh: finite-difference frequency domain simulation code
   - Christophe Caloz and Puyan Mojabi: advisory role
4. Trevor Brown, **Chaitanya Narendra**, Chen Niu, and Puyan Mojabi, "On the Use of Electromagnetic Inversion for Near-Field Antenna Measurements: A Review", *2018 Conference on Antenna Measurements and Applications (CAMA)*, pp. 1-4, 2018.
   - Trevor Brown: manuscript preparation, phaseless measurements and data-prescaling algorithms
   - Chaitanya Narendra: irregular measurement domain algorithms
   - Chen Niu: development, construction of and examples from a pendulum-based planar near-field antenna measurement system

- Puyan Mojabi: advisory role

5. **Chaitanya Narendra**, Trevor Brown, Nozhan Bayat, and Puyan Mojabi, "Multi-Plane Magnetic Near-Field Data Inversion Using the Source Reconstruction Method", *2018 18th International Symposium on Antenna Technology and Applied Electromagnetics (ANTEM)*, pp. 1-2, 2018.
   - Chaitanya Narendra: manuscript preparation, algorithm development and evaluation
   - Trevor Brown: inversion framework
   - Nozhan Bayat: HFSS simulations
   - Puyan Mojabi: advisory role
6. Trevor Brown, **Chaitanya Narendra**, and Puyan Mojabi, "On the Use of the Source Reconstruction Method for Metasurface Design", *2018 18th European Conference on Antennas and Propagation (EuCAP)*, pp. 302-306, 2018.
   - Trevor Brown: manuscript preparation, algorithm development and evaluation, simulations
   - Chaitanya Narendra: conjugate gradient algorithm
   - Puyan Mojabi: advisory role

Bibliography

[1] C. Narendra and P. Mojabi, "A phaseless gauss-newton inversion algorithm for imaging and design," in *2020 14th European Conference on Antennas and Propagation (EuCAP)*, 2020, pp. 1–5.

[2] T. Brown, C. Narendra, Y. Vahabzadeh, C. Caloz, and P. Mojabi, "On the use of electromagnetic inversion for metasurface design," *IEEE Transactions on Antennas and Propagation*, vol. 68, no. 3, pp. 1812–1824, 2019.

[3] J.-M. Geffrin, P. Sabouroux, and C. Eyraud, "Free space experimental scattering database continuation: experimental set-up and measurement precision," *inverse Problems*, vol. 21, no. 6, p. S117, 2005.

[4] M. Ostadrahimi, P. Mojabi, A. Zakaria, J. LoVetri, and L. Shafai, "Enhancement of gauss–newton inversion method for biological tissue imaging," *IEEE Transactions on Microwave Theory and Techniques*, vol. 61, no. 9, pp. 3424–3434, 2013.

[5] C. A. Balanis, *Antenna theory: analysis and design*. John wiley & sons, 2016.

[6] K. Achouri, M. A. Salem, and C. Caloz, "General metasurface synthesis based on susceptibility tensors," *IEEE Transactions on Antennas and Propagation*, vol. 63, no. 7, pp. 2977–2991, 2015.

[7] A. Epstein and G. V. Eleftheriades, "Huygens' metasurfaces via the equivalence principle: design and applications," *Journal of the Optical Society of America B*, vol. 33, no. 2, pp. A31–A50, 2016.

[8] K. Achouri and C. Caloz, "Design, concepts and applications of electromagnetic metasurfaces," *Nanophotonics*, vol. 7, no. 6, pp. 1095–1116, 2018.

[9] O. M. Bucci, I. Catapano, L. Crocco, and T. Isernia, "Synthesis of new variable dielectric profile antennas via inverse scattering techniques: a feasibility study," *IEEE transactions on antennas and propagation*, vol. 53, no. 4, pp. 1287–1297, 2005.

[10] R. Palmeri and T. Isernia, "Volumetric invisibility cloaks design through spectral coverage optimization," *IEEE Access*, vol. 7, pp. 30 860–30 867, 2019.

[11] R. F. Harrington, *Time-harmonic electromagnetic fields*. McGraw-Hill, 1961.

[12] E. J. Rothwell and M. J. Cloud, *Electromagnetics*. CRC Press, 2018.

[13] A. F. Peterson, S. L. Ray, and R. Mittra, *Computational Methods for Electromagnetics*. Wiley-IEEE Press, 1998.

[14] P. Mojabi, N. Firoozy, N. Bayat, T. Brown, C. Narendra, P. Mojabi, C. Niu, T. Tiede, T. Neusitzer, X. Li *et al.*, "Electromagnetic inversion for biomedical imaging, antenna characterization, and sea ice remote sensing applications," in *2016 URSI Asia-Pacific Radio Science Conference (URSI AP-RASC)*. IEEE, 2016, pp. 586–589.

[15] C. Narendra, T. Brown, N. Bayat, and P. Mojabi, "Multi-plane magnetic near-field data inversion using the source reconstruction method," in *2018 18th International Symposium on Antenna Technology and Applied Electromagnetics (ANTEM)*, Aug 2018, pp. 1–2.

[16] T. Brown, C. Narendra, C. Niu, and P. Mojabi, "On the use of electromagnetic inversion for near-field antenna measurements: A review," in *2018 IEEE Conference on Antenna Measurements & Applications (CAMA)*. IEEE, 2018, pp. 1–4.

[17] E. Jørgensen, P. Meincke, C. Cappellin, and M. Sabbadini, "Improved source reconstruction technique for antenna diagnostics," in *Proceeedings of the 32nd ESA Antenna Workshop*, 2010.

[18] L. Foged, L. Scialacqua, F. Saccardi, J. A. Quijano, G. Vecchi, and M. Sabbadini, "Practical application of the equivalent source method as an antenna diagnostics tool [amta corner]," *IEEE Antennas and Propagation Magazine*, vol. 54, no. 5, pp. 243–249, 2012.

[19] M. Oristaglio and H. Blok, "Wavefield imaging and inversion in electromagnetics and acoustics," *Course Notes TU Delft*, 1995.

[20] P. Mojabi, M. Ostadrahimi, L. Shafai, and J. LoVetri, "Microwave tomography techniques and algorithms: A review," in *2012 15 International Symposium on Antenna Technology and Applied Electromagnetics*, 2012, pp. 1–4.

[21] O. M. Bucci, G. D'Elia, G. Mazzarella, and G. Panariello, "Antenna pattern synthesis: a new general approach," *Proceedings of the IEEE*, vol. 82, no. 3, pp. 358–371, March 1994.

[22] L. Di Donato, T. Isernia, G. Labate, and L. Matekovits, "Towards printable natural dielectric cloaks via inverse scattering techniques," *Scientific reports*, vol. 7, no. 1, p. 3680, 2017.

[23] N. Firoozy, T. Neusitzer, D. S. Desmond, T. Tiede, M. J. L. Lemes, J. Landy, P. Mojabi, S. Rysgaard, G. Stern, and D. G. Barber, "An electromagnetic detection case study on crude oil injection in a young sea ice environment," *IEEE Transactions on Geoscience and Remote Sensing*, vol. 55, no. 8, pp. 4465–4475, Aug 2017.

[24] T. Brown, I. Jeffrey, and P. Mojabi, "Multiplicatively regularized source reconstruction method for phaseless planar near-field antenna measurements," *IEEE Transactions on Antennas and Propagation*, vol. 65, no. 4, pp. 2020–2031, 2017.

[25] M. Salucci, A. Gelmini, G. Oliveri, N. Anselmi, and A. Massa, "Synthesis of shaped beam reflectarrays with constrained geometry by exploiting nonradiating surface currents," *IEEE Transactions on Antennas and Propagation*, vol. 66, no. 11, pp. 5805–5817, Nov 2018.

[26] M. Phaneuf and P. Mojabi, "Electromagnetic inversion for noninvasive specific absorption rate characterization," *IEEE Journal of Electromagnetics, RF and Microwaves in Medicine and Biology*, vol. 4, no. 4, pp. 254–259, 2020.

[27] J. Hadamard, *Lectures on Cauchy's problem in linear partial differential equations*. Courier Corporation, 2014.

[28] A. Devaney and G. Sherman, "Nonuniqueness in inverse source and scattering problems," *IEEE Transactions on Antennas and Propagation*, vol. 30, no. 5, pp. 1034–1037, 1982.

[29] P. C. Hansen, "Regularization tools: A matlab package for analysis and solution of discrete ill-posed problems," *Numerical algorithms*, vol. 6, no. 1, pp. 1–35, 1994.

[30] A. Abubakar, P. M. van den Berg, and J. J. Mallorqui, "Imaging of biomedical data using a multiplicative regularized contrast source inversion method," *IEEE Trans. Microwave Theory Tech.*, vol. 50, no. 7, pp. 1761–1777, July 2002.

[31] A. Abubakar and P. M. van den Berg, "Iterative forward and inverse algorithms based on domain integral equations for three–dimensional electric and magnetic objects," *J. Comput. Phys.*, vol. 195, pp. 236–262, 2004.

[32] P. Mojabi, J. LoVetri, and L. Shafai, "A multiplicative regularized Gauss–Newton inversion for shape and location reconstruction," *IEEE Transactions on Antennas and Propagation*, vol. 59, no. 12, pp. 4790–4802, 2011.

[33] P. C. Hansen, "Analysis of discrete ill-posed problems by means of the L-curve," *SIAM Review*, vol. 34, no. 4, pp. 561–580, Dec 1992.

[34] T. K. Sarkar and A. Taaghol, "Near-field to near/far-field transformation for arbitrary near-field geometry utilizing an equivalent electric current andMOM," *IEEE Trans. Antennas Propag.*, vol. 47, no. 3, 1999.

[35] J. L. A. Quijano and G. Vecchi, "Improved-accuracy source reconstruction on arbitrary 3-D surfaces," *IEEE Antennas Wireless Propag. Lett.*, vol. 8, pp. 1046–1049, 2009.

[36] T. Brown, C. Narendra, C. Niu, and P. Mojabi, "On the use of electromagnetic inversion for near-field antenna measurements: A review," in *2018 IEEE Conference on Antenna Measurements Applications (CAMA)*, Sep. 2018, pp. 1–4.

[37] T. Brown, "Antenna characterization using phaseless near-field measurements," Master's thesis, University of Manitoba, 2016. [Online]. Available: http://hdl.handle.net/1993/31693

[38] C. Narendra, T. Brown, and P. Mojabi, "Gradient-based electromagnetic inversion for metasurface design using circuit models," *IEEE Transactions on antennas and propagation*, pp. 1–13, IEEE Early Access, Oct. 2021.

[39] S. Pearson and S. V. Hum, "Optimization of scalar and bianisotropic electromagnetic metasurface parameters satisfying far-field criteria," *arXiv preprint arXiv:2011.09016*, 2020.

[40] A. Abubakar and P. M. van den Berg, "The contrast source inversion method for location and shape reconstructions," *Inverse Problems*, vol. 18, no. 2, pp. 495–510, Mar 2002.

[41] C. Narendra and P. Mojabi, "Phaseless Gauss-Newton inversion for microwave imaging," *IEEE Transactions on Antennas and Propagation*, vol. 69, no. 1, pp. 443–456, 2021.

[42] M. Selvanayagam and G. V. Eleftheriades, "Circuit modeling of Huygens surfaces," *IEEE Antennas and Wireless Propagation Letters*, vol. 12, pp. 1642–1645, 2013.

[43] M. Chen, E. Abdo-Sánchez, A. Epstein, and G. V. Eleftheriades, "Theory, design, and experimental verification of a reflectionless bianisotropic Huygens' metasurface for wide-angle refraction," *Physical Review B*, vol. 97, no. 12, p. 125433, 2018.

[44] Z. Wei and X. Chen, "Deep-learning schemes for full-wave nonlinear inverse scattering problems," *IEEE Transactions on Geoscience and Remote Sensing*, vol. 57, no. 4, pp. 1849–1860, 2018.

[45] L. Li, H. Ruan, C. Liu, Y. Li, Y. Shuang, A. Alù, C.-W. Qiu, and T. J. Cui, "Machine-learning reprogrammable metasurface imager," *Nature communications*, vol. 10, no. 1, pp. 1–8, 2019.

[46] X. Chen, Z. Wei, M. Li, and P. Rocca, "A review of deep learning approaches for inverse scattering problems (invited review)," *Progress In Electromagnetics Research*, vol. 167, pp. 67–81, 2020.

[47] Y. Álvarez, F. Las-Heras, and M. R. Pino, "Reconstruction of equivalent currents distribution over arbitrary three-dimensional surfaces based on integral equation algorithms," *Antennas and Propagation, IEEE Transactions on*, vol. 55, no. 12, pp. 3460–3468, 2007.

[48] Y. A. Lopez, F. Las-Heras Andres, M. R. Pino, and T. K. Sarkar, "An improved super-resolution source reconstruction method," *IEEE Trans. Instrum. Meas.*, vol. 58, no. 11, pp. 3855–3866, 2009.

[49] T. F. Eibert, E. Kaliyaperumal, C. H. Schmidt *et al.*, "Inverse equivalent surface current method with hierarchical higher order basis functions, full probe correction and multilevel fast multipole acceleration," *Progress In Electromagnetics Research*, vol. 106, pp. 377–394, 2010.

[50] C. Narendra, I. Jeffrey, and P. Mojabi, "Using the source reconstruction method to model incident fields in microwave tomography," *IEEE Antennas and Wireless Propagation Letters*, vol. 16, pp. 46–49, 2016.

[51] N. Engheta and R. W. Ziolkowski, *Metamaterials: Physics and Engineering Explorations*. Wiley-IEEE Press, 2006.

[52] G. V. Eleftheriades, A. K. Iyer, and P. C. Kremer, "Planar negative refractive index media using periodically l-c loaded transmission lines," *IEEE Transactions on Microwave Theory and Techniques*, vol. 50, no. 12, pp. 2702–2712, 2002.

[53] N. Yu, P. Genevet, M. A. Kats, F. Aieta, J.-P. Tetienne, F. Capasso, and Z. Gaburro, "Light propagation with phase discontinuities: Generalized laws of reflection and refraction," *Science*, vol. 334, no. 6054, pp. 333–337, 2011. [Online]. Available: https://science.sciencemag.org/content/334/6054/333

[54] C. Pfeiffer and A. Grbic, "Metamaterial Huygens' surfaces: Tailoring wave fronts with reflectionless sheets," *Phys. Rev. Lett.*, vol. 110, p. 197401, May 2013.

[55] A. K. Iyer, A. Alù, and A. Epstein, "Metamaterials and metasurfaces—historical context, recent advances, and future directions," *IEEE Transactions on Antennas and Propagation*, vol. 68, no. 3, pp. 1223–1231, 2020.

[56] V. S. Asadchy, M. Albooyeh, S. N. Tcvetkova, A. Díaz-Rubio, Y. Ra'di, and S. Tretyakov, "Perfect control of reflection and refraction using spatially dispersive metasurfaces," *Physical Review B*, vol. 94, no. 7, p. 075142, 2016.

[57] C. Pfeiffer and A. Grbic, "Bianisotropic metasurfaces for optimal polarization control: Analysis and synthesis," *Physical Review Applied*, vol. 2, no. 4, p. 044011, 2014.

[58] Y. Ra'di, C. R. Simovski, and S. A. Tretyakov, "Thin perfect absorbers for electromagnetic waves: Theory, design, and realizations," *Phys. Rev. Applied*, vol. 3, p. 037001, Mar 2015.

[59] K. M. Kossifos, L. Petrou, G. Varnava, A. Pitilakis, O. Tsilipakos, F. Liu, P. Karousios, A. C. Tasolamprou, M. Seckel, D. Manessis, N. V. Kantartzis,

D. Kwon, M. A. Antoniades, and J. Georgiou, "Toward the realization of a programmable metasurface absorber enabled by custom integrated circuit technology," *IEEE Access*, vol. 8, pp. 92 986–92 998, 2020.

[60] M. Dehmollaian, N. Chamanara, and C. Caloz, "Wave scattering by a cylindrical metasurface cavity of arbitrary cross-section: Theory and applications," *IEEE Transactions on Antennas and Propagation*, 2019.

[61] M. Di Renzo, A. Zappone, M. Debbah, M.-S. Alouini, C. Yuen, J. de Rosny, and S. Tretyakov, "Smart radio environments empowered by reconfigurable intelligent surfaces: How it works, state of research, and road ahead," *arXiv preprint arXiv:2004.09352*, 2020.

[62] Y. Vahabzadeh, N. Chamanara, K. Achouri, and C. Caloz, "Computational analysis of metasurfaces," *IEEE Journal on Multiscale and Multiphysics Computational Techniques*, vol. 3, pp. 37–49, 2018.

[63] T. Brown, "Metasurface design using electromagnetic inversion," Ph.D. dissertation, University of Manitoba, Winnipeg, Canada, 2020.

[64] M. M. Idemen, *Discontinuities in the electromagnetic field*. John Wiley & Sons (IEEE Press series on electromagnetic wave theory; 40), 2011.

[65] E. F. Kuester, M. A. Mohamed, M. Piket-May, and C. L. Holloway, "Averaged transition conditions for electromagnetic fields at a metafilm," *IEEE Transactions on Antennas and Propagation*, vol. 51, no. 10, pp. 2641–2651, 2003.

[66] Y. Vahabzadeh, K. Achouri, and C. Caloz, "Simulation of metasurfaces in finite difference techniques," *IEEE Trans. Antennas Propag*, vol. 64, no. 11, pp. 4753–4759, 2016.

[67] K. Achouri, "Synthesis and applications of electromagnetic metasurfaces," Ph.D. dissertation, École Polytechnique de Montr'/eal, Montreal, Canada, 2017.

[68] T. Brown, Y. Vahabzadeh, C. Caloz, and P. Mojabi, "Electromagnetic inversion with local power conservation for metasurface design," *IEEE Antennas and Wireless Propagation Letters*, 2020.

[69] A. Epstein and G. V. Eleftheriades, "Passive lossless Huygens metasurfaces for conversion of arbitrary source field to directive radiation," *IEEE Transactions on Antennas and Propagation*, vol. 62, no. 11, pp. 5680–5695, 2014.

[70] G. Lavigne, K. Achouri, V. S. Asadchy, S. A. Tretyakov, and C. Caloz, "Susceptibility derivation and experimental demonstration of refracting metasurfaces without spurious diffraction," *IEEE Transactions on Antennas and Propagation*, vol. 66, no. 3, pp. 1321–1330, 2018.

[71] D. M. Pozar, *Microwave engineering*. John wiley & sons, 2011.

[72] E. Porter, M. Coates, and M. Popovic, "An early clinical study of time-domain microwave radar for breast health monitoring," *IEEE Transactions on Biomedical Engineering*, vol. 63, no. 3, pp. 530–539, 2016.

[73] E. C. Fear, X. Li, S. C. Hagness, and M. A. Stuchly, "Confocal microwave imaging for breast cancer detection: localization of tumors in three dimensions," *IEEE Transactions on Biomedical Engineering*, vol. 49, no. 8, pp. 812–822, 2002.

[74] S. P. Poplack, T. D. Tosteson, W. A. Wells, B. W. Pogue, P. M. Meaney, A. Hartov, C. A. Kogel, S. K. Soho, J. J. Gibson, and K. D. Paulsen, "Electromagnetic breast imaging: results of a pilot study in women with abnormal mammograms," *Radiology*, vol. 243, no. 2, pp. 350–359, 2007.

[75] E. C. Fear, S. C. Hagness, P. M. Meaney, M. Okoniewski, and M. A. Stuchly, "Enhancing breast tumor detection with near-field imaging," *IEEE Microwave Mag.*, vol. 3, no. 1, pp. 48–56, Mar 2002.

[76] W. H. Weedon, W. C. Chew, and P. E. Mayes, "A step-frequency radar imaging system for microwave nondestructive evaluation," *Progress In Electromagnetics Research*, vol. 28, pp. 121–146, 2000.

[77] N. Bayat, "Advancing microwave imaging algorithms and techniques," Ph.D. dissertation, University of Manitoba, 2019.

[78] A. Abubakar, T. Habashy, V. Druskin, L. Knizhnerman, and D. Alumbaugh, "2.5 D forward and inverse modeling for interpreting low-frequency electromagnetic measurements," *Geophysics*, vol. 73, no. 4, pp. F165–F177, 2008.

[79] P. Mojabi and J. LoVetri, "Microwave biomedical imaging using the multiplicative regularized gauss–newton inversion," *IEEE Antennas and Wireless Propagation Letters*, vol. 8, pp. 645–648, 2009.

[80] R. Palmeri, M. T. Bevacqua, A. F. Morabito, and T. Isernia, "Inverse scattering methods as a tool for the design of GPCs devices," in *2017 IEEE Conference on Antenna Measurements & Applications (CAMA)*. IEEE, 2017, pp. 130–132.

[81] T. Isernia and R. Palmeri, "Inverse scattering as a way to artificial dielectrics based devices," in *2018 12th International Congress on Artificial Materials for Novel Wave Phenomena (Metamaterials)*. IEEE, 2018, pp. 185–187.

[82] C. Narendra and P. Mojabi, "A phaseless gauss-newton inversion algorithm for imaging and design," in *2020 14th European Conference on Antennas and Propagation (EuCAP)*, 2020, pp. 1–5.

[83] F. Monticone, N. M. Estakhri, and A. Alu, "Full control of nanoscale optical transmission with a composite metascreen," *Physical review letters*, vol. 110, no. 20, p. 203903, 2013.

[84] M. Selvanayagam and G. V. Eleftheriades, "Circuit modeling of Huygens surfaces," *IEEE Antennas and Wireless Propagation Letters*, vol. 12, pp. 1642–1645, 2013.

[85] G. Xu, S. V. Hum, and G. V. Eleftheriades, "Augmented Huygens? metasurfaces employing baffles for precise control of wave transformations," *IEEE Transactions on Antennas and Propagation*, vol. 67, no. 11, pp. 6935–6946, 2019.

[86] C. L. Holloway, E. F. Kuester, J. A. Gordon, J. O'Hara, J. Booth, and D. R. Smith, "An overview of the theory and applications of metasurfaces: The two-dimensional equivalents of metamaterials," *IEEE Antennas and Propagation Magazine*, vol. 54, no. 2, pp. 10–35, 2012.

[87] M. Selvanayagam and G. Eleftheriades, "Discontinuous electromagnetic fields using orthogonal electric and magnetic currents for wavefront manipulation," *Optics Express*, pp. 14 409–14 429, 2013.

[88] S. Tretyakov, "Metasurfaces for general transformations of electromagnetic fields," *Philos. Trans. Royal Soc. A: Mathematical, Physical and Engineering Sciences*, vol. 373, no. 2049, p. 20140362, 2015.

[89] M. Yazdi, M. Albooyeh, R. Alaee, V. Asadchy, N. Komjani, C. Rockstuhl, C. R. Simovski, and S. Tretyakov, "A bianisotropic metasurface with resonant asymmetric absorption," *IEEE Transactions on Antennas and Propagation*, vol. 63, no. 7, pp. 3004–3015, 2015.

[90] V. S. Asadchy, I. A. Faniayeu, Y. Ra?Di, S. Khakhomov, I. Semchenko, and S. Tretyakov, "Broadband reflectionless metasheets: frequency-selective transmission and perfect absorption," *Physical Review X*, vol. 5, no. 3, p. 031005, 2015.

[91] V. G. Ataloglou, A. H. Dorrah, and G. V. Eleftheriades, "Design of compact Huygens' metasurface pairs with multiple reflections for arbitrary wave transformations," *IEEE Transactions on Antennas and Propagation (Early Access)*, 2020.

[92] K. Achouri and O. J. Martin, "Angular scattering properties of metasurfaces," *IEEE Transactions on Antennas and Propagation*, vol. 68, no. 1, pp. 432–442, 2019.

[93] S. Pearson and S. V. Hum, "Using augmented Lagrangian methods to design electromagnetic surfaces with far field constraints," in *2020 IEEE International Symposium on Antennas and Propagation and USNC-URSI Radio Science Meeting*, 2020, pp. 969–970.

[94] A. Epstein and G. V. Eleftheriades, "Arbitrary power-conserving field transformations with passive lossless omega-type bianisotropic metasurfaces," *IEEE Transactions on Antennas and Propagation*, vol. 64, no. 9, pp. 3880–3895, 2016.

[95] T. Brown, Z. Liu, and P. Mojabi, "Full-wave verification of an electromagnetic inversion metasurface design method," 2020.

[96] J. P. Wong, A. Epstein, and G. V. Eleftheriades, "Reflectionless wide-angle refracting metasurfaces," *IEEE Antennas and Wireless Propagation Letters*, vol. 15, pp. 1293–1296, 2015.

[97] E. Abdo-Sánchez, M. Chen, A. Epstein, and G. V. Eleftheriades, "A leaky-wave antenna with controlled radiation using a bianisotropic huygens' metasurface," *IEEE Trans. Antennas Propag.*, vol. 67, no. 1, pp. 108–120, 2019.

[98] S. R. Rengarajan and Y. Rahmat-Samii, "The field equivalence principle: Illustration of the establishment of the non-intuitive null fields," *Antennas and Propagation Magazine, IEEE*, vol. 42, no. 4, pp. 122–128, 2000.

[99] T. Brown and P. Mojabi, "Cascaded Metasurface Design Using Electromagnetic Inversion with Gradient-Based Optimization," *Available online at techrxiv*, 2020.

[100] J. Y. Lau and S. V. Hum, "Reconfigurable transmitarray design approaches for beamforming applications," *IEEE Trans. Antennas Propag.*, vol. 60, no. 12, pp. 5679–5689, 2012.

[101] R. Palmeri, M. T. Bevacqua, A. F. Morabito, and T. Isernia, "Design of artificial-material-based antennas using inverse scattering techniques," *IEEE Transactions on Antennas and Propagation*, vol. 66, no. 12, pp. 7076–7090, Dec 2018.

[102] V. G. Ataloglou, A. H. Dorrah, and G. V. Eleftheriades, "Design of compact Huygens' metasurface pairs with multiple reflections for arbitrary wave transformations," *IEEE Transactions on Antennas and Propagation*, 2020.

[103] M. Ostadrahimi, P. Mojabi, C. Gilmore, A. Zakaria, S. Noghanian, S. Pistorius, and J. LoVetri, "Analysis of incident field modeling and incident/scattered field calibration techniques in microwave tomography," *IEEE Antennas and Wireless Propagation Letters*, vol. 10, pp. 900–903, 2011.

[104] X. Chen, "Subspace-based optimization method for solving inverse-scattering problems," *IEEE Transactions on Geoscience and Remote Sensing*, vol. 48, no. 1, pp. 42–49, Jan 2010.

[105] T. Rubæk, P. M. Meaney, P. Meincke, and K. D. Paulsen, "Nonlinear microwave imaging for breast-cancer screening using Gauss-Newton's method and the CGLS inversion algorithm," *IEEE Trans. Antennas Propag.*, vol. 55, no. 8, pp. 2320–2331, Aug 2007.

[106] W. C. Chew and Y. M. Wang, "Reconstruction of two-dimensional permittivity distribution using the distorted born iterative method," *IEEE Transactions on Medical Imaging*, vol. 9, no. 2, pp. 218–225, June 1990.

[107] M. Pastorino, *Microwave imaging*. John Wiley & Sons, 2010, vol. 208.

[108] P. Mojabi and J. LoVetri, "Overview and classification of some regularization techniques for the Gauss-Newton inversion method applied to inverse scattering problems," *IEEE Transactions on Antennas and Propagation*, vol. 57, no. 9, pp. 2658–2665, Sept 2009.

[109] S. F. Razavi and Y. Rahmat-Samii, "Resilience to probe-positioning errors in planar phaseless near-field measurements," *IEEE Transactions on Antennas and Propagation*, vol. 58, no. 8, pp. 2632–2640, 2010.

[110] L. Li, H. Zheng, and F. Li, "Two-dimensional contrast source inversion method with phaseless data: TM case," *IEEE Transactions on Geoscience and Remote Sensing*, vol. 47, no. 6, pp. 1719–1736, 2009.

[111] Z. Hu, L. Lianlin, and L. Fang, "A multi-frequency MRCSI algorithm with phaseless data," *Inverse Problems*, vol. 25, no. 6, p. 065006, 2009.

[112] M. H. Maleki, A. J. Devaney, and A. Schatzberg, "Tomographic reconstruction from optical scattered intensities," *JOSA A*, vol. 9, no. 8, pp. 1356–1363, 1992.

[113] M. H. Maleki and A. J. Devaney, "Phase-retrieval and intensity-only reconstruction algorithms for optical diffraction tomography," *JOSA A*, vol. 10, no. 5, pp. 1086–1092, 1993.

[114] T. Takenaka, D. J. Wall, H. Harada, and M. Tanaka, "Reconstruction algorithm of the refractive index of a cylindrical object from the intensity measurements of the total field," *Microwave and optical technology letters*, vol. 14, no. 3, pp. 182–188, 1997.

[115] G. Gbur and E. Wolf, "Hybrid diffraction tomography without phase information," *JOSA A*, vol. 19, no. 11, pp. 2194–2202, 2002.

[116] S. Caorsi, A. Massa, M. Pastorino, and A. Randazzo, "Electromagnetic detection of dielectric scatterers using phaseless synthetic and real data and the memetic algorithm," *IEEE transactions on geoscience and remote sensing*, vol. 41, no. 12, pp. 2745–2753, 2003.

[117] L. Crocco, M. D'Urso, and T. Isernia, "Inverse scattering from phaseless measurements of the total field on a closed curve," *JOSA A*, vol. 21, no. 4, pp. 622–631, 2004.

[118] G. Franceschini, M. Donelli, R. Azaro, and A. Massa, "Inversion of phaseless total field data using a two-step strategy based on the iterative multiscaling approach," *IEEE Transactions on Geoscience and Remote Sensing*, vol. 44, no. 12, pp. 3527–3539, 2006.

[119] A. Litman and K. Belkebir, "Two-dimensional inverse profiling problem using phaseless data," *JOSA A*, vol. 23, no. 11, pp. 2737–2746, 2006.

[120] O. M. Bucci, L. Crocco, M. D'Urso, and T. Isernia, "Inverse scattering from phaseless measurements of the total field on open lines," *JOSA A*, vol. 23, no. 10, pp. 2566–2577, 2006.

[121] M. d'Urso, K. Belkebir, L. Crocco, T. Isernia, and A. Litman, "Paseless imaging with experimental data: facts and challenges," *JOSA A*, vol. 25, no. 1, pp. 271–281, 2008.

[122] L. Li, W. Zhang, and F. Li, "Tomographic reconstruction using the distorted rytov iterative method with phaseless data," *IEEE Geoscience and Remote Sensing Letters*, vol. 5, no. 3, pp. 479–483, 2008.

[123] W. Zhang, L. Li, and F. Li, "Multifrequency imaging from intensity-only data using the phaseless data distorted rytov iterative method," *IEEE Transactions on Antennas and Propagation*, vol. 57, no. 1, pp. 290–295, 2009.

[124] R. G. Yaccarino and Y. Rahmat-Samii, "Phaseless bi-polar planar near-field measurements and diagnostics of array antennas," *IEEE Transactions on Antennas and Propagation*, vol. 47, no. 3, pp. 574–583, March 1999.

[125] C. Gilmore, P. Mojabi, A. Zakaria, M. Ostadrahimi, C. Kaye, S. Noghanian, L. Shafai, S. Pistorius, and J. LoVetri, "A wideband microwave tomography system with a novel frequency selection procedure," *IEEE Transactions on Biomedical Engineering*, vol. 57, no. 4, pp. 894–904, April 2010.

[126] S. Costanzo and G. Di Massa, "Wideband phase retrieval technique from amplitude-only near-field data." *Radioengineering*, vol. 17, no. 4, 2008.

[127] S. Costanzo, G. Di Massa, M. Pastorino, and A. Randazzo, "Hybrid microwave approach for phaseless imaging of dielectric targets," *IEEE Geoscience and Remote Sensing Letters*, vol. 12, no. 4, pp. 851–854, April 2015.

[128] T. M. Habashy and A. Abubakar, "A general framework for constraint minimization for the inversion of electromagnetic measurements," *Progress in electromagnetics Research*, vol. 46, pp. 265–312, 2004.

[129] P. Mojabi, "Investigation and development of algorithms and techniques for microwave tomography," Ph.D. dissertation, University of Manitoba, Winnipeg, Manitoba, Canada, 2010.

[130] N. Bayat and P. Mojabi, "Incorporating spatial priors in microwave imaging via multiplicative regularization," *IEEE Transactions on Antennas and Propagation*, 2019.

[131] P. Mojabi and N. Bayat, "A multiplicative regularizer to incorporate prior spatial data in microwave imaging reconstruction," in *13th European Conference on Antennas and Propagation*, April 2019, pp. 1–5.

[132] A. H. Golnabi, P. M. Meaney, S. D. Geimer, and K. D. Paulsen, "3-d microwave tomography using the soft prior regularization technique: Evaluation in anatomically realistic mri-derived numerical breast phantoms," *IEEE Transactions on Biomedical Engineering*, vol. 66, no. 9, pp. 2566–2575, Sep. 2019.

[133] L. M. Neira, B. D. Van Veen, and S. C. Hagness, "High-resolution microwave breast imaging using a 3-d inverse scattering algorithm with a variable-strength spatial prior constraint," *IEEE Transactions on Antennas and Propagation*, vol. 65, no. 11, pp. 6002–6014, Nov 2017.

[134] A. H. Golnabi, P. M. Meaney, and K. D. Paulsen, "Tomographic microwave imaging with incorporated prior spatial information," *IEEE Transactions on Microwave Theory and Techniques*, vol. 61, no. 5, pp. 2129–2136, May 2013.

[135] C. Gilmore, A. Zakaria, P. Mojabi, M. Ostadrahimi, S. Pistorius, and J. LoVetri, "The University of Manitoba microwave imaging repository: A two-dimensional microwave scattering database for testing inversion and calibration algorithms [Measurements Corner]," *IEEE Antennas and Propagation Magazine*, vol. 53, no. 5, pp. 126–133, Oct 2011.

[136] C. Narendra and P. Mojabi, "A combined inverse source and scattering technique for dielectric profile design to tailor electromagnetic fields," *IEEE Transactions on Antennas and Propagation*, pp. 1–12, IEEE Early Access, Oct. 2021.

[137] N. K. Nikolova, *Introduction to Microwave Imaging.* Cambridge University Press, 2017.

[138] X. Chen, *Computational Methods for Electromagnetic Inverse Scattering.* Wiley and IEEE Press, 2018.

[139] A. Abubakar, T. M. Habashy, V. L. Druskin, L. Knizhnerman, and D. Alumbaugh, "2.5D forward and inverse modeling for interpreting low-frequency electromagnetic measurements," *Geophysics*, vol. 73, no. 4, pp. F165–F177, July–Aug 2008.

[140] P. van den Berg and A. Abubakar, "Optical microscopy imaging using the contrast source inversion method," *Journal of Modern Optics*, vol. 57, pp. 756–764, 05 2010.

[141] M. Pastorino, A. Massa, and S. Caorsi, "A microwave inverse scattering technique for image reconstruction based on a genetic algorithm," *IEEE Transactions on Instrumentation and Measurement*, vol. 49, no. 3, pp. 573–578, 2000.

[142] P. M. van den Berg and R. E. Kleinman, "A contrast source inversion method," *Inverse Probl.*, vol. 13, pp. 1607–1620, 1997.

[143] R. Palmeri, M. T. Bevacqua, A. F. Morabito, and T. Isernia, "Design of artificial-material-based antennas using inverse scattering techniques," *IEEE Transactions on Antennas and Propagation*, vol. 66, no. 12, pp. 7076–7090, 2018.

[144] R. Palmeri and T. Isernia, "Inverse design of artificial materials based lens antennas through the scattering matrix method," *Electronics*, vol. 9, no. 4, p. 559, 2020.

[145] N. M. Estakhri and N. Engheta, "Tunable metasurface-based waveplates-a proposal using inverse design," *Comptes Rendus. Physique*, pp. 1–15, 2020.

[146] H. Mosallaei and Y. Rahmat-Samii, "Nonuniform luneburg and two-shell lens antennas: radiation characteristics and design optimization," *IEEE Transactions on Antennas and Propagation*, vol. 49, no. 1, pp. 60–69, 2001.

[147] J. Budhu and Y. Rahmat-Samii, "A novel and systematic approach to inhomogeneous dielectric lens design based on curved ray geometrical optics and particle swarm optimization," *IEEE Transactions on Antennas and Propagation*, vol. 67, no. 6, pp. 3657–3669, 2019.

[148] F. Yang and Y. Rahmat-Samii, Eds., *Surface Electromagnetics: With Applications in Antenna, Microwave, and Optical Engineering.* Cambridge University Press, 2019.

[149] C. Parini, S. Gregson, J. McCormick, and D. Janse van Rensburg, *Theory and Practice of Modern Antenna Range Measurements.* The Institution of Engineering and Technology, 2014.

[150] T. Brown, C. Narendra, and P. Mojabi, "On the use of the source reconstruction method for metasurface design," *12th European Conference on Antennas and Propagation (EuCAP)*, pp. 302–306, April 2018.

[151] A. Van Den Bos, "Complex gradient and hessian," *IEE Proceedings-Vision, Image and Signal Processing*, vol. 141, no. 6, pp. 380–382, 1994.

[152] P. Mojabi and J. LoVetri, "Use of Wirtinger calculus in Gauss-Newton inversion of microwave tomography data," in *2014 XXXIth URSI General Assembly and Scientific Symposium (URSI GASS)*, Aug 2014, pp. 1–4.

[153] J. De Zaeytijd, A. Franchois, C. Eyraud, and J. Geffrin, "Full-wave three-dimensional microwave imaging with a regularized Gauss–Newton method – Theory and experiment," *IEEE Transactions on Antennas and Propagation*, vol. 55, no. 11, pp. 3279–3292, Nov 2007.

[154] E. Corp. Emscan products. [Online]. Available: https://www.emscan.com/products/

[155] P. Petre and T. K. Sarkar, "A planar near-field to far-field transformation using an equivalent magnetic current approach," in *Antennas and Propagation Society International Symposium, 1992. AP-S. 1992 Digest. Held in Conjuction with: URSI Radio Science Meeting and Nuclear EMP Meeting., IEEE.* IEEE, 1992, pp. 1534–1537.

[156] S. Rao, D. Wilton, and A. Glisson, "Electromagnetic scattering by surfaces of arbitrary shape," *IEEE Transactions on antennas and propagation*, vol. 30, no. 3, pp. 409–418, 1982.

[157] A. Kiaee, R. R. Alavi, M. M. Honari, R. Mirzavand, and P. Mousavi, "Ground de-embedded source reconstruction using a planar array of h-field probes," in *Antennas and Propagation & USNC/URSI National Radio Science Meeting, 2017 IEEE International Symposium on.* IEEE, 2017, pp. 133–134.